SAPIENZA
UNIVERSITÀ DI ROMA

PhD Thesis

Insulin signaling network: mathematical modeling and parameter estimation from experimental data

Department of Computer, Control and Management Engineering

PhD in Automatica and Operations Research
ING/INF 04
Cycle XXVIII

Candidate

Federica Conte

Advisor

Prof. Serenella Salinari

Co-Advisor

Dr. Alessandro Bertuzzi

To my family and Fabio.
I love you.

Summary

The insulin signaling network (ISN) is an important metabolic network that, upon the insulin binding to its receptor at the cell surface, triggers the glucose uptake into the cell. The study of this mechanism within muscle cells, hepatocytes and cells of the adipose tissue is of major interest since it is crucial for understanding more clearly the factors that may induce the insulin resistance. However, the structure and the behaviour of the insulin signaling network are only partially known and the current research on this topic is fragmented into various lines of investigation. Because of the high degree of complexity of the ISN, it is difficult to understand, without a theoretical framework, how the network responses evidenced from the experimental data determine the cell behaviour.

In the present thesis, we proposed a detailed mathematical model of the ISN in order to investigate the factors that affect the basal concentrations and the dose-response curves (i.e., the steady state concentrations at given insulin levels) of the main components of the whole network. Our model concentrated particularly on single and double phosphorylation of Akt protein, and hypothesized the existence of a putative factor released by the small intestine that induces insulin resistance by activating the mammalian target of rapamycin complex 2 (mTORC2) in an insulin-independent manner and possibly operating through the IGF-1 receptor. Such hypothesis is based on clinical and experimental observations.

The parameters of the ISN model were estimated from the experimental data of two skeletal muscle cell lines using a least squares approach. As the available data consisted in the equilibrium concentrations of many of the

known signaling components at given values of the insulin, we derived the concentrations of the chemicals at the steady-state from the kinetic equations and then we implemented an algorithm that minimizes the distance between the model outputs and the data. For the numerical solution, we used a local optimization routine based on a derivative-free algorithm for bound constrained optimization. The ISN model was able to adequately fit the available experimental data. The model could thus become a useful tool to generate and test hypotheses, leading to a deeper understanding of the molecular mechanisms underlying insulin resistance and, in future perspective, to find drugs able to counterbalance the effects of this disease.

Finally, as it is now widely recognized that Akt and mTOR complexes have a major role also in the regulation of cell proliferation, and then in cancer development, we combined the ISN model with a mathematical model that described the evolution of a AML (acute myeloid leukemia) cell population in order to investigate the effects of mTOR inhibitors with antitumor activity on the ISN and on the cell population response. Based on literature data of AML cell response to mTOR inhibitors with antitumor activity (the dual ATP-competitive mTOR inhibitor AZD8055), the two models provided simple relationships between the concentrations of proteins of the ISN and parameters representative of cell cycle progression and cell death.

Acknowledgments

I am indebted to many people for making my PhD an unforgettable experience.

First and foremost, I want to thank the group with whom I have had the pleasure to work for this dissertation. My advisor, Prof. Serenella Salinari, that accepted me as her Ph.D. student and proposed to me a such interesting topic for my PhD thesis. Dr. Alessandro Bertuzzi, one of the best people that I know, both humanly and scientifically. To work with him has been an honour for me. He has oriented and supported me with care, and has always been patient listening to my ideas and discussions. His ability to approach the research problems, his high scientific knowledges, and his hard work set an example. In addition, I have been very privileged to know and to collaborate with Prof. Geltrude Mingrone, an excellent example of successful woman physician and professor. The enthusiasm that she has for her research was contagious and motivational for me. Special thanks to Dr. Carmela Sinisgalli and Dr. Federico Papa that have been a source of friendships as well as good advice and collaboration. They have always been ready to help me and I have appreciated all their contributions of time, ideas, and encouragement in times of difficulties.

Then, I would like to acknowledge the funding sources that made my Ph.D. work possible. I was funded by the Department of Department of Computer, Control, and Management Engineering, Sapienza University of Rome. My work was also supported by the Institute of Systems Analysis and Computer Science of National Research Council of Rome (IASI-CNR).

My time at IASI-CNR was made enjoyable in large part due to the many friends and roommates that are a part of my life: my loving, supportive, encouraging, and patient Giulia that, in such a short time, has become one of my closest friends; Emanuel and his contagious joy and enthusiasm; Valentina that has shared with me fun and her knowledge of biology; the other postdocs and researchers, especially Antonio, Valerio, Paola and Teresa that have contributed immensely to my personal and professional time at IASI-CNR.

Finally, I thank my family for all their love and encouragement and Fabio, who has always been my biggest supporter and has unconditionally loved me during my good and bad times. I love you with all my heart.

Thank you to everybody.

Federica

Contents

Introduction

Physiological and cellular processes of the living systems are controlled by metabolic, signaling and transcription networks, specialized for cell cycle control, growth regulation, stress response, and many other cell functions.

In particular, cell signaling networks are complex cascades of reactions triggered by the binding of a ligand to a receptor on the plasma membrane. Inside the cell, signaling networks involve changes in protein-protein interactions permitting cells to communicate with other cells and with the external environment and to undergo phenotypic changes, such as cellular division, differentiation, death and others. Hence, these networks can be considered as information processing devices that translate input signals into output signals in which information is often coded by concentrations, modifications,and localization of proteins, either in the stationary levels or in temporal patterns.

Systems biology research helps us to understand the structure of cell signaling networks and how changes in these networks may affect the transmission of information. Malfunctioning of signaling networks may alter physiological processes of cells, potentially leading to severe consequences on the organism. The most common pathologies caused by altered cellular signaling networks concern heart diseases, metabolic disorders and immunological abnormalities. Moreover, it has been demonstrated that networks malfunctioning are involved with oncogenic properties of cancer cells [1].

The insulin signaling network (ISN) is an important metabolic network that, upon the insulin binding to its receptor at the cell surface, triggers the glucose uptake into the cell. The study of this mechanism within muscle cells, hepatocytes and cells of the adipose tissue is of major interest since it is crucial for understanding the mechanisms underlying insulin resistance, which represents the common denominator of a series of diseases, including obesity, type 2 diabetes (T2D), metabolic syndrome and cancer. However, the dynamics of the insulin signaling pathway is only partially known and the current research is fragmented. The complexity of the ISN derives not only from the enormous amount of different molecules involved in the process (often shared among pathways initiated by distinct receptors), but also from the presence of several feedback and feedforward signals, both negative and positive. Such links generate signaling networks rather than a linear pathway. So, the analysis of ISN requires a combination of experimental and theoretical approaches including the development and analysis of mathematical models and simulations. Without a theoretical framework, it is difficult to understand how the complexities evident from experimental data determine cell behaviour. We need a systems approach in order to achieve a deeper understanding of the molecular mechanisms underlying insulin resistance and, in the future perspective, to find drugs able to counterbalance the effect of the disease.

The main components and interconnections within the insulin signaling pathway are well established [2, 3, 4, 5], with the protein kinase B (PKB), also known as Akt, and the two mammalian Target of Rapamycin Complexes (mTORC1 and mTORC2) playing a special role. Akt is phosphorylated on Thr308 by the phosphoinositide-dependent protein kinase-1 (PDK1) and on Ser473 by mTORC2 [6], and the maximal Akt activity is achieved when the molecule is phosphorylated on both residues, allowing the translocation of the insulin-regulated glucose transporters (GLUT4) from the cytoplasmic pool to the plasma membrane (PM) in muscle and adipose cell [7, 8]. PDK1 and mTORC2 respond to the activation of the insulin receptors and also of the insulin-like growth factor 1 (IGF1) [5], via the insulin receptor substrate 1 (IRS1), the phosphatidylinositide 3-kinase (PI3K), and the phosphatidylinositol 3,4,5-trisphosphate (PIP$_3$). Akt activation results in the activation and inhibition of a variety of targets, such as mTORC1, the glycogen synthase kinase 3 (GSK3) and the Forkhead box protein O1 (FoxO1).

The kinase cascade through the insulin receptor (IR) up to mTORC1, as well as the mTORC1 activation by amino acids and energy, are clearly assessed [9]. By contrast, the upstream regulation of mTORC2 is not yet well-characterized [10]. The tuberous sclerosis complex 1/2 (TSC1/TSC2) appears to be required for mTORC2 activation [11, 4]. However, this view was questioned in a study that reported the experimental time courses of several proteins of the ISN under amino acids and insulin stimulation [12]. Interpreting the data by a dynamic model of the network, it was argued that mTORC2 activation pathway may originate from the IR or IRS1, possibly via a variant of PI3K [12]. A still different view emerged from experiments in non-diabetic mice both in vivo and in muscle biopsies, and in L6 cells exposed to a medium enriched with proteins secreted by the small intestine of diabetic rats and to serum from insulin resistant humans [13]. This study showed that jejunal factor/s induce insulin resistance and that these factors activate mTORC2, as revealed by the increased value of Ser473 Akt phosphorylation even in the absence of insulin stimulation. The presence of such intestinal factors was also suggested by the decrease of insulin resistance following bariatric surgery, a procedure in which a portion of the stomach and of the small intestine are removed or bypassed [14].

As the mTORC1 substrate S6 kinase 1 (S6K1) is involved in the regulation of protein synthesis and the growth of cell size, and FoxO1 in the regulation of proliferation and apoptosis, the ISN appears to have a main role not only in obesity and diabetes but also in cancer [5, 15, 9].

Following the seminal papers of Wanant and Quon [16] and of Sedaghat et al. [17], several studies have investigated the insulin-induced behavior of the ISN, or of some of its components, by means of mathematical models and the analysis of experimental data. Complex dynamical models, supported by the analysis of the time-course of protein concentrations after insulin stimulation, were developed and investigated in [12, 18, 19]. Other studies [20, 21] considered the dose-response curves (i.e., the steady state concentrations at given insulin levels), that are largely used in the literature to assess the behavior of ISN components at various levels of insulin stimulation and to evaluate the response to perturbing agents and drugs.

Aim of the present PhD thesis is to investigate the factors that affect the basal protein concentrations and the dose-response curves of the ISN. We developed a mathematical model of the network at the steady state, focusing mainly on the single and double Akt phosphorylation and on the upstream signaling of mTORC2. Experimental data of C2C12 myoblasts with the phosphatase and tensin homologue (PTEN) suppressed and data of L6 myotubes with induced insulin resistance have been analyzed by the model. The factors that induce insulin resistance have been modeled according to the findings in [13].

In detail, in Chapter 1 the main mechanisms underlying glucose-insulin homeostatic control both at organ/tissue level and at molecular level are discussed: we first show how the plasma glucose level is regulated by the insulin from a top-down point of view with the main combined experimental-modeling tools which are currently employed in investigating the behaviour of the glucose-insulin system; then, we detail the biochemical chain of reactions giving rise to glucose uptake in order to identify the key components of the ISN.

Chapter 2 contains an overview of the main computational approaches used to model signaling networks along with the most common methods of parameter estimation for biochemical systems.

Chapter 3 describes several models of the insulin signaling network proposed in the literature. The mathematical model used in the present work to analyze the available experimental data is then introduced. The present ISN model was developed in three stages: 1) the chemical reactions characterizing the network were established and written according to the Michaelis-Menten scheme; 2) as our goal was to investigate the factors affecting the basal concentrations and the dose-response curve of the main components of ISN, the steady-state concentrations of the chemicals were derived from the kinetic equations; 3) the expressions of steady-state concentrations were written in a normalized form to reduce the number of unknown parameters.

Chapter 4 discusses the estimation of the parameters values of the proposed ISN model. The model equations in the normalized form were fit to the experimental data of two different skeletal muscle cell lines of rodents (L6 myoblasts and C2C12 myotubes) through minimization of a least-squares index. This chapter also reports a detailed description of the experimental data used for the parameter estimation and of the optimization algorithm. Moreover, a sensitivity analysis was performed in order to investigate how changes of model parameters influence the system behaviour at the steady state and to identify those parameters that have the greatest impact on the system output. We also used the model to predict the effects of gene silencing as well as the effects of inhibitors and drugs.

Finally, in view of the close relationship between insulin resistance and cancer, Chapter 5 focuses on the combination of the insulin signaling model with a cell population model. In order to link these two models, we considered the response of the ISN and of an acute myeloid leukemia cell population to a mTOR inhibitor with antitumor activity (AZD8055).

Chapter 1

Glucose homeostasis and insulin action: from the organ and tissue level to the molecular level

Glucose is the major source of energy for living cells. The body makes glucose from all three elements of food (protein, fats, and carbohydrates) but the largest amount of glucose derives from carbohydrates. However, cells cannot use glucose without the help of insulin.

Insulin is the major hormone controlling energy homeostasis in human body and dysfunction in the insulin control perturbs glucose homeostasis leading to diseases such as type 2 diabetes (T2D) and its complications (e.g. cardiovascular disease, nephropathy, and neuropathy). The glucose homeostasis depends on the balance between hepatic glucose production and glucose utilization by the major insulin-dependent tissues, such as liver, adipose, and muscle, and by insulin-independent tissues, such as brain and kidney. This balance is tightly regulated by pancreatic hormones: in normal individuals, the response to increased plasma glucose levels is an increase in secretion of insulin from beta-cells of the pancreatic islets. This increase in insulin levels stimulates glucose transport into peripheral tissues and inhibits hepatic gluconeogenesis. In addition to its primary effects on glucose homeostasis, insulin also promotes a number of other important cellular events [22, 23].

Mainly due to the high social impact of diabetes (particularly of T2D in industrialized societies, given its link with obesity [24]), the glucose-insulin homoeostatic control has been one of the most intensely modeled biomedical problems. Modeling attempts to represent quantitatively the main features of the system, to improve the identification of the mechanisms involved, to predict the future conditions of a given patient.

In general, two different but complementary strategies can be applied to model physiological and biochemical systems: *top-down* and *bottom-up* approaches [25]. In a top-down approach an overview of the system is formulated, specifying but not detailing any first-level subsystems. Each subsystem is then refined with more details, sometimes in many additional subsystem levels, until the entire specification is reduced to base elements. In a bottom-up approach the individual base elements of the system are first specified in great detail. These elements are then linked together to form larger subsystems, until a complete top-level system is formed. In other words, the top-down modeling stars from the physiological functions and moves to understand underlying mechanisms, while the bottom-up modeling starts from the molecular details and build toward physiology.

Given the vastity of the field and the large number of important results obtained over the past four decades or so, it is impossible to present in this thesis all facets of the glucose homeostasis problem. However, to clearly understand the events leading to insulin-resistant states and the pathophysiology of insulin deficiency, it is necessary to have a total body point view, that is to consider the main mechanisms underlying the glucose-insulin homeostatic control both at organ/tissue level and at molecular level. For this reason, in the present chapter we first show how the plasma glucose level is regulated by the insulin from a top-down point of view, with the main combined experimental-modeling tools which are currently employed in investigating the behaviour of the glucose-insulin system. Then, we detail the chain of biochemical reactions, known as the insulin signaling network (ISN), that give rise to glucose uptake into the cell.

1.1 The regulation of the plasma glucose level by the insulin

The glucose-insulin system can be viewed as a feedback control system with a controller (the pancreas) and multiple effectors (muscle, liver, fat tissue), where the only state variable of interest is the level of glucose in blood (glycemia) that needs to be kept within a narrow range (110 ± 30 mg/dl). Abnormally low glucose concentrations (hypoglycaemia) give rise to anxiety, tremors, aggressiveness, obfuscation, coma and eventually death while, on the other hand, excessive plasma glucose concentrations (hyperglycaemia) produce microvascular damages and neural damages, leading among others to blindness and chronic renal insufficiency.

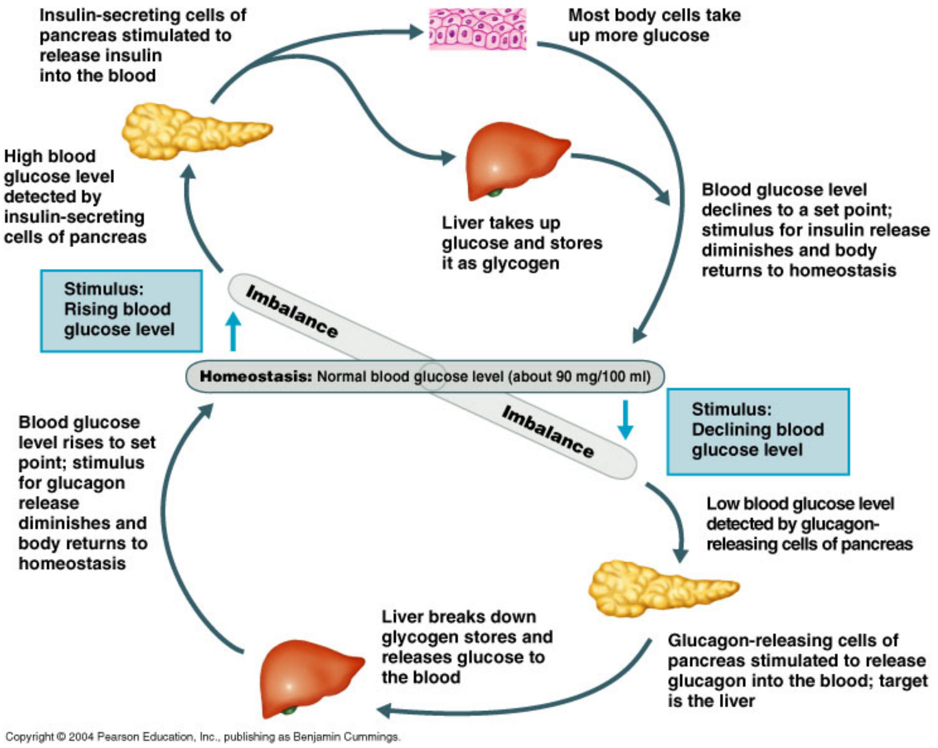

Copyright © 2004 Pearson Education, Inc., publishing as Benjamin Cummings.

Figure 1.1: Action of insulin and glucagon on blood glucose level regulation. If the blood glucose level falls to dangerous levels (as in very heavy exercise or lack of food for extended periods), the alpha cells of the pancreas release glucagon, a hormone that stimulate liver cells to convert glycogen into glucose (*glycogenolysis*) which then is released into the bloodstream.Otherwise, when level of blood sugar rises, whether as a result of glycogen conversion, or from digestion of a meal, insulin is released from beta cells found in the islets of Langerhans in the pancreas. Insulin causes the liver to convert more glucose into glycogen (*glycogenesis*), and to force cells (primarily muscle and fat tissue cells) to uptake glucose from the blood, thus decreasing blood sugar.

The glycemia is monitored and regulated by the cells in the pancreas's islets of Langerhans through the mechanism shown in Fig. 1.1. When insulin secretion by the pancreas is insufficient or absent, due to autoimmune destruction of β-cells, the clinical picture of Type 1 Diabetes (T1D) results; when insulin is secreted in normal, or supranormal amounts, but it is ineffective in lowering glycemia to normal levels, Type 2 Diabetes (T2D) is present. T2D accounts for about 90 to 95 percent of all diagnosed cases and it often begins as insulin resistance, a condition where the body produces insulin, but the cells do not use it properly. As the need for insulin increases, the pancreas progressively loses its ability to produce the hormone. It appears that both genetic and environmental factors are responsible for the progression from normal glucose tolerance to T2D [26, 27].

In the last decades, several works aimed to develop mathematical models of the glucose-insulin system in order to analyze experimental data, to identify and quantify relevant biophysical and biochemical parameters, to design clinical trials and to evaluate diabetes prevention or disease modification therapies. In the literature we find models focused on the pancreatic insulin production, short-term organ/tissue models accounting for the intra-venous and the oral glucose tolerance tests as well as for the euglycemic hyperinsulinemic clamp, and long-term diabetes models aiming to represent disease progression in terms of β-cells population dynamics over a long period of years.

In the following sections we review the main combined experimental-modeling tools which are currently employed in investigating the behaviour of the glucose-insulin system at the organ and tissue levels without getting too deep into the molecular/subcellular details. These models describe the glucose/insulin dynamics from a phenomenological viewpoint, after an external perturbation within a relatively short time period and prove information on goodness of pancreatic insulin secretion and the peripheral glucose uptake in the subject under investigation. The clinical experiments, and the mathematical models aimed at their interpretations, are very interesting since they offer the possibility to estimate a set of key markers of T2D development.

1.1.1 The intra-venous glucose tolerance test (IVGTT)

The intra-venous glucose tolerance test (IVGTT) is a clinical experiment where a glucose bolus is rapidly injected intra-venously into the forearm of a subject. Glucose and insulin samples are acquired in the following 3 h, during which glycemia and insulinemia return to their basal values. The glucose injection is modeled as an instantaneous change in the plasma glucose concentration. In healthy subjects, pancreatic insulin secretion consists of two contributions: a first-phase release, which is a quick response to a sudden change in glycemia, and a second-phase release, which occurs some ten minutes after the bolus injection. The first-phase of insulin response may be modeled as an instantaneous change in the plasma insulin concentration, whereas the second phase is described by the model equations. Many mathematical models exist to represent the dynamics of this process, but the most famous and of still widespread use is the so-called minimal model (m.m.), proposed by Bergman et al. [28]. The m.m., in the first formulation, is composed of two parts: one describing the dynamics of the glucose uptake after the external stimulus, regarding the insulin concentration as a known forcing function; the other describing the dynamics of the pancreatic insulin release in response to the glucose stimulus, with the glucose concentration regarded as a known forcing function. The model equations for the glucose dynamics are:

$$\begin{aligned} \frac{dG}{dt} &= -(p_1 + X(t))G(t) + p_1 G_b, \qquad & G(0) &= G_b + \Delta_G\,, \\ \frac{dX}{dt} &= -p_2 X(t)G(t) + p_3(I(t) - I_b), \qquad & X(0) &= 0\,. \end{aligned} \tag{1.1.1}$$

This two-compartment model shows that the plasma glucose concentration $G(t)$ does not directly depend on the plasma insulin concentration $I(t)$, but on the insulin concentration in a remote compartment, through the auxiliary function $X(t)$, called insulin action, whose dynamics depends on the plasma insulinemia. Δ_G is the instantaneous change of glycemia due to the glucose bolus injection and is computed as the ratio D/V_G, where D is the dose of glucose injected and V_G is the apparent distribution volume of glucose. G_b and I_b are the basal concentrations of blood glucose and insulin, respectively and p_1, p_2, p_3 model parameters.

The second part of the m.m., which is no longer used in the recent applications of the m.m., concerns the insulin kinetics and consists of a single compartment model:

$$\frac{dI}{dt} = -n(I(t) - I_b) + \gamma t[G(t) - h]^+\,, \quad I(0) = I_b + \Delta_I\,. \tag{1.1.2}$$

The insulin kinetics exhibits a linear clearance rate n, and the insulin secretion rate is modeled by a time-varying forcing function proportional (according with the parameter γ) both to the hyperglycemia attained and to the time elapsed from the glucose stimulus. Parameter h is the target glycemia that the actual plasma glucose concentration needs to exceed to stimulate the second-phase pancreatic insulin production. The first phase insulin release is modeled by Δ_I.

The four unknown parameters of m.m. to be estimated from the data (values of glucose and insulin concentration in plasma at given time points) are: p_1 (also denoted as S_G, glucose effectiveness), p_2, p_3 and V_G.

The m.m. has played a crucial role in modeling the glucose-insulin system and, although many criticisms have been raised in the last decade [29], [30], it is still widely used in the clinical practice because of its ability to provide some important markers of insulin efficacy. Among these markers the most important is the insulin sensitivity index, defined as the quantitative influence of basal insulin concentration to increase the glucose effectiveness at steady state, [28]:

$$S_I = \frac{\partial}{\partial I_b}\Big[-\frac{\partial}{\partial G}\frac{dG}{dt}\Big]_{steadystate} = \frac{p_3}{p_2}\,. \tag{1.1.3}$$

1.1.2 The oral glucose tolerance test (OGTT)

The oral glucose tolerance test (OGTT) is a simple clinical test where, after an oral glucose load of 75 g, plasma glucose and insulin concentrations are measured at times 0, 15, 30, 60, 90, 120 and 180min. C-peptide must also be measured to compute indexes of the insulin secretion. The OGTT is currently used to aid diagnosis of glucose intolerance and T2D since this test mimics the physiological conditions of the glucose/insulin system more closely than the Euglycemic hyperinsulinemic clamp (EHC) or the IVGTT. However, the analysis of the OGTT data by a mathematical model is very difficult as the time course of the delivery to plasma of exogenous glucose and even the total amount of glucose delivered are unknown and influenced by several factors. Experimental determinations of the rate of appearance, R_a, of exogenous glucose in plasma have been obtained using a double tracer technique by Ferrannini et al. [31, 32]. The Authors found a similar profile for R_a in healthy subjects and diabetic patients. Other groups reported R_a data during an OGTT or a meal test (MTT) (for instance, see [33]).

A mathematical model, developed with the aim of describing the kinetics of the glucose/insulin system during an OGTT or an MTT, and of estimating the parameters of clinical interest, was proposed by Caumo et al. in [34]. This OGTT minimal model extends to the oral test the basic model proposed for the IVGTT, with the difference that the glucose administration does no longer appear as a bolus dose in the initial condition of the glucose equation, but as the input function R_a, rate of appearance of the exogenous in the plasma. The model equations are as follows:

$$\begin{aligned}
\frac{dG}{dt} &= -(p_1 + X(t))G(t) + \frac{R_a(t)}{V_G}, & G(0) &= G_b\,, \\
\frac{dX}{dt} &= -p_2 X(t) + p_3(I(t) - I_b), & X(0) &= 0\,,
\end{aligned} \tag{1.1.4}$$

where G is the plasma glucose concentration (basal value, G_b), I is the plasma insulin concentration (basal value, I_b), X represents the insulin action and V_G is the glucose distribution volume. In [33] parametric descriptions of the rate of appearance were evaluated. The Authors represented the R_a in (1.1.4) by a piecewise linear function with a given number (n) of break points:

$$R_a(t) = \begin{cases} \alpha_{i-1} + \frac{\alpha_i - \alpha_{i-1}}{t_i - t_{i-1}}(t - t_{i-1}) & t_{i-1} \le t \le t_i\,, i = 1, \ldots, n \\ 0 & otherwise \end{cases}$$

with $t_0 = 0$ and $a_0 = 0$ $\big(R_a(0) = 0\big)$. The a_i values are to be estimated from the glucose concentration data. The a priori identifiability of model parameters is guaranteed if p_1 and V_G are assumed to be known [33].

Several more complex OGTT models were prosed in the literature as, for instance, the models proposed by Breda et al. [35] that considered also the insulin secretion, and the model proposed by Salinari et al. [36] where also the incretin kinetics was taken into account.

1.1.3 Euglycemic hyperinsulinemic clamp (EHC)

The gold standard for investigating and quantifying yhe insulin resistance is the euglycemic hyperinsulinemic clamp (EHC) [37] that measures the amount of glucose necessary to compensate for an increased insulin level without causing hypoglycemia. Indeed, insulin resistance expresses the imbalance between the amount of pancreatic insulin, delivered in response to a glucose load, and the levels of plasma glucose reached. To obtain the same plasma glucose concentration, higher levels of plasma insulin are necessary in insulin-resistant subjects than in normal controls.

EHC is the gold standard method for determining insulin sensitivity, in spite of its long and intensive execution: through a peripheral vein a priming dose of short-acting human insulin is given during the initial 10 min of the test in a logarithmically decreasing manner, in order to raise acutely the plasma insulin to the desired level; thereafter, insulin is infused at 10-120 mU per m^2

per minute and, to compensate for the insulin infusion, glucose is also infused (blood glucose levels have to be between 5 and 5.5 mmol/l); the glucose and insulin levels are monitored every 5 min and every 20 min, respectively, and the rate of glucose infusion is adjusted following an ad hoc algorithm; the rate of glucose infusion during the last 30-60 min of the test determines insulin sensitivity. If high levels (7.5 mg/min or higher) are acquired, the patient is diagnosed insulin-sensitive. Low levels (4.0 mg/min or lower) indicate that the subject is insulin-resistant. Levels between 4.0 and 7.5 mg/min suggest impaired glucose tolerance that may generate insulin resistance.

A mathematical model to explain the oscillations of glycemia occurring in response to the hyperinsulinization and to the continuous glucose infusion at varying speeds characterizing EHC, was proposed in [38].

1.2 The intracellular insulin control of glucose uptake: the insulin signaling network

At the molecular level, insulin regulates glucose homeostasis by stimulating the uptake of the glucose into the insulin sensitive tissues. In addition, insulin also promotes a number of other cellular events including the regulation of ion and amino acid transport, lipid metabolism, glycogen synthesis, gene transcription and mRNA turnover, protein synthesis and degradation, and DNA synthesis [22, 23] (see Fig. 1.2).

The biochemical network that, upon the insulin binding to a specific cell surface receptor, triggers the glucose uptake into the cells is known as insulin signaling network (ISN) [22].

Glucose uptake into the various tissues of the body is accomplished by two general types of glucose transporters, Na^+-dependent and facilitative glucose transporters [39]. Na^+-dependent glucose transporters are present in the intestinal tract and kidney and are not known to be regulated by insulin. Glucose uptake into all other types of tissue is accomplished by the facilitative glucose transporters. Five different facilitative glucose transporters have been identified and are referred to as GLUTl-5. GLUT1 was the first facilitative transporter to be identified, and it is present in placenta, brain, kidney, colon and in lower amount in adipose tissue and muscle. GLUT2 is present predominantly in liver and pancreatic beta-cells and appears to be involved in the glucose-regulated pathway leading to insulin secretion. GLUT 3 is found in multiple tissues including brain, placenta, and kidney.

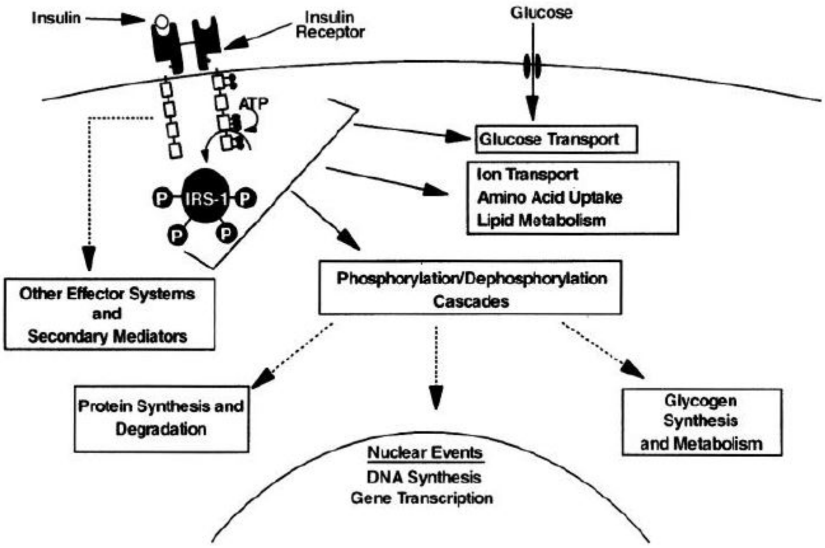

Figure 1.2: Effects of insulin at molecular level. The insulin signaling system affects numerous intracellular processes.

GLUT5 is found predominantly in the small intestine. GLUT1, GLUT3, and GLUT5 are thought to be the major transporters involved in basal glucose uptake. GLUT4 is the only glucose transporter that is regulated by insulin and is found exclusively in the insulin-sensitive tissue cells, i.e. muscle cells, hepatocytes and adipocytes [40]. In the absence of insulin, almost all of the GLUT4 resides in an intracellular vesicular pool. The binding of the insulin to its receptor on the plasma membrane activates a series of cascade reactions of phosphorylation/dephosphorylation (activation/inactivation) that lead to a redistribution of the glucose transporter GLUT4 from the intracellular storage sites to theplasma membrane resulting in an increase in the rate of glucose uptake.

In the following sections, the most important elements of the ISN are examined, giving particular attention to the molecular interactions which govern the dynamics of the metabolic response triggered by insulin. We present in more details the main elements constituting ISN that can be divided in three main subsystems:

1. From insulin binding to PI3K activation;
2. Akt phosphorylation/dephosphorylation;

3. Activation/inhibition of Akt substrates.

1.2.1 From insulin binding to PI3K activation

Insulin action initiates upon insulin binding to its receptor on the cell surface.

The IR belongs to a family of ligand-activated receptors characterized by intrinsic tyrosine kinase activity that includes, in addiction to IR, the insulin-like growth factor-1 receptor (IGF-1R), the insulin receptor-related receptor (IRR), the epidermal growth factor receptor (EGFR), the platelet-derived growth factor receptor (PDGFR) and others. These transmembrane signaling proteins are fundamental regulators of cell differentiation, growth, and metabolism. Generally, each receptor is produced starting from two chains, termed α and β, that are covalently linked by a disulfide bond. The α chains contribute to the formation of ligand-binding domain, while β chains carry the kinase domain. In the case of insulin, two α chains and two β chains are linked together forming a biologically active receptor heterotetramer ($\alpha^2\beta^2$). Figure 1.3 shows the structure of the IR that can be divided in two main parts, the extracellular and the intracellular regions [22]. Although the chains constituting IR are covalently linked, these two domains function independently. The extracellular domain of IR consists of the entire α-subunits and about one third of the β-subunits. This region is responsible for the insulin binding and, precisely, the α-subunits contain the primary ligand-binding site. The intracellular region can be divided into several sub-domains with different functions and characteristics: the juxtamembrane region (JM), that is implicated in regulating the IR internalization; the tyrosine kinase (TK) domain containing the kinase-insert region; and the carboxyl-terminus domain, that contains two autophosphorylation sites.

Upon insulin binding, IR rapidly internalizes with a multistep process and the internalized receptors undergo a sorting that determines whether they will be subjected to degradation in lysosomes or they will recycle back to the membrane surface. The IR on the plasma membrane are phosphorylated on the tyrosine residues. The activation of the insulin receptor Tyr kinase leads to the phosphorylation of several endogenous substrates, including insulin receptor substrates (IRS1, 2, 3, 4), Shc, GA B1, Cbl and others that are phosphorylated on tyrosine residues [41]. Each of these phosphorylated proteins serve as docking proteins for other signaling proteins that

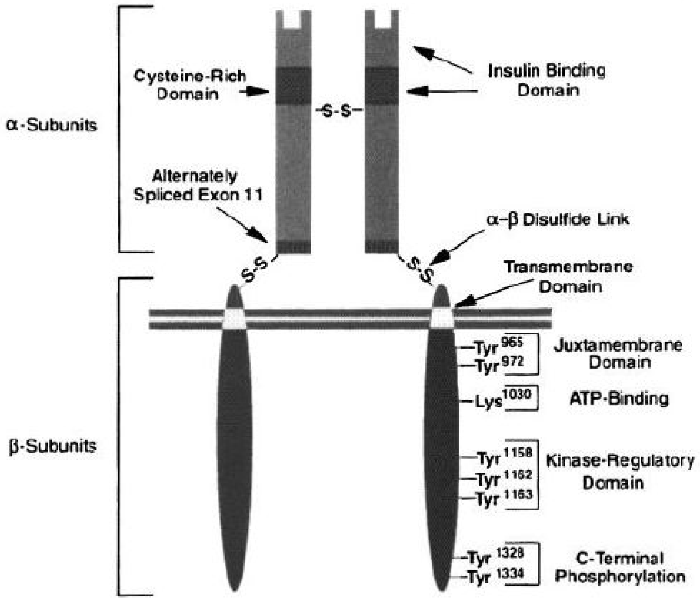

Figure 1.3: Structure of insulin receptor. Model of the insulin receptor showing its various structural and functional domains.

contain the Src-homology-2 domains (SH2 domains). Some SH2 proteins are enzymes, such as the P-Tyr phosphatase SHP2 (SH-PTP2). Other SH2 proteins, such as the p85 regulatory subunit of phosphatidyl-inositide 3-Kinase (PI3K), function as adaptor proteins for downstream effectors that further propagate the metabolic and the growth-promoting effects of insulin.

A number of protein tyrosine phosphatases (PTPases) can dephosphorylate the insulin receptor, reducing its kinase activity and thereby attenuating insulin action. Two PTPases have been implicated in the negative regulation of the insulin receptor, PTP1B and LAR. Elevated expression of each these phosphatases has been reported in the insulin-resistant patients [42].

IRS1 is a high-molecular-weight cytosolic protein, which contains 20 potential tyrosine phosphorylation sites and over 40 potential serine/threonine phosphorylation sites, and has been shown to be a major substrate for both the insulin and IGF-1 receptors [43]. It has a conserved pleckstrin homology (PH) domain that serves to anchor such receptors. IRS1 phosphorylated on tyrosine residues serve as docking sites for SH2 domain-containing the p85 regulatory subunit of PI3K, leading to its activation. Several Ser/Thr phosphorylation sites of IRS1, if phosphorylated, reduce the ability of this protein to interact with the insulin receptor and undergo Tyr phosphorylation thus impairing the insulin signaling and inducing insulin resistance. In particular, the Ser302 phosphorylation of IRS1 by S6-Kinase (S6K) constituting one of the most important negative-feedback loop present in the ISN . This negative feedback inhibits upstream insulin signaling upon mammalian target of rapamycin Complex 1 (mTORC1) and S6K1 activation. Also IRS1, as well as IR, may be dephosphorylated by the PTP1B that thus negatively regulates the insulin signaling pathway.

PI3-kinase plays a central role in the metabolic and growth-promoting actions of insulin [44]. It is a heterodimeric enzyme constitued of a p110 catalytic subunit and a p85 regulatory subunit. The regulatory subunit maintains the p110 catalytic subunit in a low-activity state. Activation of PI3-kinase occurs upon direct interaction of the regulatory subunit with adaptor proteins such as the IRS proteins [43].

1.2.2 Akt phosphorylation/dephosphorylation

The association of p85-p110 complex with IRS molecules results in the production of phosphatidylinositol 3,4,5-trisphosphate (PI(3,4,5)P3) [45, 44] . The most relevant function of PI(3,4,5)P3 is the ability to interact with the phosphoinositide-dependent kinase 1 (PDK1), the protein kinase B (PKB), also known as Akt, and other signaling molecules. These interactions result in the recruitment of these proteins to the plasma membrane triggering changes in their structure, function and their substrate availability. In the case of PDK1, binding of its PH domain to PI(3,4,5)P3 enables it to phosphorylate several downstream effectors, such as protein kinase C (PKC) and PKB/Akt and thus to further propagate the metabolic and growth promoting functions of insulin.

Moreover, two important lipid phosphatases are commonly present in the system and they mainly operate decreasing the levels of PI(3,4,5)P3: the phosphatase and tensin homologue, PTEN, and the SH2 domain containing inositol-5-phosphatase, SHIP2. In particular, PTEN acts removing the phosphate in the 3-position of the inositol ring from phosphatidylinositol PI(3,4,5)P3 to produce PI(4,5)P2. SHIP2 specifically hydrolyzes the 5-phosphate of PI(3,4,5)P3 to produce PI(3,4)P2. Thus both enzymes cooperate as antagonists of the PI3K/Akt/mTOR pathway modulating cell cycle progression and cell survival. PI3K and PDK1 also trigger the activation of the atypical PKC isoforms (PKCζ and PKCλ). Two specific sites, Thr410 and Thr560, need to be phosphorylated for full activation of this molecule which has, as main function, the regulation of GLUT4 translocation to the cellular membrane and subsequent induction of glucose transport inside the cell. PKC plays an important role constituting a negative feedback control mechanism that serves to terminate insulin action. This feedback loop involves the phosphorylation of IRS proteins and leads to IRS dissociation from IR, thereby terminating insulin signaling.

Akt is a serine/threonine-specific protein kinase and is one of the major substrates of PDK1 [41]. It is implicated in mediating numerous aspects of insulin action, including the regulation of glucose transport, glycogen synthesis, protein synthesis, the antilipolytic effects of insulin, as well as cell growth and cell survival induced by insulin [5]. Akt contains a PH domain that allows the binding to PI(3,4,5)P3 following PI3K activity and its targeting to the PM. Akt association with PI(3,4,5)P3 brings it to the proximity of PM facilitating the phosphorylation of Akt at Thr308 by PDK1 while mTORC2 (mammalian target of rapamycin complex 2) catalyzes Akt phosphorylation on Ser473 [6]. The maximal Akt activity seems to be achieved when the molecule is phosphorylated on both Thr308 and Ser473 residues, allowing the translocation to Pm of GLUT4 glucose transporters in muscle and adipose tissue [7, 8, 46]. The protein phosphatase PHLPP dephosphorylates Akt at Ser473 and the phosphatase PP2A dephosphorylates Akt at Thr308. Moreover, Akt may inactivate PTP1B upon phosphorylation at Ser50, which enhances insulin signaling via a positive feedback loop [47]. Indeed, phosphorylation of PTP1B by Akt impairs the ability of PTP1B to dephosphorylate insulin receptors and IRS. As PTP1B itself negatively modulates insulin signaling, the downstream negative regulation of an upstream negative signaling element represents a positive feedback loop for insulin signaling.

1.2.3 Activation/inhibition of Akt substrates

Akt with its phosphorylated forms may be considered the core of the ISN because it promotes the phosphorylation of a series of substrates that play a key role in the regulation of glucose uptake, glycogen and protein synthesis.

The first action is achieved by Akt mediating the translocation of GLUT4 glucose transporter to the cell membrane. This mechanismi involves AS160, which is a Rab GTPase-activating protein, for the translocation and targeting of trasporters to the PM [46], and SNARE regulatory proteins for the fusion event [48]. Despite recent studies tried to uncover this mechanism, several steps in GLUT4 trafficking, including endocytosis and sorting are still unclear.

The glycogen synthesis involves the phosphorylation and inactivation by Akt of glycogen synthase kinase 3β (GSK3β) at Ser9. Phosphorylation at this site causes a conformational change, preventing the access of substrates to the active site. GSK3β acts phosphorylating and inactivating the glycogen synthase (GYS) that has a key role in the conversion of glucose to glycogen. It is also known that the inactivation of GSK3β also plays an important role in the Wnt signalling pathway which is critical for embryonic development [49].

The regulation of protein synthesis implicates the phosphorylation and inhibition of the tuberous sclerosis complex 1/2 dimer (TSC1-TSC2) by Akt. The TSC1-TSC2 complex acts as a GTPase-activating protein (GAP) for the small GTPase Ras homologue enriched in brain (GTP/Rheb) and the primary function of this complex is as a critical negative regulator of mTORC1 activation. Since Akt-mediated phosphorylation of TSC1-TSC2 complex implies the conversion of GTP/Rheb into GDP/Rheb, and GDP-loaded Rheb is unable to activate mTORC1, TSC complex effectively shuts off mTORC1 signaling. Moreover, several studies suggest that the TSC1-TSC2 complex can also positively regulates mTORC2 in a manner independent of its GTPase-activating protein activity toward Rheb. In [11], the Authors found that mTORC2 isolated from a variety of cells lacking a functional TSC1-TSC2 complex was impaired in its kinase activity toward Akt. The defect in the mTORC2 activity in these cells was found to be separated from the known feedback mechanisms (via mTORC1) affecting IRS1 and then PIP3 that it is recognized as a mTORC2 activator [9].

The mammalian target of rapamycin (mTOR) is considered as a central controller of cellular metabolism and also of cellular growth. In the past few years, several studies focused on mTOR functions have revealed its crucial involvement in the onset and progression of diabetes, cancer and ageing [15, 9]. In particular, mTOR regulates the anabolic and catabolic processes, including translation, ribosome biogenesis and autophagy, in response to hormones, growth factors (insulin), nutrients (amino acids), energy and stress signals. Deregulation of the mTOR pathway occurs in several human disease [50, 51, 52]. Small molecules that target mTOR are becoming of great clinical interest in view of their ability to arrest the growth of the cancer.

Over-stimulation of the mTOR pathway by excess food consumption may be a crucial factor underlying the diabetes epidemics. Recent findings suggest that mTOR signalling controls the rate at which cells and tissues age, and then inhibiting mTOR may represent a promising avenue to increase longevity.

mTOR is the catalytic subunit of the two distinct complexes mTORC1 and mTORC2, which are involved in different biological processes as schematically represented in Figure 1.4.

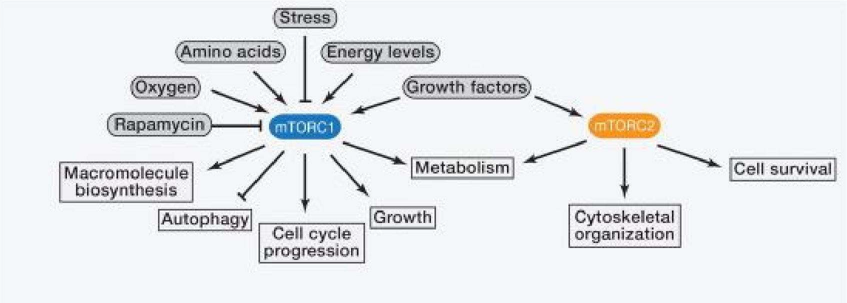

Figure 1.4: mTORC1 and mTORC2 complexes. mTORC1 responds to amino acids, stress, oxygen, energy, and growth factors and is acutely sensitive to rapamycin. It promotes cell growth by inducing and inhibiting anabolic and catabolic processes, respectively, and also drives cell-cycle progression. mTORC2 responds to growth factors and regulates cell survival and metabolism, as well as the cytoskeleton. mTORC2 is insensitive to acute rapamycin treatment but chronic exposure to the drug can disrupt its structure.

mTORC1 is constituted by the DEP domain-containing mTOR-interacting protein (DEPTOR), the mammalian lethal with SEC13 protein 8 (mLST8 or GβL), the regulatory-associated protein of mTOR (RAPTOR) and the 40 kDa Prorich Akt substrate (PRAS40). mTORC2 has DEPTOR and mLST8 in common with mTORC1 but, differently from it, contains the rapamycin-insensitive companion of mTOR (RICTOR) and the mammalian stress-activated map kinase interacting protein 1 (mSIN1).

mTORC1 is the better characterized of the two mTOR complexes while much less is known about the mTORC2 [5]. Activated mTORC1 up-regulates protein synthesis by phosphorylating key regulators of mRNA translation and ribosome synthesis. mTORC1 substrates are the S6-kinase (p70-S6K), the translation initiation regulator 4E-binding protein (4E-BP) and the mTORC1-inhibitor PRAS40. Activation of p70-S6K is regulated by a wide range of extracellular signals including growth factors, hormones, nutrients (glucose and amino acids), and stress. Works from many research groups have revealed the complexity of S6K1 activation via sequential phosphorylation at multiple sites [53, 54]. The best characterized sites are Thr-229 (T229) and Thr-389 (T389) and it is known that PDK1 and mTOR can phosphorylate T229 and T389, respectively. In particular, mTORC1 phosphorylates T389, creating a docking site for PDK1, which is then able to phosphorylate the activation loop T229. More recently, it has been found that Ser-371 (S371) is essential for T389 phosphorylation and S6K1 activity [15]. However, it remains unclear how the S371 phosphorylation is regulated. Fully actived p70-S6K is an important element in insulin pathway also because of the phosphorylation and the inhibition it carries out on IRS. Precisely, p70-S6K phosphorylates IRS at multiple serine residues, resulting in the accelerated degradation of IRS. Thus it constitutes a negative-feedback loop that inhibits upstream insulin signaling. The action of this negative feedback is widely described in the literature (see, for instance, [2, 4, 55, 56]).

Unphosphorylated 4E-BP1 suppresses mRNA translation. More precisely, when phosphorylated by mTORC1 at Thr37, Thr46, Ser65 and Thr70, 4E-BP1 dissociates from the eukaryotic translation initiation factor 4E (eIF4E), which is involved in several cellular processes including enhanced translational efficiency, splicing, mRNA stability, and RNA nuclear export.

PRAS40 contributes to the inhibition of mTORC1 activity [57, 58]. In response to insulin, mTORC1 phosphorylates PRAS40 at Ser183 and this action causes the release of PRAS40 from the complex and relieves its inhibitory effect on mTORC1 which is allowed to phosphorylate the remaining substrates. Moreover, also Akt phosphorylates PRAS40 so causing it to bind to cytosolic anchor proteins and preventing it from inhibiting mTORC1 [59].

In addition to regulating the production of proteins, mTORC1 controls the synthesis of lipids required for proliferating cells to generate membranes [60]. In yeast and mammals, an important mTOR inhibitor is rapamycin that inhibits the ability of mTORC1 to phosphorylate its substrates [61]. Rapamycin binds the small protein 12 kDa FK506-binding protein (FKBP12) and, in turn, rapamycin-FKBP12 binds and inhibits the kinase activity of the RAPTOR-bound mTOR. Because acute treatment with rapamycin does not perturb mTORC2 signaling and rapamycin-FKBP12 cannot bind to intact mTORC2, this complex was originally thought to be rapamycin insensitive [62]. However, the situation turns out to be much more complex as long term treatment with rapamycin reduces mTORC2 signaling in some, but not all, cell types and does so by suppressing mTORC2 assembly [63].

In general, the upstream and downstream regulators of mTORC2 are less characterized compared to mTORC1. Recent findings have revealed mTORC2 mediates the phosphorylation of Akt at Ser473 and then it is important for the full activation of Akt [6]. mTORC2 may favour cell survival through Akt-mediated inhibition of the forkhead box protein O1 (FOXO1) and FOXO3: phosphorylation of FOXO1 and FOXO3 by Akt effectively prevents them from translocating to the nucleus and activating the gene expression programmes that promote apoptosis. Moreover, mTORC2 activates PKC-α that regulates cell shape in cell-type-specific fashion by affecting the actin cytoskeleton [62].

1.2.4 Pathologies related to dysfunctions of the insulin signaling network

The previous sections have stressed as the ISN components have key roles, not only in the glucose metabolism, but also in other important cellular processes such as apoptosis, cell proliferation, transcription and cell migration. Malfunctioning of the ISN may alter these physiological processes of cells, potentially leading to severe consequences on the organism. So, investigating the mechanisms responsible for insulin signaling impairment is of primary importance. The most common pathologies caused by an altered ISN are the insulin resistance, T2D and cancer [5, 15, 52]. Moreover, insulin resistance is often associated with central obesity, hypertension, and atherosclerosis, and diabetes involves many long-term complications including heart diseases, strokes, diabetic retinopathy, kidney failure and poor circulation in the limbs which may lead to amputations.

A detailed analysis of regulatory processes in the ISN may permit to develop new insights about the origin of these pathologies and, in future perspective, to find a drug or combination of drugs able to counterbalance the effect of the diseases. Such purpose has been followed by several research groups in the last decades. For instance, Guertin et al. [64] demostrated that the development of prostate cancer caused by Pten delection in mice requires mTORC2, but that for normal prostate epithelial cells, mTORC2 activity is nonessential. So, the selective requirement for mTORC2 in tumor development suggests that mTORC2 inhibitors may be of substantial clinical utility. Chresta et al. [65] studied the in vivo and in vitro antitumour activity of AZD8055, a potent mTOR inhibitor. In [55], the Authors showed how the absence of S6K1 protects against age- and diet-induced obesity while enhancing insulin sensitivity.

Chapter 2

Mathematical modeling of cell signaling networks and parameter estimation in biochemical pathways

Biochemical pathways are the molecular mechanism involved in the various physiological and cellular processes of the living systems. These pathways can be categorized into three major groups: metabolic, signaling and gene regulatory networks, which control the expressions of some sets of genes, proteins or chemical compounds to regulate different phenotypic expressions. Therefore, the study of the various biochemical pathways is very important to identify their roles in several human diseases, such as cancer or diabetes.

Signaling pathways are complex, interdependent cascades of signals that sense input stimuli (e.g. extracellular ligands or intracellular metabolites) and transmit, process, and integrate this information to provide output signals that accordingly regulate the cell activity. Signaling networks permit cells to communicate with each others and with external environment and to undergo phenotypic changes, such as cellular division, differentiation, death and others. Hence, these networks can be considered as information processing devices that translate input signals into output signals in which information is often coded by concentrations, modifications, and localization of proteins, either in the stationary levels or in temporal patterns. In biological systems, signal transmission occurs mostly through two mechanisms: (i) protein-protein interactions and enzymatic reactions such as protein phosphorylation and dephosphorylation, (ii) protein degradation or production of intracellular messengers.

Despite substantial progresses over the past three decades in biochemistry, molecular biology and cell physiology, together with emerging techniques for detecting protein-protein interaction, the construction and the analysis of cellular signaling networks remains too complicated for the human mind.

The complexity of the signal transduction pathways inside the cells derives not only from the enormous amount of different molecules involved in the process but also from the presence of numerous feedback and feedforward loops, both negative or positive, concerning the pathway itself, and the crosstalks involving distinct pathways. For instance, a negative feedback loop can give rise to adaptation and desensitization, while a positive feedback loop can lead to emergent network properties such as ultrasensitivity and bistability [1] [66]. Furthermore, cellular components rarely function in just one location, but dynamically shuttle between cellular organelles [67, 68]. The network resulting from multiple interactions and dynamic localization enables the cells to process information in a context-dependent manner.

Due to this high degree of complexity, it has been necessary to develop mathematical models to more deeply understand the system behavior of signaling networks, and to predict higher order functions that can be validated by the experiments.

In the present chapter, different types of mathematical representations for the modeling of the signaling networks are described and the advantages and disadvantages of each type are discussed. Then, we discuss the main problems arising in the assessment of model parameter values and the most common methods used to estimate the parameters from the experimental data.

2.1 Mathematical tools for modeling regulatory cellular networks

Experimental biology alone may not provide a strategy for a detailed analysis of complex signaling networks, that instead requires a combination of experimental and computational approaches including the development and analysis of mathematical models. This is the idea at the basis of *Systems Biology.* Kitano [69] states “to understand complex biological system requires the integration of experimental and computational research - in other words a

---

[1] In biological context, a system exhibiting bistability might shift from ‘low’ to ‘high’ steady state in response to a signal of sufficient duration and amplitude.

systems biology approach.” Computational methods provide useful information to guide experimental design, whereas data collected from experiments help the implementation and refinement of computational models, providing more accurate predictions on the behaviour of biological systems.

Computational methods used to study cell signaling networks are typically classified into two main categories: structural and dynamic network analysis [70].

Structural network analysis depicts the regulatory network as a connection map (makes use of graph theory), in which the nodes represent the distinct chemical species populating the system, and the edges (with sign) their interactions. The aim is to give information about the network connectivity and to deduce some properties of the global network as well as some functions of the individual proteins. An advantage of these models is that they can be developed for large numbers of components and interactions. However, these connection maps are largely qualitative and then have limited use in understanding how networks behave dynamically in space and time.

An example of structural analysis is the boolean method. In the boolean model the signal transduction is discretized and can be either present or absent. This two-states modeling represents an extreme simplification of the underlying biochemistry and cannot be used to predict the time course of protein concentrations.

Dynamic network analysis utilizes the network connectivity information and makes use of the kinetic parameters characterizing the biochemical reactions in order to determine how the system changes in time and spaceunder external stimulation. Kinetics parameters, also known as kinetic rate constants, give information about the speed of a chemical reaction and thus about how fast the reactants are transformed into products.

Typically, the dynamic models are built in three steps. The first step is to generate a connection map and to identify regulatory features. After writing out the reaction schemes and collecting the necessary parameters, the modeler generates the mathematical model using the appropriate framework. Once the simulations have been performed, comparison between in silico and *in vivo/in vitro* experiments enables the estimation of the parameters that are not experimentally accessible with the current technology. Finally, the model has to be validated. Besides verifying whether a proposed molecular mechanism is correct, modeling identifies major regulatory hubs of signaling networks, and helps to uncover possible targets for the pharmacological intervention in diseases.

However, even though the dynamic models are more informative than the structural models, they require the additional knowledge of a large number of numerical values describing the kinetics of the reactions. The implementation of dynamic models easily presents problems due to the limited data available from experiments. Moreover, the values of kinetics parameters often depend on cell type, experimental conditions and other factors. These values may differ of a order of magnitude from test to test, and in some cases they may remain under-determined or non-uniquely estimated. Despite these difficulties, dynamic models are widespread and they have been currently used by many research groups with successful results.

Broadly, the mathematical models used to describe the dynamics of biochemical reactions can be *deterministic* or *stochastic*. In deterministic models, the change in time of the components' concentration is completely determined by specifying the initial, and in some cases, boundary conditions. By contrast, the changes in concentration of components with respect to time cannot be fully predicted in stochastic models. During a given period, the reaction might or might not occur and the probability of occurrence is related to the kinetic rate constant.

The choice of the modeling methodology depends on the cellular process that is being investigated and the experimental tools that are available. Deterministic models are a good description when the distributions of reactants can reasonably be assumed to be continuous. This holds when the number of molecules is large enough ($> 10^2 - 10^3$ molecules per reactant)[71]. In the eukaryotic metabolism and signal transduction, these numbers justify the use of deterministic kinetic models. On the other hand, the use of a stochastic model is necessary for problems in which fluctuations have a significant role, such as in phenotypic variations and in gene regulation. The biochemical fluctuations or 'noise' inherent in such stochastic systems are often exploited in cellular functions, resulting in spontaneous switching from one biochemical state to another [72].

In the following, we focus mainly on the deterministic models describing the three most commonly used types, that is: chemical kinetics models, compartmental models, and diffusion-reaction models [73].

2.1.1 Chemical kinetics models

The most commonly used approach to model cellular signaling networks uses the formalism derived from the chemical kinetics theory. The governing equation that describes the dynamics of a signaling network component X has the form:

$$\frac{dX}{dt} = production - consumption \tag{2.1.1}$$

The equation above states that the rate of change in concentration of any molecule (called substrate) is equal to the difference between the rate of production and the rate at which it is consumed. The generation and consumption terms can be a constant (e.g., synthesis), first order reactions (e.g., degradation), or nonlinear (e.g., second order reactions or Michelis-Menten kinetics for enzymes). Chemical kinetics models are implemented using a set of ordinary differential equations (ODEs) where the only independent variable is the time. In these models, the concentrations of chemicals are assumed to be independent of space. The advantage of ODE-based models is that, although analytical solutions are not guaranteed (in most cases, it cannot be obtained), various numerical methods for solving ODEs systems are well developed.

An example of a chemical kinetics model is the *mass action law* that states that the rate of any chemical reaction is proportional to the product of the masses of the reacting substances, with each mass raised to a power equal to the coefficient that occurs in the chemical reaction. Thus, for instance, a bimolecular reaction, $A + B \xrightarrow{k} C$, proceeds at a rate proportional to the product of the concentrations of the substrates, $k[A][B]$ (the squares brackets denote concentrations).

Michaelis-Menten kinetics

In biochemistry, Michaelis-Menten (MM) kinetics is one of the best-known models of enzyme kinetics. It involves an enzyme E binding to a substrate S to form a complex C, which in turn may give back the substrate or be converted into a product P plus the unmodified enzyme [74]. MM kinetics may be represented schematically as

$$S + E \underset{k_d}{\overset{k_a}{\rightleftharpoons}} C \xrightarrow{k_c} P + E \tag{2.1.2}$$

where k_a, k_d, and k_c denote, respectively, the association, dissociation and catalytic rate constants. The double arrows between S and C represent the fact that enzyme-substrate binding is a reversible process whereas the final catalytic step is irreversible. The MM scheme in (2.1.2) is used in a variety of biochemical situations other than enzyme-substrate interaction, including antigen-antibody binding, DNA-DNA hybridization, and protein-protein interaction [75].

Applying the mass action law to the two chemical reactions in (2.1.2), we can write the following system of four non-linear ordinary differential equations:

$$\begin{cases} \dfrac{dS}{dt} = -k_a ES + k_d C \\ \dfrac{dE}{dt} = -k_a ES + k_d C + k_c C \\ \dfrac{dC}{dt} = k_a ES - k_d C - k_c C \\ \dfrac{dP}{dt} = k_c C \end{cases} \tag{2.1.3}$$

with the initial conditions:

$$\begin{aligned} S(0) &= S_{tot}\,, \\ E(0) &= E_{tot}\,, \\ C(0) &= 0\,, \\ P(0) &= 0\,, \end{aligned} \tag{2.1.4}$$

and the conservation laws

$$S_{tot} = S + C + P\,, \tag{2.1.5}$$

$$E_{tot} = E + C\,. \tag{2.1.6}$$

The quantities S, E, C, P are time-dependent concentrations. Note that, because of (2.1.5)-(2.1.6), the system (2.1.3) of four ODEs can be reduced to a system of only two non linear differential equations with the corresponding initial conditions:

$$\begin{cases} \dfrac{dS}{dt} = -k_a(E_{tot} - C)S + k_d C & S(0) = S_{tot}\,, \\ \dfrac{dC}{dt} = +k_a(E_{tot} - C)S - (k_d + k_c)C & C(0) = 0\,. \end{cases} \tag{2.1.7}$$

The systems (2.1.3) cannot be solved in closed form, but only numerically, for any specific values of the initial conditions and the kinetic parameters. Actually, it would be very useful to have a closed form expression for the rate of the reaction $S \to P$, because that expression could be compared to the experiments and the rate constants could be determined.

Michaelis and Menten [74], in their original analysis, assumed that the substrate is in instantaneous chemical equilibrium (*equilibrium approximation*) with the complex and derived an approximate formula. In particular, they assumed

$$k_a E S = k_d C \, .$$

Combining the above expression with the enzyme conservation law (2.1.6), they obtained

$$k_a(E_{tot} - C)S = k_d C \, .$$

and then

$$C = \frac{E_{tot} S}{K_d + S} \, ,$$

with $K_d = k_a/k_d$. Hence, the velocity v of the reaction (the rate at which P is formed) is:

$$v = \frac{dP}{dt} = \frac{V_{max} S}{K_d + S} \tag{2.1.8}$$

where $V_{max} = k_c E_{tot}$ is the maximum reaction velocity, obtained as S tends to infinity.

In 1925, the British botanist G. E. Briggs and the British geneticist J. B. S. Haldane undertook an alternative analysis of the system (2.1.3) [76]. They assumed that the concentration of the intermediate complex does not change on the time-scale of product formation, that is, the dynamics of the complex is faster than the substrate dynamics. Mathematically, this assumption, known as the *standard quasi-steady-state approximation* (sQSSA), means that:

$$\frac{dC}{dt} = 0 \Rightarrow k_a E S = k_d C + k_c C \tag{2.1.9}$$

Combining this relationship with the enzyme conservation law (2.1.6), the concentration of complex is given by

$$C = \frac{E_{tot} S}{K_m + S} \,,$$

where

$$K_m = \frac{k_d + k_c}{k_a} \tag{2.1.10}$$

is the so-called Michaelis-Menten constant. Thus, the reaction rate v becomes

$$v = \frac{dP}{dt} = -\frac{dS}{dt} = \frac{k_c E_{tot} S}{K_m + S} \,. \tag{2.1.11}$$

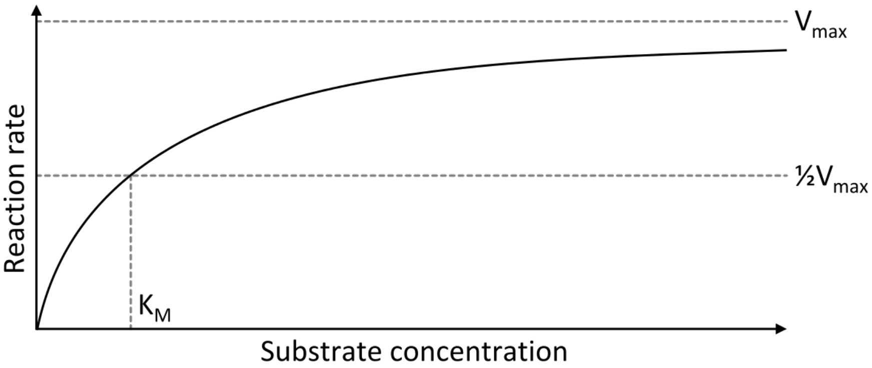

Figure 2.1: Michaelis-Menten saturation curve for an enzyme reaction showing the relation between the substrate concentration and the reaction rate.

The reaction rate increases with the substrate concentration and asymptotically tends to its maximum $V_{max} = k_c E_{tot}$, attained when all the enzyme is bound to substrate (Figure 2.2). The constant k_c, the turnover number, is the maximum number of substrate molecules converted to product per enzyme molecule per second, and the constant k_c/K_m (catalytic efficiency) is a measure of how efficiently an enzyme converts a substrate into the product. The MM constant K_m represents the substrate concentration at which the reaction rate is at half of V_{max} and is an inverse measure of the affinity of the substrate for the enzyme (a small K_m indicates high affinity, meaning that the rate will approach V_{max} more quickly).

The parameters V_{max} and K_m describe completely the kinetics of a MM reaction in sQSSA and they can be computed from experiments [77]. The advantage of the sQSSA is that it reduces the dimensionality of the system (2.1.3) and thus speeds up the numerical simulations, especially for large networks as found *in vivo*. Moreover, the kinetic constants k_a, k_d, k_c are usually unknown, whereas finding the kinetic parameters K_m and V_{max} is a standard *in vitro* procedure in biochemistry [77].

The resulting reaction rates predicted by the two approaches (*equilibrium approximation* vs sQSSA) are similar, with the only difference that the equilibrium approximation defines the constant as K_d, whilst the quasi-steady-state approximation uses K_m (see (2.1.8) and (2.1.11)). However, each approach is founded upon a different assumption. The Michaelis-Menten equilibrium analysis is valid if the substrate reaches equilibrium on a much faster time-scale than the product is formed or, more precisely, if

$$\frac{k_a}{k_c} \ll 1\,.$$

By contrast, the Briggs-Haldane quasi-steady-state analysis is valid if:

$$\frac{E_{tot}}{K_m + S_{tot}} \ll 1\,, \tag{2.1.12}$$

i.e., the total enzyme concentration must be much lower than the sum of the total substrate concentration and the MM constant[78, 79].

According to the procedure described by Segel [78], the first step in attempting to determine the parameter ranges for which the sQSSA is valid is to estimate two time scales. Recalling that the simplifying assumptions of the sQSSA are that the complex dynamics is faster than the substrate dynamics and that during this fast complex transient the substrate does not decrease appreciably, we have: τ_f, the time that characterizes the duration of the fast transient, and τ_s, the time interval required for a significant change in S during the post-transient period (see Figure 2.2).

The estimated values are (see [78] for the details):

$$\tau_f = \frac{1}{k_a(S_{tot} + K_m)} \tag{2.1.13}$$

and

$$\tau_s = \frac{\textit{total change in } S \textit{ after fast transient}}{max\{|\dot{S}|\}\textit{after fast transient}}\,. \tag{2.1.14}$$

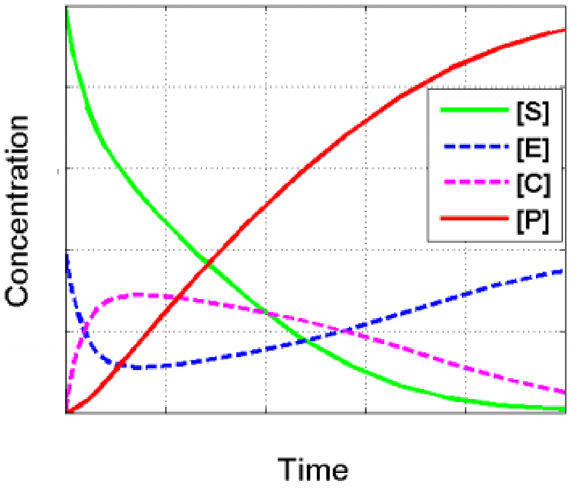

Figure 2.2: Time-concentration profiles of enzyme E, substrate S, complex C and product P in a Michealis-Menten model.

Assuming the validity of the steady state assumption, the numerator of (2.1.14) is approximately S_{tot} and the denominator is given by (2.1.11) with $S = S_{tot}$, i.e.:

$$\tau_s = \frac{S_{tot} + K_m}{k_c E_{tot}} \,. \tag{2.1.15}$$

The first condition necessary for the sQSSA is $\tau_f \ll \tau_s$ that, from (2.1.13) and (2.1.15), implies:

$$\frac{E_{tot}}{S_{tot} + K_m} \ll \left(1 + \frac{k_d}{k_c}\right)\left(1 + \frac{S_{tot}}{K_m}\right) \tag{2.1.16}$$

Secondly, to insure that $S(0) = S_{tot}$ can be taken as initial condition, there must be only a negligible decrease ΔS in the substrate concentration during the fast transient, i.e. $|\Delta S / S_{tot}| \ll 1$ during τ_f. Overestimating the decrease ΔS by the product of the initial maximal rate of depletion of S, $k_a E_{tot} S_{tot}$ (obtained by setting $t = 0$ in the first equation of (2.1.3)) with the time duration τ_f, yields

$$\left|\frac{\Delta S}{S_{tot}}\right| = \frac{1}{S_{tot}} \left|\frac{dS}{dt}\right|_{max} \cdot \tau_f = \frac{E_{tot}}{K_m + S_{tot}} \ll 1 \,. \tag{2.1.17}$$

If (2.1.17) holds then (2.1.16) holds. Thus, it is demonstrated that (2.1.12) guarantees the validity of the steady state assumption.

The condition (2.1.12) is usually fulfilled for the *in vitro* experiments, but often breaks down *in vivo* [80].

In order to simulate physiologically realistic *in vivo* scenarios, Borghans et al. [81] recently introduced the *total quasi steady-state approximation* (tQSSA) and showed that it is valid for a broader range of parameters covering both high and low enzyme concentrations. The term *total* refers to the fact that the tQSSA yields an equation for the total substrate concentration ($\bar{S} = S + C$ becomes the new substrate variable).

Several recent papers have reviewed and extended the results by Borghans et al. [80, 82, 83, 84]. Tzafriri rederived and corrected the tQSSA both for irreversible enzyme kinetics [80] and for reversible enzyme kinetics [82]. Pedersen et al [83, 84] extended the tQSSA to more complex reaction schemes, as the fully competitive reactions, the double phosphorylation, and the Goldbeter-Koshland switch [2].

We avoid to discuss further about the tQSSA because, as shown in the following chapters, the ISN model proposed in this thesis was developed and analysed assuming the sQSSA. This assumption is justified by the fact that the experimental data used for the parameter estimation are *in vitro* data and, as stressed above, the condition (2.1.12) is usually fulfilled for *in vitro* experiments.

We conclude this section with two remarks.

First, in general, in an enzymatic process the product formation can be reversible but the irreversibility is a necessary simplification in order to yield a tractable analytic solution [82]. Thus, the enzyme reaction is more correctly described as

$$S + E \underset{k_{-1}}{\overset{k_1}{\rightleftharpoons}} C \underset{k_{-2}}{\overset{k_2}{\rightleftharpoons}} P + E \tag{2.1.18}$$

The assumption of irreversibility is correct in situations where one of the below condition is true:

- the concentration of substrate is very much larger than the concentration of products ($S \gg P$);

---

[2] Goldbeter-Koshland switch [85] is used to describes the cycle of phosphorylation and dephosphorylation of a substrate, that is one the most important processes to activate and inactivate enzymes in all intracellular pathways.

- the energy released in the reaction is very large.

These conditions are true *in vitro* and for many *in vivo* biological reactions, particularly when the product is continually removed by a subsequent reaction. In situations where neither of these two conditions hold (that is, the reaction is low energy and a substantial pool of product(s) exists), the MM scheme in (2.1.2) breaks down, and more complex modeling approaches explicitly taking the forward and reverse reactions into account must be considered to understand the enzyme biology.

The last remark is linked to the observation that, in biochemistry and pharmacology, the binding of a ligand to a macromolecule is often enhanced if other ligands are already present on the same macromolecule (the so-called cooperative binding) [86]. If we want to represent this enhancement for a substrate having more than one binding site, the Michaelis-Menten equation (2.1.11) is no longer appropriate to study the rate of reaction. Indeed, the plot of the reaction rate as function of the substrate assumes a sigmoidal shape instead of the hyperbolic one reported in Figure 2.2.

The first description of the cooperative binding to a multi-site protein was developed by A.V. Hill [87], who suggested the following equation:

$$Y = \frac{[X]^n}{K + [X]^n}\,, \tag{2.1.19}$$

where Y is the fraction of the ligand-binding sites on the receptor protein, $[X]$ is the free (unbound) ligand concentration, K is an apparent dissociation constant, and n is the so-called Hill coefficient. The total number of ligand binding sites is an upper bound for n. If $n < 1$, the system exhibits negative cooperativity, whereas the cooperativity is positive if $n > 1$. A coefficient $n = 1$ indicates that the affinity of the enzyme for a ligand molecule is not dependent on whether or not other ligand molecules are already bound.In the latter case, the Hill equation has the form of the Michaelis-Menten equation normalized with respect to the maximal reaction rate (see Eq. (2.1.11)).

2.1.2 Compartmental models

The basic limitation in using equations such as (2.1.1) to describe a complex system, such as a subcellular system, is the assumption of spatial homogeneity. However, since the activity of biological molecules is often controlled by their microenvironment, it is desirable to incorporate this feature into the models. The simplest way to take into account the spatial distribution of some quantities in a system is by making a compartmental approximation.

In a compartmental model, the molecules in different compartments are treated as separate species. The exchange of molecules among compartments is modeled as a flux, which is determined from either a priori knowledge of the biology or from empirical observations. Compartmental modeling has been used extensively in the modeling of dynamical systems in biology and medice, and more recently, in the modeling of networks involved in protein secretion and trafficking (e.g. [88]).

For a component X that dynamically shuttles between the plasma membrane and the cytoplasm, (2.1.1) might be extended as:

$$\begin{aligned}\frac{dX_{PM}}{dt} = &\, production - consumation \\ &- export\ to\ cytoplasm + membrane\ recruitment \end{aligned} \tag{2.1.20}$$

Similar equations can be written for the concentrations of components in the cytoplasmic compartment. Thus, like the chemical kinetics models, compartmental models are also based on ordinary differential equations (ODEs). However, for the cases where the explicit dependence on the spatial variables is needed, a partial differential equation (PDE)-based model has to be used (see, for instance, [89]).

As the same component in different compartments is described by different equations, the biological realism of the model increases along with the computational complexity of the model. Moreover, the experimental complexity increases because it becomes necessary to use the flux terms that must be estimated from indirect measurements. Currently, the flux terms are estimated by means of experiments that use the photoactivation of labeled proteins.

2.1.3 Diffusion-reaction models

At a more fine-grained level, the spatiotemporal dynamics of cellular components can be modeled by the reaction-diffusion equation:

$$\frac{\partial X}{\partial t} = D\frac{\partial^2 X}{\partial x^2} - \nu\frac{\partial X}{\partial x} + R \tag{2.1.21}$$

where X is the concentration of the molecule, t is time, D is the diffusion coefficient, x is the spatial variable, ν is the convective velocity, and R is the rate of generation and consumption. The diffusion-reaction models are based on partial differential equations (PDEs) because the concentrations depend on multiple independent variables, in the case of (2.1.21) time and one space variable. Physically, Equation (2.1.21) states that the rate of change of concentration of a component at any particular location depends on diffusion (the first term), active transport or convection (second term), and biochemical reactions (the last term).

PDE problems can require many more parameters compared to ODE problems. Indeed, in addition to the initial concentrations and kinetics parameters, PDE-based models require the diffusion coefficients, and the mandatory specification of concentration and/or flux at the boundary. Moreover, PDE problems require far greater computational skills, resources, and time than their ODE counterparts.

2.2 Assessment of the parameter values from the experimental data

One of the greatest hurdles in the modeling of the biological systems is the estimation of the parameter values [90]. Values for specific parameters measured in vivo are rare and the parameters are often estimated from experimental measurements made in vitro or by fitting of model equations to the available experimental data.

The minimum requirements for modeling the biochemical reactions using chemical kinetics models are the concentrations of the signaling components at the basal state and the kinetic parameters, such as the forward and backward reaction rates. Currently, these values exist only for a small fraction of the enzymatic and chemical reactions occurring within any cell of interest. Furthermore, even in cases where the rate constants are measured, the experiments are usually performed in vitro with purified components. The interactions may have largely different kinetics in vivo, because many biological reactions take place on cell scaffold, microdomains, or PM, that essentially increase the local concentrations of the reactants. Thus far, techniques for measuring rate constants and concentrations of reactants in their natural compartmentalized environment have not generally available.

A further key area of research is the multidimensional parameter estimation. Because of the paucity of quantitative data, it is often necessary to estimate several parameters from a single dose-response curve or a single concentration time course. As the number of parameters to be estimated increases, the difficulty and the time required for parameter estimation also increase.

In general, a simple data set consists of n points $(x_i, y_i), i = 1, \dots, n$ where x_i is the independent variable and y_i is the dependent variable which is measured. The relationship between x and y is described by the regression model

$$y = \bar{y}(x, \theta) + v, \tag{2.2.1}$$

where $\bar{y} \in R^n$ is the input-output function of the model that describes a set of specific dynamic/mechanicistic assumptions, $\theta \in R^m$ is the vector of the (deterministic) unknown parameters and $v \in R^n$ represents the measurement (random) error assumed with mean zero. As well as v, y is a stochastic vector. Moreover, the regression model (2.2.1) can be linear or non-linear, depending on whether the model function $\bar{y}(x, \theta)$ is or is not a linear combination of the parameters in θ.

If n data points are observed, with $n < m$, the classical approaches of the regression analysis cannot be used since the system of equations defining the regression model is underdetermined and there are not enough data to recover θ.

If exactly $n = m$ data points are observed, and the function $\bar{y}$ is linear in θ, the system $y = \bar{y}(x, \theta)$ can be solved exactly rather than approximately. Indeed, we have to solve a set of n equations with n unknowns (the elements of θ), which has a unique solution as long as the x are linearly independent. If $\bar{y}$ is non linear in θ, a solution may not exist, or many solutions may exist.

The most common situation is when $n > m$ data points are observed. In this case, the regression model results an overdetermined system in θ and in principle there is enough information in the data to estimate a value for θ that best fits the measurements.

Let us show some of the most common methods to determine the unknown parameter vector θ from the available data using the regression model in (2.2.1).

2.2.1 Maximum likelihood method

In the regression model (2.2.1), if the probability distribution of the vector v, and then of y, is known, the estimator of the paramenter vector θ, denoted by $\hat{\theta}$, can be obtained by the *Maximum Likelihood Method* (MLM) [91]. Given the probability distribution of y, $f(y;\theta)$, the *Maximum Likelihood Estimator* (MLE) of θ is defined as the value of θ that maximizes the so called likelihood function $L_y(\theta) = f(y;\theta)$.

For instance, let us suppose that v has a Gaussian distribution with mean zero and covariance matrix Σ, independent of θ and known. Thus, also the observation vector y has a Gaussian distribution with mean $\bar{y}(\theta)$ and covariance matrix Σ. To obtain the MLE $\hat{\theta}$, we need to maximize with respect to θ the likelihood function

$$L_y(\theta) = \frac{1}{(2\pi)^{n/2}(det\Sigma)^{1/2}}\exp\left(-\frac{1}{2}[y-\bar{y}(\theta)]^T\Sigma^{-1}[y-\bar{y}(\theta)]\right). \qquad (2.2.2)$$

Equivalently, we can minimize the function -ln$L_y(\theta)$ that, as Σ is known, means to minimize, with respect to θ, the index

$$R(\theta) = [y-\bar{y}(\theta)]^T\Sigma^{-1}[y-\bar{y}(\theta)]\,. \qquad (2.2.3)$$

Note that the estimator $\hat{\theta}$ is unique if $n \geq m$, i.e. the number of available data points is larger than the number of unknown parameters.

MLE enjoys good asymptotic properties. Under not particularly restrictive conditions and when the sample size tends to infinity, the MLE has the properties of: 1) *consistency*, i.e. the estimator $\hat{\theta}$ converges in probability to the true value; 2) *asymptotic normality*, i.e. the distribution of $\hat{\theta}$ tends to the Gaussian distribution with mean θ and covariance matrix Σ; 3) *efficiency*, i.e. the estimator achieves the Cramér-Rao lower bound (its covariance matrix Σ is equal to the inverse of the Fisher information matrix). The property of efficiency guarantees that no consistent estimator has lower asymptotic mean squared error than the MLE (or other estimators attaining the Cramér-Rao bound).

In the study of biochemical models, because of the complexity of the measurements processes, it is very difficult to assign a specific probability distribution to the measurement errors and then the application of the maximum likelihood method is not allowed. When the error distribution is unknown, the most common method used to fit the model equations to the experimental data is the Least Squares Method.

2.2.2 Least squares method

The *Least Squares Method* (LSM) determines the unknown parameter values minimizing the sum of squared residuals, i.e. the differences between the model-based predictions and the observed values. Thus, a problem of parameter estimation solved by the LSM coincidesin general with an optimization problem in which the objective function is:

$$\textit{obj(parameters)} = (\textit{model output - data})^2\,,$$

where the squared term prevents the negative deviations from canceling out the positive deviations.

Let us now introduce the different types of *Least Squares Estimator* (LSE) [91].

Let us consider the generic ODE model

$$\dot{x} = f(x, \theta)\,,$$

where x is the state vector and θ the parameter vector. The observed value of the model output is described by the measurement equation (2.2.1) with the only assumption $E[v] = 0$. As no other information about the distribution of v is known, the simplest way to determine θ from the available data is to find the value $\hat{\theta}$ which minimizes the distance $||y - E(y)||^2$, where $E(y) \equiv E(\bar{y}(\theta)) \equiv \bar{y}(\theta)$ is the expected value of y, i.e. the cost function

$$R(\theta) = [y - \bar{y}(\theta)]^T [y - \bar{y}(\theta)] = \sum_{i=1}^{n} (y_i - \bar{y}_i(\theta))^2 \tag{2.2.4}$$

Such estimator $\hat{\theta}$ is called *Ordinary Least Squares Estimator* (OLSE).

The OLSE is a particular case of the so called *Generalized Least Squares Estimator* (GLSE) or *Weighted Least Squares Estimator*(WLSE) defined as

$$\hat{\theta}_{GLS} = \min_{\theta} \left([y - \bar{y}(\theta)]^T W^{-1} [y - \bar{y}(\theta)] \right)\,, \tag{2.2.5}$$

where W is a symmetric and positive defined matrix.

Denoting by $Cov(v)$ the covariance matrix of the error v in (2.2.1), defined as

$$Cov(v) = E[vv^T] = E[(y - \bar{y}(\theta))(y - \bar{y}(\theta))^T]\,, \tag{2.2.6}$$

it is easy to verify that, if $W = Cov(v)$ and v has a Gaussian distribution, GLSE coincides with the MLE (see(2.2.3) and (2.2.5)). We recall that, in view of central limit theorem, the errors can be considered approximately normally distributed when the dimension of data set n increases.

Under the assumption that the errors $v_i, i = 1, \ldots, n$ are uncorrelated each other, i.e. $Cov(v)$ is diagonal and each non-zero element is the variance $\sigma_i^2, i = 1, \ldots, n$ of the i-th component of the error vector, the GLSE becomes

$$\hat{\theta} = \min_{\theta} \sum_{i=1}^{n} \frac{(y_i - \bar{y}_i(\theta))^2}{\sigma_i^2}\,. \tag{2.2.7}$$

Obviously, if the variance of the errors is constant over the observations we obtain again the OLSE.

Both the OLSE and the GLSE can be linear or non-linear function of θ.

In the linear least squares, the model function $\bar{y}(x, \theta)$ of (2.2.1) must be linear with respect to the parameters, not necessarily with respect to the state variable. This means that, even if the model is linear in x, the fitting of the data can require the non linear least squares estimator if the state matrix contains the parameters.

The linear least-squares problem is convex and has a closed-form solution that is unique, provided that the number of data points used for fitting equals or exceeds the number of unknown parameters. Indeed, given the regression model

$$y = X\theta + v, \tag{2.2.8}$$

where $y \in R^n$, $\theta \in R^m$, $m \leq n$, X is a matrix nxm with the m coloumns linearly independent, and v a random vector with mean zero, the GLSE, $\hat{\theta}_{GLS}$, is

$$\hat{\theta}_{GLS} = (X^T W X)^{-1} X^T W y\,, \tag{2.2.9}$$

i.e. the value of θ that minimizes $[y - X\theta]^T W^{-1} [y - X\theta]$.

Obviously, for the linear OLSE Eq. (2.2.9) holds with $W = I$.

The linear OLSE is important in view of the Gauss-Markov Theorem that states:

Theorem 2.2.1 *In a linear regression model in which the errors have zero expectation, are uncorrelated, and have equal variance, the best linear unbiased estimator (BLUE) of the coefficient vector is given by the OLSE as it is the most efficient as compared to other unbiased, linear estimators.*

Unfortunately, the problem of parameter estimation in the biochemical pathways is often non-linear, so that it must be solved by using numerical algorithms that minimize the sum of squared residuals iteratively until some convergence criteria are satisfied. Moreover, the optimization problem can be non-convex with multiple optima for the objective function.

2.3 Sensitivity analysis in systems biology modeling

In the previous section, we stressed that one of the main hurdles in the development and identification of mathematical models of biological systems is that a large number of model parameters remain unknown and difficult to be estimated. In most cases, parameter estimates are associated with significant uncertainty, and examining the influence of these uncertainties on the model behaviour is crucial to enhance the predictive capacity of the model and to generate hypotheses about the biological mechanisms. Therefore, each model should be checked with respect to its sensitivity to parameter changes.

The term *sensitivity analysis*(SA) refers to an important tool used to determine how parameter changes influence the system behaviour and to identify those parameters that have the greatest impact on the system output both in steady and transient states. Moreover, SA can allow to simplify high dimensional models that arise in systems biology and can be used to indicate prospective molecular targets for new drugs.

A good overview of the sensitivity methods and their applicability can be found in [90]. Here, we give only few hints about these methods.

In general, there are two main classes of SA, local and global [92]. The local sensitivity analysis (LSA) investigates the effect on the system output of a small deviation in a single parameter around its nominal value. Global sensitivity analysis (GSA) describes the effects of simultaneous parameter variations over relatively wide ranges, and allows us to explore the effects of interactions among the parameters.

2.3.1 Local sensitivity analysis

Let us consider the generic non linear ODE model used to describe the dynamic behaviour of a cell signaling network:

$$\frac{dX}{dt} = f(X, u, \theta)\,, \tag{2.3.1}$$

where $X = [x_1\ x_2 \dots x_n]^T$ is the state vector with x_i denoting the molar concentration of molecules of type i, u is an input variable and $\theta \in R^m$ contains the model parameters (i.e. the kinetic constants).

The LSA is not related to the experimental measurements and, therefore the state is considered to be the output. In particular, the model output is the solution of (2.3.1), $X(\theta_n, t)$, where θ_n denotes the nominal parameter vector.

Denoting by x_i the i-th state in X and by θ_j the j-th parameter in θ, the effect of the change in parameter θ_j on a species of interest x_i can be expressed by a Taylor series expansion:

$$x_i(\theta_j + \Delta\theta_j, t) = x_i(\theta_j, t) + \sum_{j=1}^{m} \frac{\partial x_i}{\partial \theta_j}\Delta\theta_j + \frac{1}{2}\sum_{l=1}^{m}\sum_{j=1}^{m} \frac{\partial^2 x_i}{\partial\theta_l \partial\theta_j}\Delta\theta_l\Delta\theta_j + \dots \tag{2.3.2}$$

In the expression (2.3.2), the partial derivatives $\partial x_i/\partial\theta_j$ are called the first order local concentration sensitivity coefficients, while $\partial^2 x_i/\partial\theta_l\partial\theta_j$ are the second-order local concentration sensitivity coefficients, etc. Normally, only the first-order sensitivity coefficients are considered.

The absolute sensitivity matrix is defined as

$$S = \frac{\partial X}{\partial \theta} = \begin{bmatrix} s_{11} & s_{12} & \dots & s_{1m} \\ s_{21} & s_{22} & \dots & s_{2m} \\ \vdots & \vdots & \ddots & \vdots \\ s_{n1} & s_{n2} & \dots & s_{nm} \end{bmatrix} \tag{2.3.3}$$

where the first order sensitivity coefficients

$$s_{ij} = \frac{\partial x_i}{\partial \theta_j}\,, \tag{2.3.4}$$

are actually sensitivity functions (as they change in time) describing the influence of the j-th parameter on the time course of the i-th state variable.

The matrix S can be obtained by computing the partial derivatives in

(2.3.4) if the analytical solution of (2.3.1) is available. Unfortunately, this is very rare for cell network systems whose dynamics is described by complex nonlinear ODEs. Therefore, in these cases, numerical methods have to be applied to obtain S at each sample time.

One of the most commonly used numerical methods applies the finite difference approximation, computing the sensitivity coefficient s_{ij} by means of the difference between the nominal and perturbed solution [93]

$$s_{ij}(t) = \frac{\partial x_i(t)}{\partial \theta_j} \cong \frac{x_i(\theta_j + \Delta\theta_j, t) - x_i(\theta_j, t)}{\Delta\theta_j}\,. \tag{2.3.5}$$

Obviously, for $\Delta\theta_j \to 0$, we obtain the definition of derivative. This method is straightforward in that only the calculation of x_i is required with the nominal and the perturbed parameter value, even if the numerical values obtained may vary significantly with the size of $\Delta\theta_j$.

In the models describing biological systems, the parameters as well as the state variables may take values that are distributed over several orders of magnitude. Therefore, instead of the absolute sensitivities, the relative sensitivities defined as

$$\bar{s}_{ij} = \frac{\partial x_i}{\partial \theta_j} \cdot \frac{\theta_j}{x_i} \tag{2.3.6}$$

are often considered. Such normalization makes it possible to compare the relative influence of any parameter change on system behaviour, regardless of the scale of either the parameter or the state variable. The analysis of the relative sensitivities allows to:

- check which parameters are relevant for the steady state and which for the transient dynamics;
- create a ranking of parameters indicating, consequently, which processes are the most important for the behaviour of the signaling network and also providing suggestions for experimental research;
- find correlations among parameters so to simplify the parameter estimation of the model.

For the ranking of the parameters, it is necessary to define cumulative indices that can be calculated either for each state variable separately, or for the whole system [92]. In particular, the cumulative effect of the j-th parameter on the i-th state variable can be measured as

$$S_{ij}^{*} = \frac{1}{T}\int_{0}^{T} |s_{ij}(\tau)| d\tau \,, \tag{2.3.7}$$

where T denotes the time horizon of the simulation, or:

$$S_{ij}^{*} = \frac{1}{N}\sqrt{\sum_{k=1}^{N} |s_{ij}(k)|^2} \,, \tag{2.3.8}$$

where N denotes the number of integration steps in the simulation and the sum includes the consecutive values of s_{ij} computed in the simulation.

Similarly, the overall effect of the j-th parameter change on the whole system can be measured as

$$S_{j}^{tot} = \sum_{i=1}^{n} S_{ij}^{*} \,. \tag{2.3.9}$$

2.3.2 Global sensitivity analysis

In a generic system, multiple parameters can be changed simultaneously and some of these changes can increase and some decrease the effect on the system behaviour compared with the change of a single parameter. To capture the general sensitivity of the system, several methods for global sensitivity analysis (GSA) have been developed. Most of them consist in simulation of the model for a large number of parameter sets and subsequent interpretations of the results. So, the sampling methods of the parameter space has a key role for the good performance of GSA. Usually, for signaling network models, parameter values are randomly generated from: i) a normal or Gamma distribution, if the nominal value of the parameter has already been determined or known from literature; ii) a uniform distribution, defined on a wide range of biologically acceptable parameters, if the parameters are not known.

Afterwards, one of the following methods is applied [92, 94]:

- calculating local sensitivities for each simulation and subsequently averaging them over all simulations;
- variance-based sensitivity methods, where

- the ratio of a model output variance to its average value is calculated and then used as a sensitivity index, or
- the variance of a model output is decomposed into partial variance contributes caused by changes in individual parameters, and the sensitivity indices are subsequently derived from the ratio of the partial variance to the total variance of model output.

Among the variance-based sensitivity methods, the most known is the so called Sobol's method widely detailed in [95]. In few words, this method calculates two kinds of sensitivity indices: one is a first-order sensitivity that measures the fractional contribution of the change of a single parameter to the variance of the output; the other is the total effect sensitivity, or the sum of all the sensitivities involving the model inputs of interest over the full range of parameters values explored.

However, we do not detail the various GSA methods further because, in the present thesis, the sensitivity analysis of the ISN was performed through LSA methods (see Chapter 4). Works devoted to the GSA, dealing with both theoretical and pratical aspects, can be found in the literature [92, 93, 96, 97].

Chapter 3

Mathematical modeling of the insulin signaling network

The ISN represents a typical example of complex signaling network because of the large number component molecules and the various types of interactions between these elements. This complex network of interacting elements can be described by means of a mathematical model to analyse in detail its dynamics. The resulting model can be used to make predictions of the behaviour of the signaling pathway in physiological/pathological states and to test hypotheses leading to a deeper understanding of the process. In the previous chapter, we have shown that the dynamic models of cell signaling networks are commonly described by a system of ordinary differential equations (ODEs) as (2.3.1). An important property of these systems is that for any time t all variables are non-negative.

Starting from some of the best known models of the insulin signaling network proposed in the literature, we present in this chapter the mathematical model used in the present thesis to analyze the available experimental data. Such model explicitly represents many known insulin signaling components and incorporates feedback pathways, both positive and negative.

3.1 State of the art

In the last decades, several studies have investigated the behavior of the ISN by mathematical models and analysis of experimental data providing new insights at different levels, for instance: (i) insulin binding to the insulin receptor [98, 16], (ii) insulin signaling and cellular responses [17], and (iii) integration of intracellular insulin signaling with whole-body glucose homeostasis [99].

Following the seminal papers of Wanant and Quon [16] and of Sedaghat et al. [17], some studies focused on the response to a step increase of the extracellular insulin concentration and give the time course of the protein phosphorylation/dephosphorylation reactions, whereas in other studies the dose-response curves, i.e., the steady state concentrations at given insulin levels, are considered.

The transient response of insulin binding and the subsequent autophosphorylation of insulin receptor have been described in [16, 17, 100, 101, 19]. In particular, the complex mathematical model proposed by Kiselyov et al. [100] accounted for both the high and low affinity sites in the two monomers of insulin receptor. Brännmark et al. [101] studied possible schemes that explain the peculiar behavior observed in the phosphorylation of insulin receptor and insulin receptor substrate. More complete dynamical models, supported by the analysis of the time-course of protein concentrations after insulin stimulation, were developed and investigated in [12, 18, 19].

Based on previous models of insulin-IR binding [16] and regulation of the insulin sensitive glucose transporter GLUT4 [98], Sedaghat et al. [17] built a mathematical model of insulin signaling that contained most of the accepted mechanisms and intermediates in downstream signaling to control the glucose uptake. This model contains kinetic equations from the insulin receptor (including the binding of two insulin molecules and the cytosolic IR pool) up to PIP3, PKC, and total phosphorilated Akt(pAkt). Intracellular and surface GLUT4, and both negative and positive feedback loops were included. Model parameters were assessed from literature data of 3T3-L1 adipocytes and the model response to a 15 min insulin pulse was computed. In addition, a comparison of steady-state surface GLUT4 against literature data is also reported.

The model in [17] was extended to include amino acids, the mammalian target of rapamycin, and some other aspects of the signaling network by Vinod et al. [102].

A more complete scheme of the ISN was investigated in [19]. The model proposed by Brannmark et al. [19] is based on data of adipocytes isolated from subcutaneous adipose tissue of patients with T2D and non-diabetic subjects. Data consist of the time course of IR and IRS1 up to PKB/Akt, mTORC1 and mTORC2, S6K and S6, AS160 and GLUT4 together with glucose uptake, after insulin stimulation. Dose-response data were also obtained. In adipocytes from T2D patients compared to control the Authors found that the positive feedback from mTORC1 to IRS1(Ser307) was reduced to 15% of control and IR and GLUT4 concentrations were reduced to 55% and 50% of control, respectively. The response to rapamycin was used for model validation.

Other studies focused maily on the steady state of the ISN system, using experimental data of the insulin dose-response curve, which can be more easily determined and are available in the literature for a variety of cells (mainly adipocytes and skeletal muscle cells). Giri et al. [20] and Wang [21] studied the behavior of the dose response curves of the components of the insulin signaling pathway versus the extracellular insulin concentration, with the aim of determining the conditions that produce a hysteresis in the curves as the result of the interactions between negative and positive feedback loops present in the system. In [20], many of the signaling intermediates and parameters were re-used from the Sedaghat model [17]. The main finding was bi-stability, in other words, the notion that two steady-states might coexist for given parameters and constant insulin stimulation. However, no experimental validation of the results was presented. By applying singularity analysis, in [21] regions of the model parameters were identified that correspond to diabetes and cancer.

Some preliminary attempts to link the insulin signaling models with models of glucose homeostasis have recently been published [103], [104], [105], [18]. Such multi-level models are important because diseases emanate from, and drugs act at, the intracellular molecular level, whereas diseases are manifested and diagnosed at the whole-body level. In [18], a minimal model of the insulin signaling in the adipose tissue was analyzed using constraints from a whole-body glucose homeostasis model developed by Dalla Man et al. [106]. Nyman et al.[18] considered, as inputs, the interstitial glucose and the insulin concentrations of the tissue and, as output, the glucose uptake computed by the minimal model.

In other works, the crosstalking of the ISN with other pathways, such as the epidermal growth factor (EGF) signaling and the MAP kinase pathway [107], have been also studied.

3.2 The ISN model proposed to analyse the available experimental data

The model proposed in this thesis represents the main protein-protein interactions of the PI3K-Akt-mTOR pathway, according to the current view of ISN [17, 4, 5, 108]. The model, reported in Figure 3.1, includes negative feedback loops to IRS1 and Rictor, plus a positive feedback to PTP1B, but it does not include (among others): the intracellular pool of IR and the IR recruitment to plasma membrane (PM); phosphatidylinositol 4,5-bisphosphate PI(4,5)P2 with the phosphatase SHIP; the transport of PDK1 and Akt from cytosol to PM; the complex TSC1/TSC2 that, stimulating the conversion from the active GTP-Rheb to the inactive GDP-Rheb, acts as a functional unit in the suppression of mTORC1 activity [4]; the possible mTORC2 activation by TSC2 [11, 51]. Similarly, we did not include the activation of S6K1 by GSK3 [53] and the protein kinase C (PKC) action on GLUT4 translocation [3]. .

Our model concentrats particularly on the single and double phosphorylation of Akt, because recent studies have shown that its action on glucose uptake is maintained almost unaltered when it is phosphorylated only on Thr308, while Akt phosphorylation on Ser473 seems to have a key role in the oneset of insulin resistance [13] and in the cancer development [5, 9]. Moreover, we assumed that mTORC2 activation may also be promoted independently by a putative factor which is related to signaling from the proximal small intestine and possibly operates through the IGF-1 receptor. Such hypothesis is based on the clinical observation that bariatric surgery, a procedure in which a portion of the stomach and of the small intestine are removed or bypassed, induces a remission of T2D very soon after surgery and far too early to be attributed to weight loss [109], [110], [14]. The mechanisms responsible for the improvement in glycemic control after bariatric surgery are still not well understood but, as bariatric operations reroute food through the upper small intestine, an hypothesis can be that gastrointestinal removal or bypass reduce the production of putative intestinal factor/s inducing insulin resistance. Such hypothesis was experimentally tested by Salinari et al. in [13] where the Autors collected experiments in non-diabetic mice both in vivo and in muscle biopsies, and in L6 cells exposed to a medium enriched with proteins secreted by the small intestine of diabetic rats and to serum from insulin resistant humans. The Authors found that jejunal factor/s in-

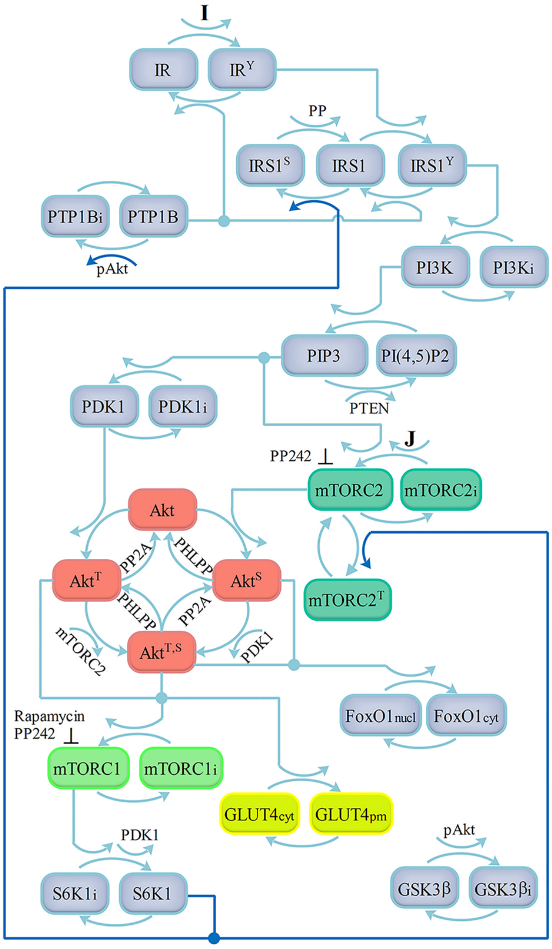

Figure 3.1: Scheme of the insulin signaling network model. Activation by insulin I of IR catalyzes tyrosine phosphorylation of IRS1. Phosphorylated IRS1 binds the p85 regulatory subunit of PI3K, activating the p110 catalytic subunit. PI3K mediates phosphorylation of PI(4,5)-bisphosphate (PIP2) to PI(3,4,5)-trisphoshpate (PIP3) near PM and PTEN dephosphorylates PIP3 back to PIP2. PIP3 recruits Akt and PDK1 to PM, where PDK1 phosphorylates Akt at Thr308 (phosphatase PP2A). mTORC2 is activated by PIP3 and by the jejunal factor J, and catalyzes Akt phosphorylation on Ser473 (phosphatase PHLPP). Maximal Akt activity is achieved when the molecule is phosphorylated on both Thr308 and Ser473 residues, allowing translocation of GLUT4 glucose transporters to PM. GSK3 and FoxO1 are direct Akt substrates. Akt also activates mTORC1, which in turn activates S6K1. Activated S6K1 phosphorylates IRS1 and Rictor in negative feedback loops. The positive feedback loop from Akt to PTP1B is also included. Feedback loops are represented by bold lines. Points of action of rapamycin and PP242 are also shown.

duce insulin resistance and that these factors activate mTORC2, as revealed by an increased value of Ser473 Akt phosphorylation, even in the absence of insulin stimulation.

Most of the reactions in the scheme of Fig. 3.1 are represented by the classical Michaelis-Menten scheme (see Chapter 2) composed of the reversible formation of complex E:S of substrate S and enzyme E, with k_a and k_d the association and the dissociation constant, respectively. The complex C undergoes an irreversible catalytic step with catalytic constant k_c that leads to product P [85, 111, 112]. Since substrates and enzymes are continuously synthesized and degraded within the cell, synthesis and degradation rates were also accounted for in the mathematical model, and denoted by the symbols b and, respectively, μ (endowed with the suitable subscripts). The synthesis rate and degradation rate constants were assumed to not change with time and do not depend on the insulin signal. This assumption may fail during chronic insulin treatment: e.g., after 12 h treatment, IRS1 amount is reduced to 13.6% of control level in 3T3-L1 adipocytes [113]. However, experimental data and model simulations of insulin signaling pathway ([17], [18], [19]) show that the response to a step insulin increase may reach a steady state within a shorter time, so the horizon is here limited to times that do not include these long-range changes. Moreover, we assumed that the degradation rate constant of the complex enzyme-substrate is negligible compared with the sum of dissociation and catalytic constants according to the observations in [114]. This assumption allowed us to write the model equations in a simpler form.

In addition, we assumed that: i) an (approximate) steady state of insulin signaling is attained in cells in culture; ii) intracellular localization (e.g., cytosolic vs. membrane-associated) and compartmentalization (for instance, see [115]), as well as intracellular trafficking, can be neglected; iii) similarly, the presence of isoforms (for instance the three isoforms of Akt [116]) was not considered ; iv) interactions with other receptors (e.g., IGF-1 receptor) and signaling pathways (e.g., effects of nutrient supply on mTOR/S6K1, see [55] are also neglected; v) protein complexes (e.g., mTORC1 and mTORC2) are treated as simple molecular components.

The network model was developed in three stages: first, we established the chemical reactions that characterizes the network; then, as our goal was to investigate the factors affecting the basal concentrations and the dose-response curve of the main components of ISN, we derived the concentrations of the chemicals at the steady-state from the kinetic equations; finally, to reduce the number of unknown parameters, we rewrote the steady-state concentrations in a normalized form.

3.2.1 Reactions within the PI3K-Akt-mTOR network

In the following, we detail the chemical reactions that are included in the network shown in Fig. 3.1.

IR phosphorylation/dephosphorylation with inhibition of dephosphorylation by pAkt

Insulin binding and autophosphorylation of the insulin receptor IR upon insulin binding have been described by complex mathematical models in [16, 17, 20, 101, 18, 100]. Kiselyov et al. [100] accounted for both the high and the low affinity site in the two IR monomers and Cedersund et al.[101, 18] investigated possible schemes that explain the transient response. In the present model, the binding of one or two insulin molecules to IR, as well as the receptor internalization and recycling, are neglected. Phosphorylation at multiple tyrosine residues is here treated as one-site phosphorylation. Insulin binding and receptor autophosphorylation are represented according to the reaction scheme (phosphate group omitted)

$$\mathrm{I} + \mathrm{IR} \leftrightarrows \mathrm{C}_0 \to \mathrm{I} + \mathrm{IR}^{\mathrm{Y}} \tag{3.2.1}$$

where I denotes insulin, IR the free insulin receptor, C_0 the complex IR:I and IR^{Y} the tyrosine-phosphorylated, but still insulin-bound, insulin receptor. The reaction constants are denoted by k_{0a}, k_{0d}, k_{0c} and $K_{m,0} = (k_{0d} + k_{0c})/k_{0a}$. Spontaneous IR autophosphorylation at zero insulin (according to [101]), that leads to $\mathrm{IR}^{\mathrm{Y}}_{\mathrm{b}}$, is regulated by a phosphorylation rate constant, k_b.

As shown in Fig. 3.1, IR dephosphorylation occurs via PTP1B [117]. It has also been found that PTP1B may be inactivated upon phosphorylation at Ser50 by Akt, so that insulin signaling may be enhanced via a positive feedback loop [17, 47]. IR dephosphorylation and the possible inactivation of PTP1B by the phosphorylated Akt, pAkt (possibly Akt phosphorylated at Ser473 and Thr308), may be described by the following reactions:

$$\mathrm{IR}^{\mathrm{Y}} + \mathrm{PTP1B} \quad \leftrightarrows \quad \mathrm{C}_1 \to \mathrm{IR} + \mathrm{PTP1B} \tag{3.2.2}$$

$$\mathrm{pAkt} + \mathrm{PTP1B} \quad \leftrightarrows \quad \mathrm{C}_{\mathrm{P}} \to \mathrm{PTP1B}_{\mathrm{i}} + \mathrm{pAkt} \tag{3.2.3}$$

where $\mathrm{C_1}$ is the complex $\mathrm{IR^Y : PTP1B}$ with k_{1a}, k_{1d}, k_{1c} the reaction constants and $K_{m,1} = (k_{1d} + k_{1c})/k_{1a}$. The same reaction constants also regulate the complex $\mathrm{IR_b^Y : PTP1B}$, denoted by $\mathrm{C_1'}$. $\mathrm{C_P}$ is the putative complex of PTP1B with the inhibitor pAkt, with k_{Pa}, k_{Pd}, k_{Pc} the reaction constants and $K_{m,P} = (k_{Pd} + k_{Pc})/k_{Pa}$, and $\mathrm{PTP1B_i}$ is the inactive form of PTP1B. The inverse transition $\mathrm{PTP1B_i} \to \mathrm{PTP1B}$ is simply regulated by a rate constant k_{-P}. Similar symbols will be used in the following reactions.

IRS1 phosphorylation/dephosphorylation with serine phosphorylation by mTORC1 signaling

For the phosphorylation/dephosphorylation of IRS1 we consider, according to [17], two coupled cycles that account for IRS1 phosphorylation at tyrosine and serine residues. Several IRS1 serine residues are phosphorylated by downstream kinases: IRS1 is phosphorylated at Ser318 by the atypical protein kinase C_ζ, at Ser632 by mTORC1, at Ser302 by the S6K1, at Ser9 by GSK3 [3]. To simplify, we assume that IRS1 is only phosphorylated at Ser302 by the activated S6K1 (Ser302 phosphorylation by S6K1 disrupts IRS1 ability to interact with activated IR, [15, 118]), whereas it is phosphorylated at tyrosine residues by $\mathrm{IR^Y}$. We have:

$$\mathrm{IRS1 + IR^Y} \leftrightarrows \mathrm{C_2} \to \mathrm{IRS1^Y + IR^Y} \tag{3.2.4}$$

$$\mathrm{IRS1^Y + PTP1B} \leftrightarrows \mathrm{C_3} \to \mathrm{IRS1 + PTP1B} \tag{3.2.5}$$

$$\mathrm{IRS1 + S6K1} \leftrightarrows \mathrm{C_4} \to \mathrm{IRS1^S + S6K1} \tag{3.2.6}$$

$$\mathrm{IRS1^S + PP} \leftrightarrows \mathrm{C_5} \to \mathrm{IRS1 + PP} \tag{3.2.7}$$

where IRS1 is the unphosphorylated insulin receptor substrate-1, $\mathrm{IRS1^Y}$ is the tyrosine phosphorylated IRS1, and PTP1B dephosphorylates $\mathrm{IRS1^Y}$. PP is a protein serine phosphatase. $\mathrm{C_2, C_3, C_4}$ and $\mathrm{C_5}$ are the complexes $\mathrm{IR^Y : IRS1}$, $\mathrm{IRS1^Y : PTP1B}$, $\mathrm{IRS1 : S6K1}$ and $\mathrm{IRS1^S : PP}$, respectively, with $k_{ia}, k_{id}, k_{ic}, i = 2, 3, 4, 5$ the respective reaction constants and $K_{m,i} = (k_{id} + k_{ic})/k_{ia}, i = 2, 3, 4, 5$. IRS1 phosphorylation at serine residues represents a negative feedback, widely described in the literature (see, for instance, [2, 55, 56, 4]). The formation of complex $\mathrm{C_P}$ by reaction (3.2.3) with the PTP1B inactivation represents a putative positive feedback since it attenuates $\mathrm{IR^Y}$ and $\mathrm{IRS1^Y}$ dephosphorylation (see reactions (3.2.2) and (3.2.5)) and enhances insulin signaling.

PI3K activation/deactivation

The formation of PI3K occurs through the recruitment of the catalytic subunit p110 to the PM and the p110 binding to the regulatory subunit p85. Both steps of the process are assumed to be regulated by a complex IRS1Y/p85. We have:

$$\mathrm{IRS1^{Y}/p85 + p110_{cyt}} \leftrightarrows \mathrm{C_6^{'}} \rightarrow \mathrm{IRS1Y/p85 + p110_{PM}} \leftrightarrows \mathrm{C_6} \rightarrow \mathrm{IRS1^{Y} + PI3K} \tag{3.2.8}$$

where $\mathrm{C_6^{'}}$ and $\mathrm{C_6}$ are the complexes and the kinetic constants are defined accordingly. Transport of p110 from PM to cytosol and deactivation of PI3K occur according to rate constants $k_{-6}^{'}$ and k_{-6}. PI3K activation by IRS-independent mechanisms can also occur upon growth factor stimulation (IGF-1 and EGF receptor signaling, see [119, 108]).

Phosphatidylinositol phosphates and PDK1

PI3K phosphorylates the phosphatidylinositol 4,5-bisphosphate PI(4,5)P2 on the $3^{'}$–position to form the second messenger PI(3,4,5)P3 (PIP3), whereas PIP3 dephosphorylation to PI(4,5)P2 occurs through the phosphatase and tensin homologue PTEN $3^{'}$–lipid phosphatase [120]. We neglect PIP3 formation from PI(3,4)P2 and the SHIP1/2 phosphatases. PIP3 activates the PDK1 [4] and then the following reactions can be written:

$$\mathrm{PI(4,5)P2 + PI3K} \leftrightarrows \mathrm{C_7} \rightarrow \mathrm{PIP3 + PI3K} \tag{3.2.9}$$

$$\mathrm{PIP3 + PTEN} \leftrightarrows \mathrm{C_8} \rightarrow \mathrm{PI(4,5)P2 + PTEN} \tag{3.2.10}$$

$$\mathrm{PIP3 + PDK1_i} \leftrightarrows \mathrm{C_9} \rightarrow \mathrm{PIP3 + PDK1} \tag{3.2.11}$$

$\mathrm{C_7, C_8, C_9}$ denote the complexes in (3.2.9)-(3.2.11) and the kinetic constants are defined accordingly. The transition from active to inactive form of PDK1, $\mathrm{PDK1_i}$, is regulated by the rate constant k_{-9}.

Activation/deactivation of mTORC2

It is currently accepted that the mTOR complex 2 (mTORC2) is the kinase that promotes Akt phosphorylation at Ser473 ([6]). As suggested in [9], PIP3 may activate mTORC2, reaction (3.2.12). The inverse transition to the inactive form, $\mathrm{mTORC2} \rightarrow \mathrm{mTORC2_i}$, is regulated by a rate constant k_{-10}. We assume that mTORC2 activation is also promoted independently by a factor, J in the reaction (3.2.13), which is related to signaling from the proximal small intestine and possibly operates through the IGF-1 receptor

[13]. The inverse transition is regulated by the rate constant k_{-11}. We have:

$$\mathrm{mTORC2_i + PIP3} \leftrightarrows \mathrm{C_{10}} \rightarrow \mathrm{mTORC2 + PIP3} \tag{3.2.12}$$

$$\mathrm{mTORC2_i + J} \leftrightarrows \mathrm{C_{11}} \rightarrow \mathrm{mTORC2 + J} \tag{3.2.13}$$

where the subscript "i" denotes the inactive form and $\mathrm{C_{10}, C_{11}}$ the complexes in reactions (3.2.12)-(3.2.13), with the kinetic constants defined accordingly. Although the TSC1/2 complex has been shown to positively regulate mTORC2 kinase activity [11, 4], we did not include this pathway in the model in view of the results reported in [12]. Moreover, S6K1 negatively regulates mTORC2 by phosphorylation of Rictor (a component of mTORC2) at Thr1135, so impairing mTORC2 ability to phosphorylate Akt at Ser473 [108]. We have:

$$\mathrm{mTORC2 + S6K1} \leftrightarrows \mathrm{C_{12}} \rightarrow \mathrm{mTORC2^T + S6K1} \tag{3.2.14}$$

where $\mathrm{mTORC2^T}$ denotes the mTOR complex 2 with Rictor phosphorylated at Thr1135. The inverse transition is assumed to be regulated by a rate constant k_{-12}.

Akt phosphorylation/dephosphorylation

The first step in Akt activation is the protein translocation to plasma membrane through interaction with PIP3. For simplicity, we have not considered this step as well as the recruitment of PDK1 to PM, assuming that Akt translocation to PM and Thr308 Akt phosphorylation are a unique step directly regulated by PDK1. At the membrane, mTORC2 phosphorylates Akt at Ser473. The protein phosphatase PHLPP dephosphorylates Akt at Ser473 and the phosphatase PP2A dephosphorylates Akt at Thr308 (Fig 3.1). In some cases a hierarchical scheme where Ser473 Akt phosphorylation precedes phosphorylation at Thr308 was considered but this point is controversial [10]. So, we assumed that two pathways may in principle be followed to achieve full Akt phosphorylation and obtain the following reactions:

$$\begin{aligned}
\mathrm{Akt} + \mathrm{PDK1} &\leftrightarrows \mathrm{C}_{13} \rightarrow \mathrm{Akt}^{\mathrm{T}} + \mathrm{PDK1} && (3.2.15)\\
\mathrm{Akt}^{\mathrm{T}} + \mathrm{PP2A} &\leftrightarrows \mathrm{C}_{14} \rightarrow \mathrm{Akt} + \mathrm{PP2A} && (3.2.16)\\
\mathrm{Akt} + \mathrm{mTORC2} &\leftrightarrows \mathrm{C}_{15} \rightarrow \mathrm{Akt}^{\mathrm{S}} + \mathrm{mTORC2} && (3.2.17)\\
\mathrm{Akt}^{\mathrm{S}} + \mathrm{PHLPP} &\leftrightarrows \mathrm{C}_{16} \rightarrow \mathrm{Akt} + \mathrm{PHLPP} && (3.2.18)\\
\mathrm{Akt}^{\mathrm{S}} + \mathrm{PDK1} &\leftrightarrows \mathrm{C}_{17} \rightarrow \mathrm{Akt}^{\mathrm{S,T}} + \mathrm{PDK1} && (3.2.19)\\
\mathrm{Akt}^{\mathrm{S,T}} + \mathrm{PP2A} &\leftrightarrows \mathrm{C}_{18} \rightarrow \mathrm{Akt}^{\mathrm{S}} + \mathrm{PP2A} && (3.2.20)\\
\mathrm{Akt}^{\mathrm{T}} + \mathrm{mTORC2} &\leftrightarrows \mathrm{C}_{19} \rightarrow \mathrm{Akt}^{\mathrm{T,S}} + \mathrm{mTORC2} && (3.2.21)\\
\mathrm{Akt}^{\mathrm{T,S}} + \mathrm{PHLPP} &\leftrightarrows \mathrm{C}_{20} \rightarrow \mathrm{Akt}^{\mathrm{T}} + \mathrm{PHLPP} && (3.2.22)
\end{aligned}$$

where $\mathrm{Akt}^{\mathrm{T}}$ denotes Akt phosphorylated at Thr308, $\mathrm{Akt}^{\mathrm{S}}$ denotes Akt phosphorylated at Ser473, and $\mathrm{Akt}^{\mathrm{S,T}}$ or $\mathrm{Akt}^{\mathrm{T,S}}$ denote the dual phosphorylated protein. C_{13}-C_{20} denote the complexes in reactions (3.2.15)-(3.2.22).

Activation/deactivation of the Akt substrates FoxO1 and GSK3β

Upon phosphorylation by $\mathrm{Akt}^{\mathrm{S}}$ and $\mathrm{Akt}^{\mathrm{S,T}}$, FoxO1 leaves the nucleus and enters cytoplasm, where it is degraded. We have

$$\mathrm{FoxO1}_{\mathrm{nucl}} + \mathrm{Akt}^{\mathrm{S}} \leftrightarrows \mathrm{C}_{21} \rightarrow \mathrm{Akt}^{\mathrm{S}} + \mathrm{FoxO1}_{\mathrm{cyt}} \qquad (3.2.23)$$

and similarly for $\mathrm{Akt}^{\mathrm{S,T}}$ with the same kinetic constants. The inverse transition are also regulated by equal rate constants. We assume that $\mathrm{GSK3}\beta$ is phosphorylated at Ser9 and deactivated by pAkt, but it may also be sequestered in cytoplasmic vesicles [49]. We have

$$\mathrm{GSK3}\beta + \mathrm{pAkt} \leftrightarrows \mathrm{C}_{23} \rightarrow \mathrm{pAkt} + \mathrm{GSK3}\beta_{\mathrm{i}} \qquad (3.2.24)$$

Binding with the factor W that promotes sequestration and $\mathrm{GSK3}\beta$ sequestration/recruitment are similarly represented.

Activation/deactivation of the pathway to mTORC1 *and* S6K1

$\mathrm{Akt}^{\mathrm{T}}$ and $\mathrm{Akt}^{\mathrm{T,S}}$ phosphorylate and inactivate the tuberous sclerosis complex 2 (TSC2). TSC2 inactivation inhibits the formation of the complex Rheb/GDP and thus enhances the active complex Rheb/GTP, which in turn activates the mTOR complex 1 [5]. To simplify the model, we consider that mTORC1 is activated directly by $\mathrm{Akt^T}$ and $\mathrm{Akt^{T,S}}$:

$$\mathrm{Akt^T + mTORC1_i \leftrightarrows C_{24} \rightarrow Akt^T + mTORC1} \tag{3.2.25}$$

and similarly for $\mathrm{Akt^{T,S}}$ with the same kinetic constants. The inverse transition is regulated by a rate constant. For the full activation of S6K1, we neglect Ser371 phosphorylation by GSK3β [53] and we assume that phosphorylation at Thr229 by PDK1 precedes the Thr389 phosphorylation by mTORC1 [54].

$$\mathrm{S6K1_i + PDK1} \quad \leftrightarrows \quad \mathrm{C_{25} \rightarrow S6K1^{'} + PDK1} \tag{3.2.26}$$
$$\mathrm{S6K1^{'} + mTORC1} \quad \leftrightarrows \quad \mathrm{C_{26} \rightarrow S6K1 + mTORC1} \tag{3.2.27}$$

where $\mathrm{S6K1_i}$ denotes the inactive form, $\mathrm{S6K1^{'}}$ the Thr229-phosphorylated form, and S6K1 the active form phosphorylated at both Thr229 and Thr389. The inverse transitions, $\mathrm{S6K1^{'} \rightarrow S6K1_i}$ and $\mathrm{S6K1 \rightarrow S6K1^{'}}$, are regulated rate constants. As seen in reaction (3.2.6), the fully activated S6K1 promotes the serine phosphorylation of IRS1.

Exocytosis/endocytosis of GLUT4

$\mathrm{Akt^T}$ and fully activated Akt phosphorylate and inactivate AS160, thus relieving from the inactive state some Rab proteins implicated in vesicular traffic processes [3, 121, 8]. According to Sedaghat et al. [17], we assume that GLUT4 also undergoes trafficking between cytoplasm and plasma membrane in basal conditions. Insulin stimulation promotes GLUT4 exocytosis according to the following reaction:

$$\mathrm{AS160 + Akt^T \leftrightarrows C_{28} \rightarrow Akt^T + AS160_i} \tag{3.2.28}$$
$$\mathrm{AS160 + Rab \leftrightarrows C_{29} \rightarrow AS160 + Rab_i} \tag{3.2.29}$$
$$\mathrm{GLUT4_{cyt} + Rab \leftrightarrows C_{30} \rightarrow Rab + GLUT4_{pm}} \tag{3.2.30}$$

and similarly as (3.2.28) for $\mathrm{Akt^{T,S}}$. The inverse reactions are regulated by rate constants, and the subscript "i" denotes the inactive form. The rate constants of exocytosis and endocytosis are denoted as k_{exo} and, respectively, k_{endo}. We remark that AS160 is here inhibited by pAkt(Thr308) and fully activated Akt whereas in the model proposed in [19] AS160 is inhibited by pAkt(Ser473) and fully activated Akt. Our assumption is supported by the results reported in [122], where muscle-specific deletion of rictor in mice reduced pAkt(Ser473) to less than 10% of control, but pAS160(Thr642) was still at 80% of control, with data from glucose and insulin tolerance tests not substantially different from control.

3.2.2 Kinetic and equilibrium equations

The concentrations at the equilibrium of the chemicals are obtained from the kinetic equations by setting the time derivatives to zero. Synthesis and degradation rates are denoted by the symbols b and, respectively, μ (with the suitable subscripts).

We show now in detail the derivation of the kinetic equations for reactions (3.2.1)-(3.2.8), denoting the concentration with the same symbol of the chemical species written in italic. A similar procedure allows obtaining the concentrations at equilibrium of all other species.

For the complexes C_0-C_6 and C_P the following equations hold:

$$\frac{dC_0}{dt} = k_{0a} IR \cdot I - (k_{0d} + k_{0c}) C_0 \,, \tag{3.2.31}$$

$$\frac{dC_1}{dt} = k_{1a} IR^Y \cdot PTP1B - (k_{1d} + k_{1c}) C_1 \,, \tag{3.2.32}$$

$$\frac{dC_2}{dt} = k_{2a} IR^Y \cdot IRS1 - (k_{2d} + k_{2c}) C_2 \,, \tag{3.2.33}$$

$$\frac{dC_3}{dt} = k_{3a} IRS1^Y \cdot PTP1B - (k_{3d} + k_{3c}) C_3 \,, \tag{3.2.34}$$

$$\frac{dC_4}{dt} = k_{4a} IRS1 \cdot S6K1 - (k_{4d} + k_{4c}) C_4 \,, \tag{3.2.35}$$

$$\frac{dC_5}{dt} = k_{5a} IRS1^S \cdot PP - (k_{5d} + k_{5c}) C_5 \,, \tag{3.2.36}$$

$$\frac{dC_6^{'}}{dt} = k_{6a}^{'} IRS1^Y \cdot p110_{cyt} - (k_{6d}^{'} + k_{6c}^{'}) C_6^{'} \,, \tag{3.2.37}$$

$$\frac{dC_6}{dt} = k_{6a} IRS1^Y \cdot p110_{PM} - (k_{6d} + k_{6c}) C_6 \,, \tag{3.2.38}$$

$$\frac{dC_P}{dt} = k_{Pa} PTP1B \cdot pAkt - (k_{Pd} + k_{Pc}) C_P \,, \tag{3.2.39}$$

where we have assumed that the degradation rate constant of a complex is negligible compared with the sum of the dissociation and catalytic constants according to the observations in [114]. An equation similar to (3.2.32) with

IR_b^Y instead of IR^Y holds for $C_1^{'}$. Moreover, in (3.2.37)-(3.2.38), $IRS1^Y$ denotes the concentration of the complex IRS1$^{\mathrm{Y}}$/p85.

Recalling that the Michaelis-Menten constant is defined as $K_m = (k_d + k_c)/k_a$ and the specificity constant as k_c/K_m, at the equilibrium (time derivatives equal to zero), we write

$$C_0 = \frac{IR \cdot I}{K_{m,0}}, \qquad C_1 = \frac{IR^Y \cdot PTP1B}{K_{m,1}}, \tag{3.2.40}$$

$$C_2 = \frac{IRS1 \cdot IR^Y}{K_{m,2}}, \qquad C_3 = \frac{IRS1^Y \cdot PTP1B}{K_{m,3}}, \tag{3.2.41}$$

$$C_4 = \frac{IRS1 \cdot S6K1}{K_{m,4}}, \qquad C_5 = \frac{IRS1^S \cdot PP}{K_{m,5}}. \tag{3.2.42}$$

Similarly, for the complexes $\mathrm{C_P}$, $\mathrm{C_6^{'}}$ and $\mathrm{C_6}$ we have

$$C_P = \frac{PTP1B \cdot pAkt}{K_{m,P}}, \qquad C_6^{'} = \frac{IRS1^Y \cdot p110_{cyt}}{K_{m,6}^{'}}, \tag{3.2.43}$$

$$C_6 = \frac{IRS1^Y \cdot p110_{pm}}{K_{m,6}}.$$

The kinetics of IR, IR^Y and of the spontaneously autophosphorylated IR, denoted as IR_b^Y, is described by

$$\frac{dIR}{dt} = -k_{0a} IR \cdot I + k_{0d} C_0 + k_{1c} C_1 + k_{1c} C_1^{'} + b_{IR} - \mu_{IR} IR - k_b IR, \tag{3.2.44}$$

$$\begin{aligned}\frac{dIR^Y}{dt} =& k_{0c} C_0 - k_{1a} IR^Y \cdot PTP1B + k_{1d} C_1 - k_{2a} IR^Y \cdot IRS1 \\ &+ (k_{2d} + k_{2c}) C_2 - \mu_{IR} IR^Y,\end{aligned} \tag{3.2.45}$$

$$\frac{dIR_b^Y}{dt} = k_b IR - k_{1a} IR_b^Y \cdot PTP1B + k_{1d} C_1^{'} - \mu_{IR} IR_b^Y, \tag{3.2.46}$$

where b_{IR}, expressed as concentration over time, is the rate of biosynthesis (and transport to PM) of the insulin receptor, μ_{IR} is a rate constant representing internalization and degradation, and k_b is the rate constant of spontaneous IR autophosphorylation.

For IRS1 and PTP1B, we write:

$$\begin{aligned}
\frac{dIRS1}{dt} =& - k_{2a}IRS1 \cdot IR^{Y} + k_{2d}C_2 + k_{3c}C_3 - k_{4a}IRS1 \cdot S6K1 \\
&+ k_{4d}C_4 + k_{5c}C_5 + b_{IRS1} - \mu_{IRS1}IRS1 \,, \qquad (3.2.47) \\
\frac{dIRS1^{Y}}{dt} =& k_{2c}C_2 - k_{3a}IRS1^{Y} \cdot PTP1B + k_{3d}C_3 - k^{'}_{6a}IRS1^{Y} \cdot p110_{cyt} \\
&+ (k^{'}_{6d} + k^{'}_{6c})C^{'}_{6} - k_{6a}IRS1^{Y} \cdot p110_{PM} \\
&+ (k_{6d} + k_{6c})C_6 - \mu_{IRS1}IRS1^{Y} \,, \qquad (3.2.48) \\
\frac{dIRS1^{S}}{dt} =& k_{4c}C_4 - k_{5a}IRS1^{S} \cdot PP + k_{5d}C_5 - \mu_{IRS1}IRS1^{S} \,, \qquad (3.2.49) \\
\frac{dPTP1B}{dt} =& - k_{1a}IR^{Y} \cdot PTP1B + (k_{1d} + k_{1c})C_1 - k_{3a}IRS1^{Y} \cdot PTP1B \\
&+ (k_{3d} + k_{3c})C_3 - k_{Pa}PTP1B \cdot pAkt + k_{Pd}C_P \\
&+ k_{-P}PTP1B_i + b_{PTP1B} - \mu_{PTP1B}PTP1B \,, \qquad (3.2.50) \\
\frac{dPTP1B_i}{dt} =& k_{Pc}C_P - k_{-P}PTP1B_i - \mu_{PTP1B}PTP1B_i \,. \qquad (3.2.51)
\end{aligned}$$

In view of (3.2.31)-(3.2.33), Eqs. (3.2.44)-(3.2.46) at the equilibrium give

$$\begin{aligned}
-k_{0c}C_0 + k_{1c}C_1 + b_{IR} - \mu_{IR}IR - k_bIR + k_{1C}C^{'}_{1} &= 0 \,, \qquad (3.2.52) \\
+k_{0c}C_0 - k_{1c}C_1 - \mu_{IR}IR^{Y} &= 0 \,, \qquad (3.2.53) \\
+k_bIR - k_{1C}C^{'}_{1} - \mu_{IR}IR^{Y}_{b} &= 0 \,, \qquad (3.2.54)
\end{aligned}$$

where C_2 does not appear because its degradation rate constant has been taken equal to zero. The sum of (3.2.52)- (3.2.54) provides the relation

$$IR + IR^{Y} + IR^{Y}_{b} = \frac{b_{IR}}{\mu_{IR}} \,. \qquad (3.2.55)$$

The above equation and (3.2.53)-(3.2.54) are a linear system in IR, IR^{Y} and IR^{Y}_{b}, which is easily solved providing

$$IR^{Y} = \frac{b_{IR}}{\mu_{IR}} \frac{\dfrac{k_{0c}}{K_{m,0}}I}{k_b + \mu_{IR} + \dfrac{k_{1c}PTP1B}{K_{m,1}} + \dfrac{k_{0c}}{K_{m,0}}I} \,, \qquad (3.2.56)$$

$$IR^{Y}_{b} = \frac{b_{IR}}{\mu_{IR}} \frac{k_b}{k_b + \mu_{IR} + \dfrac{k_{1c}PTP1B}{K_{m,1}} + \dfrac{k_{0c}}{K_{m,0}}I} \,. \qquad (3.2.57)$$

The expression of IR is similarly found. We impose for the insulin the conservation equation

$$I_e = I + C_0 + IR^Y \,, \tag{3.2.58}$$

where I_e is total insulin concentration, the insulin in the complex $\mathrm{IR}^{\mathrm{Y}}:\mathrm{IRS1}$ was neglected and terms in the right-hand-side refer to equal volumes. Using the expressions of IR and IR^Y, the conservation equation yields a second-order equation that gives I as a function of I_e:

$$\begin{aligned} I =& \frac{1}{2}\Big[- (a_b + a_0^{''} + a_1^{''} PTP1B - I_e) + \\ & \sqrt{(a_b + a_0^{''} + a_1^{''} PTP1B - I_e)^2 + 4(a_b + a_0^{'} + a_1^{'} PTP1B) I_e}\Big] \,, \end{aligned} \tag{3.2.59}$$

with the following unknown parameters:

$$a_b = k_b \Big/ \left(\frac{k_{0c}}{K_{m,0}}\right) , \quad a_0^{'} = \mu_{IR} \Big/ \left(\frac{k_{0c}}{K_{m,0}}\right) , \quad a_1^{'} = \left(\frac{k_{1c}}{K_{m,1}}\right) \Big/ \left(\frac{k_{0c}}{K_{m,0}}\right)$$

$$a_0^{''} = a_0^{'} + \frac{b_{IR}}{\mu_{IR}} \frac{a_0^{'}}{K_{m,0}} + \frac{b_{IR}}{\mu_{IR}} , \quad a_1^{''} = a_1^{'} + \frac{b_{IR}}{\mu_{IR}} \frac{a_1^{'}}{K_{m,0}} ,$$

where the choice of the positive sign in the square root is required to have $I \geq 0$. Equation (3.2.59) allows us to express IR^Y and IR_b^Y as functions of I_e. If $I_e = 0$ and $k_b > 0$, only IR_b^Y survives and its expression shows that k_b is likely to be much smaller than $k_{1c}PTP1B/K_{m,1}$. Note that the unit of a_b and a_0 is a concentration and a_1 is nondimensional.

Proceeding similarly, Eqs. (3.2.47)-(3.2.49) at the equilibrium give

$$-k_{2c}C_2 + k_{3c}C_3 - k_{4c}C_4 + k_{5c}C_5 + b_{IRS1} - \mu_{IRS1} IRS1 = 0 \,, \tag{3.2.60}$$

$$k_{2c}C_2 - k_{3c}C_3 - \mu_{IRS1} IRS1^Y = 0 \,, \tag{3.2.61}$$

$$k_{4c}C_4 - k_{5c}C_5 - \mu_{IRS1} IRS1^S = 0 \,, \tag{3.2.62}$$

and the sum of (3.2.60)-(3.2.62) provides the relation

$$IRS1 + IRS1^Y + IRS1^S = \frac{b_{IRS1}}{\mu_{IRS1}} \,. \tag{3.2.63}$$

Using the expressions of the complexes in Eqs. (3.2.61), (3.2.62) we obtain

$$k_{2c}\frac{IR^Y \cdot IRS1}{K_{m,2}} - \left(k_{3c}\frac{PTP1B}{K_{m,3}} + \mu_{IRS1}\right) IRS1^Y = 0\,, \tag{3.2.64}$$

$$k_{4c}\frac{S6K1 \cdot IRS1}{K_{m,4}} - \left(k_{5c}\frac{PP}{K_{m,5}} + \mu_{IRS1}\right) IRS1^S = 0\,. \tag{3.2.65}$$

Given $IR^Y, PTP1B, S6K1$ and PP, Eqs. (3.2.63)-(3.2.65) are a linear system in $IRS1$, $IRS1^Y$ and $IRS1^S$ whose solution in $IRS1^Y$ and $IRS1^S$ is given by:

$$IRS1^Y = \frac{b_{IRS1}}{\mu_{IRS1}} \frac{\alpha\dfrac{k_{2c}}{K_{m,2}}IR^Y}{\alpha\beta + \beta\dfrac{k_{4c}}{K_{m,4}}S6K1 + \alpha\dfrac{k_{2c}}{K_{m,2}}IR^Y} \tag{3.2.66}$$

$$IRS1^S = \frac{b_{IRS1}}{\mu_{IRS1}} \frac{\beta\dfrac{k_{4c}}{K_{m,4}}S6K1}{\alpha\beta + \beta\dfrac{k_{4c}}{K_{m,4}}S6K1 + \alpha\dfrac{k_{2c}}{K_{m,2}}IR^Y} \tag{3.2.67}$$

with

$$\alpha = \mu_{IRS1} + \frac{k_{5c}}{K_{m,5}}PP\,, \qquad \beta = \mu_{IRS1} + \frac{k_{3c}}{K_{m,3}}PTP1B\,.$$

Moreover, at the equilibrium, from Eqs. (3.2.50) and (3.2.51) we have

$$PTP1B_i + PTP1B = \frac{b_{PTP1B}}{\mu_{PTP1B}} \tag{3.2.68}$$

and, using (3.2.68) and the expression of C_p with $pAkt = Akt^{S,T}$ (that is, the fully active, but not the partially active Akt phosphorylates PTP1B), we get

$$PTP1B = \frac{b_{PTP1B}}{\mu_{PTP1B}} \frac{1}{1 + \dfrac{1}{\mu_{PTP1B} + k_{-9}} \cdot \dfrac{k_{Pc}}{K_{m,P}}Akt^{S,T}}\,. \tag{3.2.69}$$

From Eq. (3.2.56) it is found, as expected, that IR^Y increases with the insulin concentration I_e and (3.2.66) shows that $IRS1^Y$ increases with IR^Y and thus with I_e, provided that $PTP1B$, PP and $S6K1$ are constant. However, according to (3.2.66), the downstream kinase S6K1 exerts an inhibitory effect on the IRS1 tyrosine phosphorylation and thus on insulin signalling (negative feedback). In addition, the fully phosphorylated Akt inhibits the phosphatase PTP1B as shown by (3.2.69), and thus tends to increase IR^Y (see Eq. (3.2.56)) and to decrease the factor β in (3.2.66)-(3.2.67). Consequently, Akt phosphorylation might exert a positive feedback on insulin signaling, especially upon inhibition of $S6K1$. In the absence of the positive feedback, PTP1B is constant and simpler expressions hold for the phosphorylated IR and IRS1.

Following the same approach, and without reporting from now on the kinetic equations, it is found that

$$PI3K = \frac{b_{p110}}{\mu_{p110}} \frac{\frac{k'_{6c}}{K'_{m,6}} \frac{k_{6c}}{K_{m,6}} (IRS1^Y)^2}{E + F \cdot IRS1^Y + \frac{k'_{6c}}{K'_{m,6}} \frac{k_{6c}}{K_{m,6}} (IRS1^Y)^2}, \tag{3.2.70}$$

where

$$E = (\mu_{p110} + k'_{-6})(\mu_{p110} + k_{-6}), \qquad F = \mu_{p110} \left(\frac{k'_{6c}}{K'_{m,6}} + \frac{k_{6c}}{K_{m,6}} \right) + \frac{k'_{6c}}{K'_{m,6}} k_{-6}.$$

According to reactions (3.2.9)-(3.2.11), we get

$$PI(4,5)P_2 + PIP_3 = \frac{b_{PI}}{\mu_{PI}}, \tag{3.2.71}$$

$$PDK1_i + PDK1 = \frac{b_{PDK1}}{\mu_{PDK1}}, \tag{3.2.72}$$

and

$$PIP_3 = \frac{b_{PI}}{\mu_{PI}} \frac{\frac{k_{7c}}{K_{m,7}} PI3K}{\mu_{PI} + \frac{k_{8c}}{K_{m,8}} PTEN + \frac{k_{7c}}{K_{m,7}} PI3K}, \tag{3.2.73}$$

$$PDK1 = \frac{b_{PDK1}}{\mu_{PDK1}} \frac{\frac{k_{9c}}{K_{m,9}} PIP_3}{\mu_{PDK1} + k_{-9} + \frac{k_{9c}}{K_{m,9}} PIP_3}. \tag{3.2.74}$$

Equation (3.2.73) predicts that the concentration of the second messenger PIP3 increases with PI3K if PTEN is constant and still increases after PTEN deletion. Note that the spontaneous IR autophosphorylation leads to nonzero PIP3 and PDK1 concentrations for $I_e = 0$.

Turning to the mTOR complex 2, we find:

$$mTORC2 = \frac{b_{mTORC2}}{\mu_{mTORC2}} \frac{\left(\mu_{mTORC2} + k_{-12}\right)\left(\frac{k_{10c}}{K_{m,10}} PIP_3 + \frac{k_{11c}}{K_{m,11}} J\right)}{D}\,, \tag{3.2.75}$$

where

$$\begin{aligned} D =& \left(\mu_{mTORC2} + k_{-12}\right)\left(\mu_{mTORC2} + k_{-10} + k_{-11}\frac{k_{10c}}{K_{m,10}} PIP_3 + \frac{k_{11c}}{K_{m,11}} J\right) \\ &+ \frac{k_{12c}}{K_{m,12}} S6K1 \left(\mu_{mTORC2}\frac{k_{10c}}{K_{m,10}} PIP_3 + \frac{k_{11c}}{K_{m,11}} J\right)\,, \end{aligned} \tag{3.2.76}$$

showing how mTORC1 negatively regulates mTORC2 via S6K1.

The concentrations of Akt, $\mathrm{Akt}^{\mathrm{T}}$, $\mathrm{Akt}^{\mathrm{S}}$ and $\mathrm{Akt}^{\mathrm{S,T}}$ at the steady state are derived from reactions (3.2.15)-(3.2.22) by solving a system of four linear equations, one of them given by

$$Akt + Akt^{T} + Akt^{S} + Akt^{S,T} = \frac{b_{Akt}}{\mu_{Akt}}\,. \tag{3.2.77}$$

We obtain the following expressions:

$$\begin{aligned} Akt^{T} =& \frac{b_{Akt}}{\mu_{Akt}} \frac{PDK1}{D_1} \left(\frac{k_{13c}}{K_{m,13}} \frac{k_{17c}}{K_{m,17}} PDK1 \theta + \right. \\ & \left. \frac{k_{15c}}{K_{m,15}} \frac{k_{17c}}{K_{m,17}} mTORC2 \left(\gamma - \eta\right) + \frac{k_{13c}}{K_{m,13}} \gamma\epsilon\right)\,, \end{aligned} \tag{3.2.78}$$

$$\begin{aligned} Akt^{S} =& \frac{b_{Akt}}{\mu_{Akt}} \frac{mTORC2}{D_1} \left(\frac{k_{15c}}{K_{m,15}} \frac{k_{19c}}{K_{m,19}} mTORC2 \eta + \right. \\ & \left. + \frac{k_{13c}}{K_{m,13}} \frac{k_{19c}}{K_{m,19}} PDK1 \left(\gamma - \theta\right) + \frac{k_{15c}}{K_{m,15}} \gamma\delta\right)\,, \end{aligned} \tag{3.2.79}$$

$$\begin{aligned} Akt^{T,S} =& \frac{b_{Akt}}{\mu_{Akt}} \frac{PDK1 \cdot mTORC2}{D_1} \left(\frac{k_{15c}}{K_{m,15}} \frac{k_{17c}}{K_{m,17}} \left(\frac{k_{19c}}{K_{m,19}} mTORC2 + \delta\right) + \right. \\ & \left. \frac{k_{13c}}{K_{m,13}} \frac{k_{19c}}{K_{m,19}} \left(\frac{k_{17c}}{K_{m,17}} PDK1 + \epsilon\right)\right) \end{aligned} \tag{3.2.80}$$

where the the denominator D_1 is given by

$$\begin{aligned} D_1 = \frac{k_{13c}}{K_{m,13}}\frac{k_{17c}}{K_{m,17}} PDK1^2 \left(\frac{k_{19c}}{K_{m,19}} mTORC2 + \theta\right) + \\ \frac{k_{15c}}{K_{m,15}}\frac{k_{19c}}{K_{m,19}} mTORC2^2 \left(\frac{k_{17c}}{K_{m,17}} PDK1 + \eta\right) + \\ PDK1 \cdot mTORC2 \left(\frac{k_{15c}}{K_{m,15}}\frac{k_{17c}}{K_{m,17}} (\gamma + \delta - \eta) + \right. \\ \left. \frac{k_{13c}}{K_{m,13}}\frac{k_{19c}}{K_{m,19}} (\gamma + \epsilon - \theta) + \frac{k_{17c}}{K_{m,17}}\frac{k_{19c}}{K_{m,19}} (\eta + \theta - \gamma)\right) + \\ PDK1 \left(\frac{k_{13c}}{K_{m,13}} \gamma\epsilon + \frac{k_{17c}}{K_{m,17}} \delta\theta\right) + mTORC2 \left(\frac{k_{15c}}{K_{m,15}} \gamma\delta + \frac{k_{19c}}{K_{m,19}} \epsilon\eta\right) + \gamma\delta\epsilon \quad (3.2.81) \end{aligned}$$

and the quantities $\gamma, \delta, \epsilon, \eta, \theta$ express the activity of the phosphatases:

$$\gamma = \mu_{Akt} + \frac{k_{18c}}{K_{m,18}} PP2A + \frac{k_{20c}}{K_{m,20}} PHLPP\,, \quad (3.2.82)$$

$$\delta = \mu_{Akt} + \frac{k_{14c}}{K_{m,14}} PP2A\,, \quad (3.2.83)$$

$$\epsilon = \mu_{Akt} + \frac{k_{16c}}{K_{m,16}} PHLPP\,, \quad (3.2.84)$$

$$\eta = \mu_{Akt} + \frac{k_{18c}}{K_{m,18}} PP2A\,, \quad (3.2.85)$$

$$\theta = \mu_{Akt} + \frac{k_{20c}}{K_{m,20}} PHLPP\,. \quad (3.2.86)$$

Equations (3.2.78)-(3.2.80) show that in the absence of insulin, when the concentrations of PDK1, $\mathrm{Akt^{T}}$ and $\mathrm{Akt^{S,T}}$ are likely to be very small, the concentration of $\mathrm{Akt^{S}}$ may still be large because of mTORC2 signaling throught the factor J (Eq. (3.2.75)). This behavior cannot be described by a hierarchical scheme in which Thr308Akt phosphorylation is necessary for phosphorylation at Ser473. The phosphorylation at threonine and serine measured in the absence of insulin may be related to: 1) basal autophosphorylation of the insulin receptor [101]; 2) signaling from other receptors (e.g., $\mathrm{IGF}-1$ receptor); 3) PIP3 activation by $\mathrm{PI(3,4)P2}$; 4) nonspecific binding of the anti pAkt antibodies.

The cytoplasmic FoxO1 concentration is given by

$$FoxO1_{cyt} = \frac{b_{FoxO}}{\mu_{FoxO}} \frac{\frac{k_{21c}}{K_{m,21}} \left(Akt^S + Akt^{T,S}\right)}{\mu_{deg} + k_{-21} + \frac{k_{21c}}{K_{m,21}} \left(Akt^S + Akt^{T,S}\right)} . \tag{3.2.87}$$

The concentration of phosphorylated GSK3β is obtained as

$$GSK3\beta_{cyt} = \frac{b_{GSK3}}{\mu_{GSK3}} \cdot \frac{\frac{k_{23c}}{K_{m,23}} \left(\frac{1}{\mu_{GSK3} + k_{-23}}\right) \left(Akt^T + Akt^{T,S}\right)}{1 + \frac{k_{24c}}{K_{m,24}} \left(\frac{1}{\mu_{GSK3} + k_{-24}}\right) W + \frac{k_{23c}}{K_{m,23}} \left(\frac{1}{\mu_{GSK3} + k_{-23}}\right) \left(Akt^T + Akt^{T,S}\right)} , \tag{3.2.88}$$

where W is the concentration of the putative factor that promotes GSK3β sequestration and decreased response [49].

For the cascade of reactions (3.2.25)- (3.2.27) leading to the activation of mTORC1 and S6K1, the following expressions for the concentrations of the active mTORC1 and S6K1 may be obtained:

$$mTORC1 = \frac{b_{TORC1}}{\mu_{TORC1}} \frac{\frac{k_{24c}}{K_{m,24}} \left(Akt^T + Akt^{T,S}\right)}{\mu_{mTORC1} + k_{-24} + \frac{k_{24c}}{K_{m,24}} \left(Akt^T + Akt^{T,S}\right)} , \tag{3.2.89}$$

$$S6K1 = \frac{b_{S6K1}}{\mu_{S6K1}} \frac{\frac{k_{26c}}{K_{m,26}} PDK1 \frac{k_{27c}}{K_{m,27}} mTORC1}{D_2} , \tag{3.2.90}$$

where

$$\begin{aligned} D_2 = & \left(\mu_{S6K1} + k_{-26}\right) \left(\mu_{S6K1} + k_{-27}\right) + \mu_{S6K1} \frac{k_{27c}}{K_{m,27}} mTORC1 \\ & + \frac{k_{26c}}{K_{m,26}} PDK1 \left(\mu_{S6K1} + k_{-27} \frac{k_{27c}}{K_{m,27}} mTORC1\right) \end{aligned} \tag{3.2.91}$$

Finally, for the concentration of GLUT4 at the plasma membrane, reactions (3.2.28)-(3.2.30) provide the following equation in terms of $Akt^T + Akt^{T,S}$:

$$GLUT4_{pm} = \frac{b_{GLUT}}{\mu_{GLUT}} \cdot$$

$$\frac{\omega\rho + [\omega\left(\mu_{Rab} + k_{-29}\right) + \sigma]}{\rho + [\mu_{Rab} + k_{-29} + \sigma]} \cdot \frac{1 + \dfrac{k_{28c}}{(\mu_{AS} + k_{-28})K_{m,28}}\left(Akt^T + Akt^{T,S}\right)}{1 + \dfrac{k_{28c}}{(\mu_{AS} + k_{-28})K_{m,28}}\left(Akt^T + Akt^{T,S}\right)} \tag{3.2.92}$$

where

$$\omega = \frac{k_{exo}}{\mu_{GLUT} + k_{exo} + k_{endo}}, \tag{3.2.93}$$

$$\rho = \frac{k_{29c}}{K_{m,29}} \frac{b_{AS}}{\mu_{AS}}, \tag{3.2.94}$$

$$\sigma = \frac{k_{-29}}{\mu_{GLUT} + k_{exo} + k_{endo}} \frac{k_{30c}}{K_{m,30}} \frac{b_{Rab}}{\mu_{Rab}}, \tag{3.2.95}$$

with ω possibly much smaller than 1. Equation (3.2.92) shows that a decrease in ω impairs GLUT4 translocation to plasma membrane. Moreover, at zero insulin, $GLUT4_{pm}$ may increase when AS160 expression is silenced (ρ driven close to zero), according to the function of "brake" of AS160 [8].

We note that most of model parameters, as seen in the previous equations, are in the form of the specificity constant k_c/K_m.

3.2.3 Model equations in normalized form

The model equations at the equilibrium, obtained in section 3.2.2, are here rewritten in a simple non-dimensional form in order to reduce the number of unknown parameters. The concentrations of all molecules, except insulin and factor J in (3.2.75), are normalized to the ratio of production rate (expressed as concentration · time^{-1}) over degradation rate constant (time^{-1}) and denoted by the subscript n. We recall that synthesis rate and degradation rate constants are assumed to not change with time and do not depend on the insulin signal. All the normalized concentrations are nonnegative and smaller than the unity for any value of the extracellular insulin concentration I_e. The model parameters are modified accordingly, and are combinations of the original parameters of the kinetic equations.

Let us start considering Eqs. (3.2.56)-(3.2.59), from which it is simple to obtain the equation for the total tyrosine phosphorylated IR in normalized form (i.e., normalized to b_{IR}/μ_{IR}). In particular, assuming for simplicity that the positive feedback is not active ($PTP1B_n = 1$), we have the following simplified expression:

$$IR_n^Y = \frac{IR^Y + IR_b^Y}{b_{IR}/\mu_{IR}} = \frac{a_b + I}{a_b + a_0 + I}\,, \tag{3.2.96}$$

where the free insulin concentration I is expressed as a function of total insulin I_e by

$$I = \frac{1}{2}\Big[- (a_b + a_0 + a_1 - I_e) + \sqrt{(a_b + a_0 + a_1 - I_e)^2 + 4(a_b + a_0)I_e}\,\Big]\,, \tag{3.2.97}$$

with

$$a_b = k_b \Big/ \left(\frac{k_{0c}}{K_{m,0}}\right)\,, \qquad a_0 = \left(\mu_{IR} + \frac{k_{1c}}{K_{m,1}}\frac{b_{PTP}}{\mu_{PTP}}\right) \Big/ \left(\frac{k_{0c}}{K_{m,0}}\right)\,,$$

$$a_1 = \frac{b_{IR}}{\mu_{IR}} \cdot \left(1 + \frac{a_0}{K_{m,0}}\right)\,.$$

Since $IR_b^Y = a_b/(a_b + a_0)$ can be experimentally measured, a_b can be written as $a_0\rho/(1-\rho)$, where ρ denotes this experimental value. Therefore, (3.2.96)-(3.2.97) allow to obtain two meaningful quantities function of a_0, a_1 and ρ, i.e. the value of I_e at $IR_n^Y = 0.5$

$$I_{e,0.5} = \left(a_0 + \frac{a_1}{2}\right)\frac{1-2\rho}{1-\rho} \tag{3.2.98}$$

and the slope at $I_{e,0.5}$

$$S_{0.5} = \frac{1-\rho}{a_1 + 4a_0(1-\rho)}\,, \tag{3.2.99}$$

where $I_{e,0.5}$ has the dimension of a concentration and $S_{0.5}$ is a concentration^{-1}.

Assuming that PP, and so α, is constant, Eqs. (3.2.66) and (3.2.67) are rewritten with $IRS1^Y$ and $IRS1^S$ normalized to b_{IRS1}/μ_{IRS1} as follows:

$$IRS1_n^Y = \frac{IR_n^Y}{(a_2 + a_3 PTP1B_n)(1 + a_4 S6K1_n) + IR_n^Y}\,, \tag{3.2.100}$$

$$IRS1_n^S = \frac{(a_2 + a_3 PTP1B_n)a_4 mTORC1_n}{(a_2 + a_3 PTP1B_n)(1 + a_4 S6K1_n) + IR_n^Y}\,, \tag{3.2.101}$$

where

$$a_2 = \mu_{IRS1}\left(\frac{k_{2c}}{K_{m,2}} \cdot \frac{b_{IR}}{\mu_{IR}}\right)^{-1}, \qquad a_3 = \frac{k_{3c}}{K_{m,3}} \cdot \frac{b_{PTP1B}}{\mu_{PTP1B}} \left(\frac{k_{2c}}{K_{m,2}} \cdot \frac{b_{IR}}{\mu_{IR}}\right)^{-1},$$

$$a_4 = \frac{k_{4c}}{\alpha K_{m,4}} \cdot \frac{b_{S6K1}}{\mu_{S6K1}},$$

with a_2-a_4 nondimensional.

Equation (3.2.69) becomes

$$PTP1B_n = \frac{1}{1 + a_P Akt_n^{S,T}} \tag{3.2.102}$$

with a_P given by

$$a_P = \frac{k_{Pc}}{(\mu_{PTP1B} + k_{-P})\, K_{m,P}} \cdot \frac{b_{Akt}}{\mu_{Akt}}.$$

In the absence of the positive feedback, $a_P = 0$ and $PTP1B_n = 1$.

Proceeding similarly, Eq. (3.2.70) normalized to b_{PI3K}/μ_{PI3K} rewrites as

$$PI3K_n = \frac{a_6 (IRS1_n^Y)^2}{1 + a_6' IRS1_n^Y + a_6 (IRS1_n^Y)^2}, \tag{3.2.103}$$

with

$$a_6' = \frac{F}{E} \cdot \frac{b_{IRS1}}{\mu_{IRS1}}, \qquad a_6 = \frac{1}{E} \frac{k_{6c}'}{K_{m,6}'} \frac{k_{6c}}{K_{m,6}} \left(\frac{b_{IRS1}}{\mu_{IRS1}}\right)^2.$$

Equations (3.2.73) and (3.2.74) become

$$PIP3_n = \frac{PI3K_n}{a_7 + a_8 PTEN_n + PI3K_n} \tag{3.2.104}$$

$$PDK1_n = \frac{a_9 PIP3_n}{1 + a_9 PIP3_n} \tag{3.2.105}$$

with

$$a_7 = \mu_{PI} \Big/ \left(\frac{k_{7c}}{K_{m,7}} \cdot \frac{b_{PI3K}}{\mu_{PI3K}}\right), \qquad a_8 = \left(\frac{k_{8c}}{K_{m,8}} \cdot \frac{b_{PTEN}}{\mu_{PTEN}}\right) \Big/ \left(\frac{k_{7c}}{K_{m,7}} \cdot \frac{b_{PI3K}}{\mu_{PI3K}}\right),$$

$$a_9 = \frac{k_{9c}}{(\mu_{PDK1} + k_{-9}) K_{m,9}} \cdot \frac{b_{PIP3}}{\mu_{PIP3}}.$$

For the mTOR complex 2, (3.2.75) provides the following equation:

$$mTORC2_n = \frac{a_{10} PIP3_n + a_{11} J}{1 + (1 + a_{12} S6K1_n)(a_{10}^{\mu} + a_{10} PIP3_n + a_{11} J)} \tag{3.2.106}$$

with

$$a_{10} = \frac{k_{10c}}{(k_{-10}+k_{-11})K_{m,10}} \frac{b_{PIP3}}{\mu_{PIP3}}\,, \qquad a_{11} = \frac{k_{11c}}{(k_{-10}+k_{-11})K_{m,11}}\,,$$

$$a_{12} = \frac{k_{12c}}{(\mu_{mTORC2}+k_{-12})K_{m,12}} \frac{b_{S6K1}}{\mu_{S6K1}}\,, \qquad a_{10}^{\mu} = \frac{\mu_{mTORC2}}{k_{-10}+k_{-11}}\,,$$

where $a_{10}, a_{10}^{\mu}, a_{12}$ are nondimensional and a_{11} is the inverse of a concentration.

Assuming $PP2A$ and $PHLPP$ (and so $\gamma, \delta, \epsilon, \eta, \theta$ defined by (3.2.82)-(3.2.86)) constant, Eqs. (3.2.78)-(3.2.80) may be rewritten in terms of eight parameters as follows:

$$Akt_n^T = \frac{PDK1_n}{D_1^{'}}\Big(a_{13}^{\delta}a_{17}^{\gamma}a_{\theta\epsilon}PDK1_n + a_{15}^{\epsilon}(a_{17}^{\delta} - a_{17}^{\gamma}a_{\eta\delta})mTORC2_n + a_{13}^{\delta}\Big) \tag{3.2.107}$$

$$Akt_n^S = \frac{mTORC2_n}{D_1^{'}}\Big(a_{15}^{\epsilon}a_{19}^{\gamma}a_{\eta\delta}mTORC2_n + a_{13}^{\delta}(a_{19}^{\epsilon} - a_{19}^{\gamma}a_{\theta\epsilon})PDK1_n + a_{15}^{\epsilon}\Big) \tag{3.2.108}$$

$$\begin{aligned} Akt_n^{S,T} =& \frac{PDK1_n mTORC2_n}{D_1^{'}}\Big(a_{15}^{\epsilon}a_{17}^{\delta}a_{19}^{\gamma}mTORC2_n + a_{13}^{\delta}a_{19}^{\epsilon}a_{17}^{\gamma}PDK1_n + \\ & a_{15}^{\epsilon}a_{17}^{\gamma} + a_{13}^{\delta}a_{19}^{\gamma}\Big) \end{aligned} \tag{3.2.109}$$

with

$$\begin{aligned} D_1^{'} =& a_{13}^{\delta}a_{17}^{\gamma}PDK1_n^2(a_{19}^{\epsilon}mTORC2_n + a_{\theta\epsilon}) + a_{15}^{\epsilon}a_{19}^{\gamma}mTORC2_n^2(a_{17}^{\delta}PDK1_n + a_{\eta\delta}) \\ & + PDK1_n mTORC2_n(a_{13}^{\delta}(a_{19}^{\epsilon} - a_{19}^{\gamma}a_{\theta\epsilon}) + a_{15}^{\epsilon}(a_{17}^{\delta} - a_{17}^{\gamma}a_{\eta\delta}) + a_{17}^{\gamma}(a_{15}^{\epsilon} + a_{19}^{\epsilon}a_{\eta\delta}) \\ & + a_{19}^{\gamma}(a_{13}^{\delta} + a_{17}^{\delta}a_{\theta\epsilon}) - a_{17}^{\delta}a_{19}^{\epsilon}) + PDK1_n(a_{13}^{\delta} + a_{17}^{\gamma}a_{\theta\epsilon}) \\ & + mTORC2_n(a_{15}^{\epsilon} - a_{19}^{\gamma}a_{\theta\epsilon}) + 1 \end{aligned}$$

and

$$\begin{aligned}
a_{13}^{\delta} &= \frac{k_{13c}}{K_{m,13}} \cdot \frac{b_{PDK1}}{\mu_{PDK1}} \frac{1}{\delta}\,, & a_{15}^{\epsilon} &= \frac{k_{15c}}{K_{m,15}} \cdot \frac{b_{mTORC2}}{\mu_{mTORC2}} \frac{1}{\epsilon}\,,\\
a_{17}^{\delta} &= \frac{k_{17c}}{K_{m,17}} \cdot \frac{b_{PDK1}}{\mu_{PDK1}} \frac{1}{\delta}\,, & a_{19}^{\epsilon} &= \frac{k_{19c}}{K_{m,19}} \cdot \frac{b_{mTORC2}}{\mu_{mTORC2}} \frac{1}{\epsilon}\,,\\
a_{17}^{\gamma} &= \frac{k_{17c}}{K_{m,17}} \cdot \frac{b_{PDK1}}{\mu_{PDK1}} \frac{1}{\gamma}\,, & a_{19}^{\gamma} &= \frac{k_{19c}}{K_{m,19}} \cdot \frac{b_{mTORC2}}{\mu_{mTORC2}} \frac{1}{\gamma}\,,\\
a_{\theta\epsilon} &= \frac{\theta}{\epsilon}\,, & a_{\eta\delta} &= \frac{\eta}{\delta}\,,
\end{aligned}$$

where all parameteres are nondimensional.

Concerning the Akt substrates, we assumed that singly and doubly phosphorylated Akt molecules have the same catalytic activity. So, the normalized cytoplasmic FoxO1 concentration is given by

$$FoxO1_n = \frac{a_{21}\left(Akt_n^S + Akt_n^{T,S}\right)}{1 + a_{21}\left(Akt_n^S + Akt_n^{T,S}\right)}\,, \tag{3.2.110}$$

with

$$a_{21} = \frac{1}{\mu_{FoxO} + k_{-21}} \frac{k_{21c}}{K_{m,21}} \frac{b_{Akt}}{\mu_{Akt}}\,.$$

The normalized concentration of phosphorylated GSK3β is obtained as

$$GSK3\beta_n = \frac{a_{23}\left(Akt_n^T + Akt_n^{T,S}\right)}{1 + a_{23}^{'}W + a_{23}\left(Akt_n^T + Akt_n^{T,S}\right)}\,, \tag{3.2.111}$$

with

$$a_{23} = \frac{1}{\mu_{GSK3} + k_{-23}} \frac{k_{23c}}{K_{m,23}} \frac{b_{Akt}}{\mu_{Akt}}\,, \qquad a_{23}^{'} = \frac{1}{\mu_{GSK3} + k_{-23}^{'}} \frac{k_{23c}^{'}}{K_{m,23}^{'}}\,.$$

Equation (3.2.89) for the normalized concentration of mTORC1 becomes:

$$mTORC1_n = \frac{a_{24}\left(Akt_n^T + Akt_n^{T,S}\right)}{1 + a_{24}\left(Akt_n^T + Akt_n^{T,S}\right)}\,, \tag{3.2.112}$$

with

$$a_{24} = \frac{1}{\mu_{mTORC1} + k_{-24}} \frac{k_{24c}}{K_{m,24}} \frac{b_{Akt}}{\mu_{Akt}}\,.$$

For the normalized $S6K1$ from (3.2.90) we have:

$$S6K1_n = \frac{a_{26}PDK1_n a_{27} mTORC2_n}{1 + a_{26}PDK1_n + (a_{26}^{\mu} + a_{26}PDK1_n) a_{27} mTORC1_n} \tag{3.2.113}$$

where

$$a_{26} = \frac{1}{\mu_{S6K1} + k_{-26}} \frac{k_{26c}}{K_{m,26}} \frac{b_{PDK1}}{\mu_{PDK1}}\,, \quad a_{26}^{\mu} = \frac{\mu_{S6K1}}{\mu_{S6K1} + k_{-26}}\,,$$

$$a_{27} = \frac{1}{\mu_{S6K1} + k_{-27}} \frac{k_{27c}}{K_{m,27}} \frac{b_{mTORC1}}{\mu_{mTORC1}}\,.$$

The equation (3.2.92) for the normalized $GLUT4_{pm}$ (here simply denoted as $GLUT4_n$) may be written as:

$$GLUT4_n = \frac{a_{28} + a_{29}(Akt_n^T + Akt_n^{T,S})}{1 + a_{30}(Akt_n^T + Akt_n^{T,S})}\,, \tag{3.2.114}$$

with

$$a_{28} = \frac{\omega\rho + \omega\left(\mu_{Rab} + k_{-29}\right) + \sigma}{\rho + \mu_{Rab} + k_{-29} + \sigma}\,,$$

$$a_{29} = \frac{\omega\left(\mu_{Rab} + k_{-29}\right) + \sigma}{\left(\rho + \mu_{Rab} + k_{-29} + \sigma\right)\left(\mu_{AS} + k_{-28}\right)} \cdot \frac{k_{-28}}{K_{m,28}} \cdot \frac{b_{GLUT}}{\mu_{GLUT}}\,,$$

$$a_{30} = \frac{\mu_{Rab} + k_{-29} + \sigma}{\left(\rho + \mu_{Rab} + k_{-29} + \sigma\right)\left(\mu_{AS} + k_{-28}\right)} \cdot \frac{k_{-28}}{K_{m,28}} \cdot \frac{b_{GLUT}}{\mu_{GLUT}}\,.$$

Parameters a_{28}, a_{29}, a_{30} account in a simple way for the various steps that promote GLUT4 translocation to plasma membrane [8]. Moreover, it may be easily verified that $a_{28} < 1$ and $a_{29} < a_{30}$.

In summary, given the concentrations of insulin and of the factor J, plus the constant parameters defined above, Eqs. (3.2.96)-(3.2.114) provide the dose-response curve of each component in the scheme of Fig. 3.1 of the insulin signaling network.

Chapter 4

Model parameter estimation from experimental data of skeletal muscle cells

In general, the typical building cycle of the model representing a biological process starts from a goal definition and some a priori knowledge (i.e. preliminary data and initial hypotheses) that suggest the model structure. From the available data, parameter estimation is then performed and, finally the initial model must be validated with new experiments. If the validation reveals a number of model deficiencies, a new model structure and/or a new experimental design must be planned and the process is repeated iteratively until the validation step is considered satisfactory.

In the previous chapter, we presented a mathematical model of the ISN developed to investigate the mechanisms that regulates the glucose uptake into insulin-sensitive cells such as muscle cells, hepatocytes and cells of the adipose tissue.

Skeletal muscle is the main tissue involved in the insulin-induced stimulation of glucose uptake in rodents and humans. Reduction of glucose uptake in muscles in the state of insulin resistance is the principal factor that accounts for reduced systemic glucose utilization. For this reason, skeletal muscle cells have long been regarded as a critical organ/cellular system for the investigation of insulin resistance and the pathogenesis of type 2 diabetes.

As described in this chapter, the ISN model parameters were estimated by fitting the model equations at the steady state (3.2.96)-(3.2.114) to the experimental data of two different skeletal muscle cell lines of rodents (L6 myoblasts and C2C12 myotubes) through minimization of a least-squares index. A preliminary observation of the data obtained from the two different cell lines [13, 123] suggested that, although L6 and C2C12 are both skeletal muscle cells, their response to insulin stimuli can be significantly different as well as their parameter values. Moreover, the observation of the data suggested that there could exist some differences in the ISN model structure for the two cell lines as detailed in the following sections.

The present chapter presents the main results of this thesis project and shows the potential applications that the ISN model here proposed could have.

4.1 Experimental data used for the ISN parameter estimation

The ISN model parameters were estimated using (separately) the experimental data sets related to two different skeletal muscle cell lines: L6 myotubes with induced insulin resistance and C2C12 myoblasts with PTEN protein suppressed.

L6 myotubes are derived from rat skeletal muscle, and this cell line is one of the most frequently used cellular model systems to investigate the insulin-stimulated glucose transport. In these cells insulin induces significant glucose uptake and the extent of such uptake is related to the expression and function of the muscle-specific GLUT4 glucose transporters. In addition, the GLUT1 glucose transporter responsible for basal glucose uptake is also expressed. Thus, this cell line serves as an ideal model system to investigate both insulin-dependent and insulin-independent glucose transport.

We used the experimental data of L6 cell line to estimate the parameter values of the ISN model in this line with the aim of obtaining a useful tool to generate and test hypotheses, leading to a deeper understanding of the molecular mechanisms underlying insulin resistance. Then, to test the ability of our model to reproduce the effect of gene knockout, we estimated the ISN model parameters starting from the second data set that showed the effect of PTEN knockout in C2C12 myotubes of mouse [123].

Let us show now in detail the two data sets, available in the literature, used for the parameter estimation.

L6 myotubes data The L6 data set includes data reported in [13] and in [124]. In [13], the Authors aimed to investigate the possible molecular mechanism/s underlying the decrease of insulin resistance and remission of type 2 diabetes observed after the bariatric surgey. Indeed, several and recent studies ([109], [110], [14]) demonstrated that bariatric surgery, a procedure in which a portion of the stomach and of the small intestine are removed or bypassed, induces a remission of type 2 diabetes very soon after surgery and far too early to be attributed to weight loss. The mechanisms responsible for the improvement in glycemic control after bariatric surgery are still not well understood but, as bariatric operations reroute food through the upper small intestine, it has been hypothesised that gastrointestinal removal or bypass reduce the production of putative intestinal factor/s inducing insulin resistance. To test such hypothesis, Salinari et al. [13] collected experimental data on the effects of jejunal proteins, secreted by diabetic mice (db/db) or Swiss mice, on the glucose uptake *in vivo* in Swiss mice and *in vitro* in both Swiss mice soleus and L6 skeletal muscle cells.

To perform the parameter estimation, we considered the data of L6 cells collected in [13]. These data represent the phosphorylation levels of some of ISN components for several insulin values normalized with respect to the respective saturation levels. In particular: the normalized levels of pAkt(Ser473) and (Thr308) at zero insulin and at insulin concentrations of 0.1, 1, 10, and 100 nM; pGSK3β(Ser9) at zero and 100 nM insulin; the basal (zero insulin) pAkt(Ser473) and pS6K1(Thr389) in the presence of the inhibitors Rapamycin and PP242 (that targets both mTOR complexes) [125]. The data, reported in Fig. 4.1, were measured in the control medium, enriched by proteins secreted by the jejunal mucosa of non-diabetic mice, and in conditioned medium (CM) enriched by proteins secreted by the mucosa of diabetic mice (db/db CM).

The phosphorylation of ISN components was measured by Western blot analysis [1] and quantified by densitometry.

As extensively discuss in Chapter 2, one of the main problems in the estimation of the biological parameter values from experimental data is that the number of available data is not large enough compared to the number of parameters. Another problem is related to the substantial differences in the parameter values that may be found among different cell types.

Such problems also characterized our study. So, in order to increase the amount of data for the estimation of L6 parameters, we used in addition some

---

[1] Western Blotting is a technique used in biochemistry for analysis of individual proteins in a protein mixture.

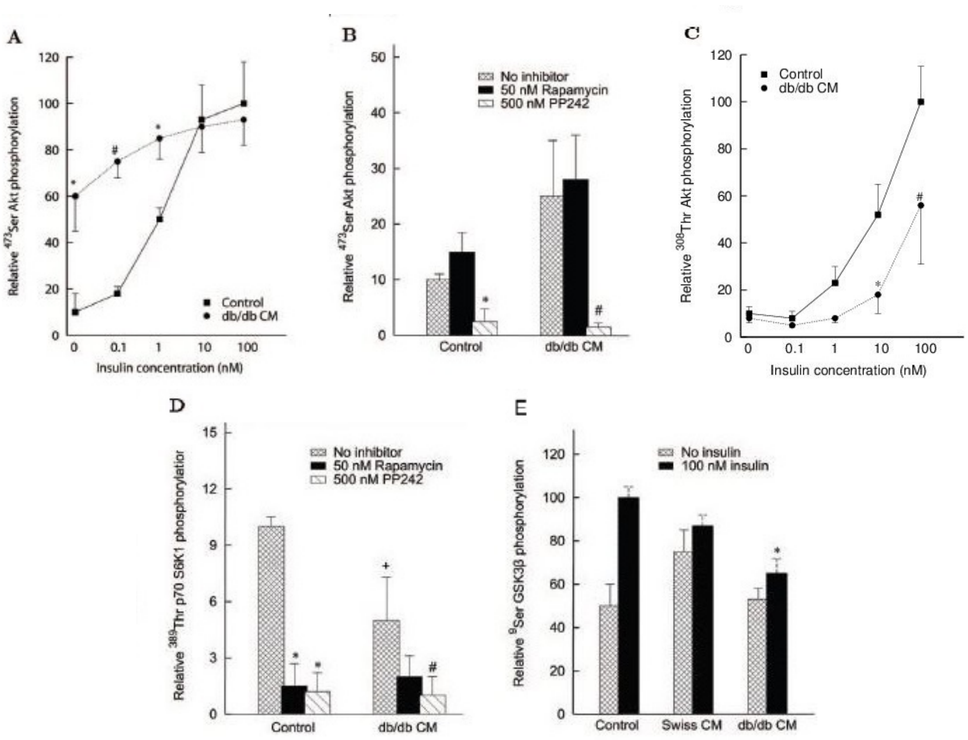

Figure 4.1: Experimental data of L6 myoblasts reported in [13] and used for the parameter estimation of the ISN model. Data are expressed as fold change versus control condition (control at 100 nM insulin set at 100). Data are mean ± s.d. *Panel A*: Dose-response curve of pAkt(Ser473) vs insulin concentration (nM) in logarithmic scale in the absence (squares) or presence (circles) of db/db CM proteins. *Panel B*: Effect of mTORC inhibitors (Rapamycin or PP242) on basal ^{473}Ser Akt phosphorylation in both control and db/db CM treated cells. *Panel C*: Dose-response curve of pAkt(Thr308) vs insulin concentration (nM) in logarithmic scale in the absence (squares) or presence (circles) of db/db CM proteins. *Panel D*: Effect of mTORC inhibitors (Rapamycin or PP242) on basal ^{389}Thr p70S6K1 phosphorylation in both control and db/db CM treated cells. *Panel E*: ^{9}Ser GSK3β phosphorylation in control, in Swiss CM treated cells (data not used for the parameter estimation), and db/db CM treated cells with or without insulin.

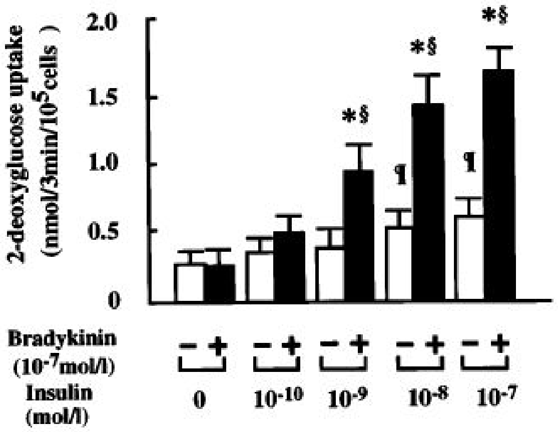

Figure 4.2: Experimental data of L6 myoblasts reported in [124] and used for the parameter estimation of the ISN model. 2-deoxyglucose uptake measured in L6 myoblasts in the presence (black bars) or absence (white bars) of bradykinin (10^-7 mol/l) after preincubation with various concentrations of insulin $(0, 10^{-10}, 10^{-9}, 10^{-8}$ and 10^{-7} mol/l. Results are expressed as the mean ± s.d. (n=6).

of the data reported by Miyata et al. in [124]. In this work, the Authors wanted to determine how bradykinin, a peptide involved in multiple biological processes (such as vasodilatation, increase in capillary permeability, smooth muscle relaxation/contraction, and inflammation) affected insulin-stimulated glucose uptake in dog skeletal muscle and rat L6 myoblasts. They found that bradykinin significantly increased 2-deoxyglucose (2-DG) uptake in isolated muscle and L6 myoblasts in the presence of insulin in a dose-dependent manner, but not in the absence of insulin (Fig. 4.2). 2-Deoxyglucose is a glucose molecule which has the 2-hydroxyl group (one oxygen atom connected by a covalent bonding to one hydrogen atom) replaced by hydrogen, so that it cannot undergo glycolysis when taken up by the cell. 2-DG is taken up by the glucose transporters of the cell (GLUT4 for the skeletal muscle cells) and, therefore, cells with higher concentrations of glucose transporters also have a higher uptake of 2-DG. We assumed that there exists a proportional relation between the levels of 2-DG measured by Miyata et al. [124] in L6 myoblasts in the absence of bradykinin at the various concentrations of insulin, and the GLUT4 levels ate plasma menbrane in the same cell line and the same condition. In view of this assumptions, to estimate the GLUT4 parameters, we used the data of Fig. 4.2 (white bars) normalized to the value of the maximal insulin concentration.

C2C12 myoblasts data In order to verify the present ISN model is able to represent data from different cell lines and different experimental conditions, we used the data reported in [123] to estimate the ISN parameters of the C2C12 cells. In [123] the Authors investigated the effects on insulin signaling regulation of selective inhibitions of PIP3 phosphatases (SKIP, SHIP2 and PTEN) by small interfering RNA (siRNA) in the C2C12 myoblasts. As widely discussed in Chapter 1, PTEN (phosphatase and tensin homologue) acts by removing the phosphate in the 3-position of PI(3,4,5)P3 to produce PI(4,5)P2 while SHIP2 (SH2 domain-containing inositol polyphosphate phosphatase) specifically hydrolyzes the 5-phosphate of PI(3,4,5)P3 to produce PI(3,4)P2. SKIP (skeletal muscle and kidney enriched inositol polyphosphate 5-phosphatase) is an other phosphatase abundantly expressed in the skeletal muscle that hydrolyzes PI(3,4,5)P3 to downregulate its intracellular levels [126]. SKIP is localized to the endoplasmic reticulum under basal conditions and is translocated to the membrane ruffles [2] in response to insulin. The action of SKIP, SHIP2 and PTEN on PIP3 is represented in Figure 4.3. Several studies have shown that SKIP, SHIP2, and PTEN negatively regulate insulin-dependent glucose incorporation [126, 127, 128]. Based on these studies, all of the PIP3 phosphatases are implicated in the regulation of insulin signaling, but several important findings about the differences between the PIP3 phosphatases are also reported. It is stated, however, that the exact role of these PIP3 phosphatases in the regulation of insulin signaling in the skeletal muscle remains unknown.

In [123] the Authors measured the relative phosphorylation levels of some players of the ISN for different insulin concentrations in C2C12 myoblasts transfected with small interfering RNA (siRNA) of PTEN, SKIP and SHIP2 (see Figures 4.4, 4.5, 4.6). Among these data, we used only the experimental data for control and for PTEN-suppressed cells (PTEN protein concentration was reduced up to 10% of control) because SKIP and SHIP2 were not included in the present ISN model. In particular, for the parameter estimation of C2C12 cells, we used the normalized phosphorylation levels of IR(Tyr1146), Akt(Ser473) and (Thr308), GSK3β(Ser9) and S6K1(Thr389) at zero insulin and at insulin concentrations of 1, 10, and 100 nM. In addition, we considered the normalized concentration of GLUT4$_{pm}$ at the cell surface in basal (zero insulin) conditions and in cells stimulated with 100 nM of insulin for 15 min

---

[2] Membrane ruffles are actin-rich protrusions of the plasma membrane that can be observed on the surface of many cell types.

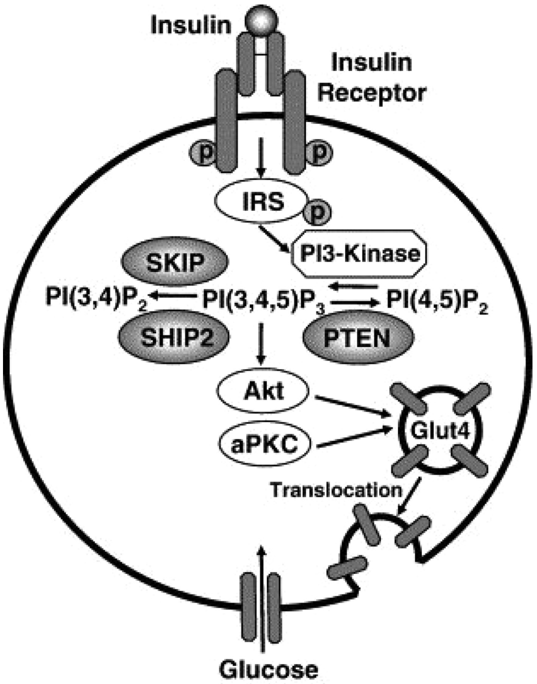

Figure 4.3: Role of PTEN, SKIP and SHIP2 in the regulation of insulin signaling in skeletal muscle cells. PTEN, SKIP and SHIP2 are PIP3 phosphatases that regulate insulin-dependent glucose incorporation. PTEN acts removing the phosphate in the 3-position of PI(3,4,5)P3 to produce PI(4,5)P2. SKIP and SHIP2 hydrolyze PI(3,4,5)P3 to produce PI(3,4)P2.

(Figure 4.5). The data of PIP3 and AS160(Thr642) shown in Fig. 4.6 were used for the prediction. All protein levels were measured by Western blotting analysis and immunoprecipitation and quantified by densitometry.

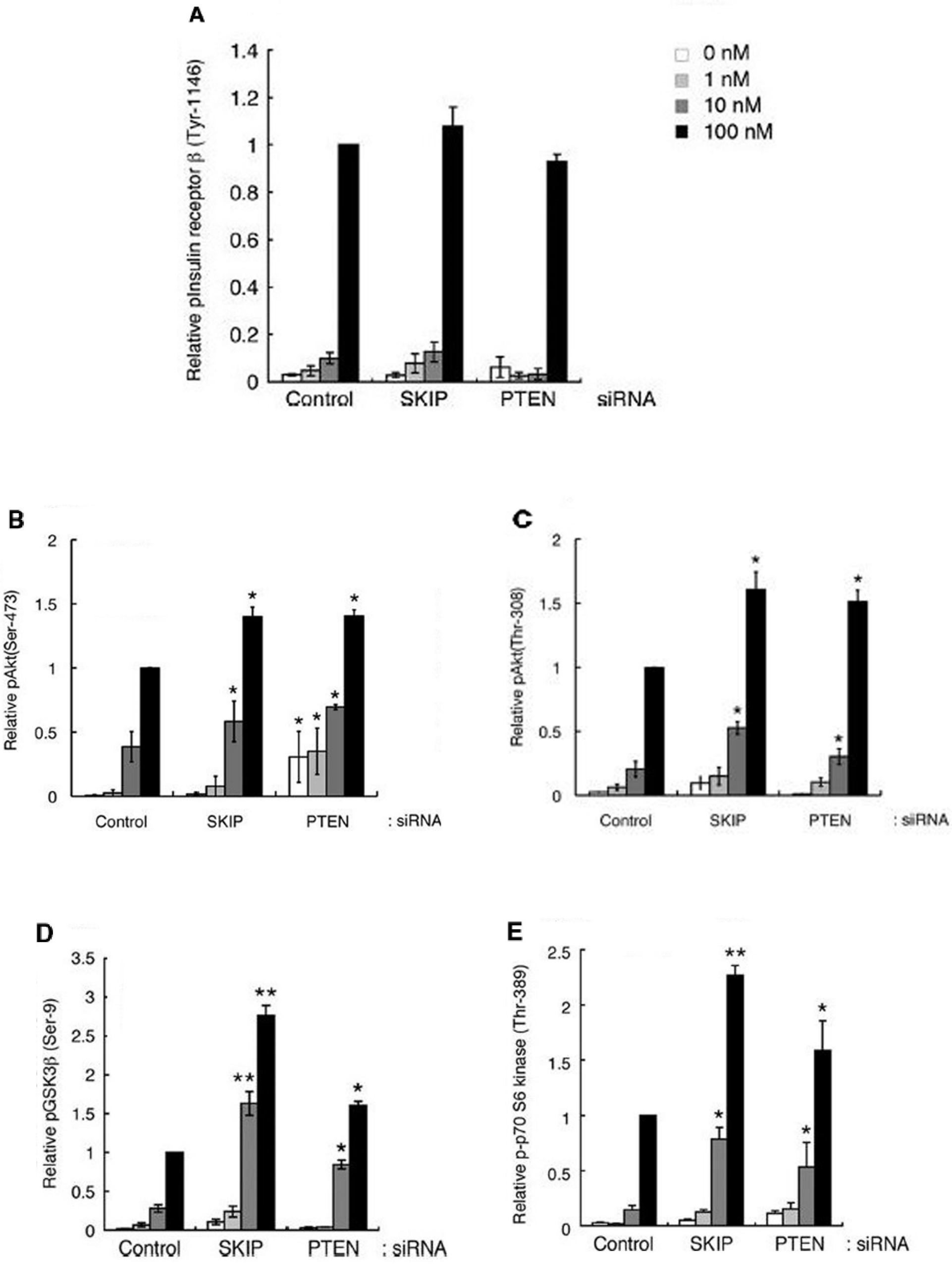

Figure 4.4: Experimental data of C2C12 myotubes reported in [123] and used for the parameter estimation of the ISN model. Phosphorylation levelss in C2C12 cells transfected with specific siRNAs at insulin concentrations of 0, 1, 10, 100 nM. Data are expressed as fold change versus control condition at 100 nM insulin (data related to SKIP not considered in for the parameter estimation). Data are mean ± s.e. (error bars). *Panel A*: Insulin-stimulated phosphorylation of pIR(Tyr116). *Panel B*: Insulin-stimulated phosphorylation of pAkt(Ser473). *Panel C*: Insulin-stimulated phosphorylation of pAkt(Thr308). *Panel D*: Insulin-stimulated phosphorylation of pGSK3β(Ser9). *Panel E*: Insulin-stimulated phosphorylation of p70S6K1(Thr389).

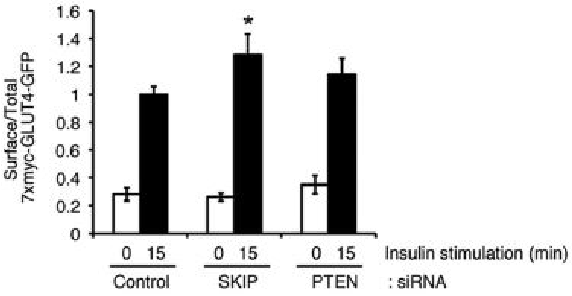

Figure 4.5: Translocation of GLUT4 at the cell surface in the basal or insulin-stimulated C2C12 cells. Surface-to-total distribution of GLUT4 reporter was analyzed in C2C12 cells expressing GLUT4 reporter. Cells were stimulated with 100 nM of insulin for 15 min in control, SKIP-directed and PTEN-directed siRNA.

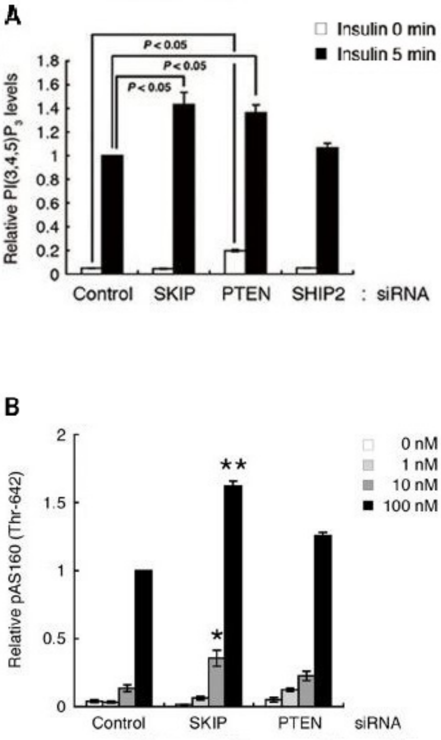

Figure 4.6: Experimental data of C2C12 myotubes reported in [123] and used for predictions of the ISN model. Data are presented as the mean ± s.e. (error bars). *Panel A*: Relative PI(3,4,5)P3 levels in the insulin-stimulated C2C12 cells transfected with control, SKIP-, SHIP2- or PTEN-directed siRNA. *Panel B*: Insulin-stimulated AS160 phosphorylation in C2C12 cells transfected with the indicated siRNAs.

4.2 Estimation procedure and optimization algorithm

The optimal values of the ISN model parameters were estimated by fitting the model equations at the steady state (3.2.96)-(3.2.114) to the experimental data through minimization of a least-squares index. In other words, according to the Ordinary Least Squares (OLS) method described in section 2.2.2 of Chapter 2, we implemented an estimation algorithm that aimed to minimize the sum of squared residuals, i.e. the differences between the model-based predictions and the available data. Such optimization algorithm, implemented using the C programming language, consists in the following steps:

1. The model parameter values are initialized.
2. For any insulin concentrations, model equations (3.2.96)-(3.2.114) are solved numerically by reducing to a non-linear system in only two variables, $\mathrm{PDK1_n}$ and $\mathrm{mTORC2_n}$, through a series of cascade substitutions.
3. As the experimental data were normalized to have a unity value at maximal insulin concentration in control, the concentrations of the measured quantities are computed according to this constraint.
4. The cost function defined as the sum of squared residuals is computed.
5. A numerical optimization routine searches for the cost function minimum repeating Steps 2-4. When the routine converges, the algorithm stops providing the optimal parameter values.

To find the numerical solution of the optimization problem, we used a local routine implementing a derivative-free algorithm for bound constrained optimization problems (Package SDBOX available at the Software Library of the Department of Computer and System Science, Sapienza University of Rome). The choice of a local optimization routine, whose performance may depend on the initial parameter vector, was motivated by the availability of *a priori* information about this initial value, obtained both from a careful analysis of the literature and from an extensive series of preliminary numerical simulations. Moreover, we constrained the local routine to search for the optimal parameter values in the wide range [0,500].

The parameter estimation for the two cell lines was characterized by some differences and some common hypothesis suggested by the data observation and the literature knowledge. Such differences and common assumptions will be detailed in the following sections.

4.3 Estimates of ISN model parameters and optimal fitting curves for L6 myoblasts

We used the L6 data described in section (4.1) to estimate the following parameters of the ISN model: the value of $I_{e,0.5}$ defined in (3.2.98) letting $S_{0.5}$ fixed as no IR data were available; the IRS1 parameters a_3 and a_4; the PI3K parameters a_6 and $a_6^{'}$; the PIP3 parameter a_8; the PDK1 parameter a_9 assumed equal to the mTORC2 parameter a_{10} as no data on the phosphorylation of PDK1 and mTORC2 were available; the mTORC2 parameter a_{12}; the factor J that activates mTORC2 for db/db with a_{11} set to 1; the Akt parameters a_{13}^{δ}, a_{15}^{ϵ}, a_{17}^{δ}, a_{17}^{γ}, a_{19}^{δ}, a_{19}^{γ}, $a_{\theta\epsilon}$ and $a_{\eta\delta}$; the GSK3β parameters a_{23} and $a_{23}^{'}$ (only for db/db as $a_{23}^{'}$ is zero for control); the mTORC1 parameter a_{24}; the S6K1 parameters a_{26}, a_{26}^{μ} and a_{27}; and the GLUT4 parameters a_{28}, a_{29} and a_{30}.

We fit the experimental data assuming that: i) J has negligible concentration in control medium and a larger concentration, to be estimated, in db/db medium; ii) insulin resistance also increases because of an increased IRS1 degradation due to enhancement of mTORC2 signaling [129]. So, to fit the data of cells exposed to db/db medium, we reduced the values of $a_6^{'}$ and a_6 in Eq. (3.2.103) according to a twofold increase of IRS1 degradation rate constant (μ_{IRS1});iii) as the L6 data suggested that, for this cell line, $GSK3\beta$ is activated by pAkt(Ser473), we changed $\mathrm{Akt}_\mathrm{n}^\mathrm{T}$ into $\mathrm{Akt}_\mathrm{n}^\mathrm{S}$ in Eq. (3.2.111) and assumed $a_{23}^{'} > 0$ with $W = 1$ in db/db to represent the putative GSK3β sequestration; iv) the action of Rapamycin was accounted for by reducing a_{24} in (3.2.112) by a factor 0.1, and the action of PP242 by reducing a_{10} and a_{11} in Eq. (3.2.106) and a_{24} in Eq. (3.2.112) by a factor 0.15; v) to reduce the number of parameters to be estimated, the parameters a_2, a_7 and a_{10}^{μ} in Eqs. (3.2.100), (3.2.104), (3.2.106), that are likely to be small, were set to zero and the positive feedback loop from Akt to PTP1B was not included ($a_P = 0$ and then $PTP1B_n = 1$ from (3.2.102)); vi) the remaining parameters were fixed, i.e. $\rho = 0.03$ in (3.2.98), $S_{0.5} = 2.5 \cdot 10^{-2}$ in (3.2.99), $W = 1$ in (3.2.111), $a_{21} = 0.5$ in (3.2.110).

We remark that the normalized experimental data of pAkt(Ser473) were fit by the sum $Akt_n^S + Akt_n^{S,T}$, given by Eqs. (3.2.108)-(3.2.109), because the specific monoclonal antibody is likely to bind Akt phosphorylated on Ser473 irrespective of the presence of the phosphorylated Thr308. Similarly, the data of pAkt(Thr308) were fit by $Akt_n^T + Akt_n^{S,T}$. All parameters to be estimated were constrained to be nonnegative and to belong to the box [0, 500]. Moreover, in view of the definition of some model parameters, further constrains were necessary. In particular, since from (3.2.98), (3.2.99) IR parameters a_0 and a_1 are related to $I_{e,0.5}$ and $S_{0.5}$ by the equations

$$a_0 = \left(\frac{1}{2S_{0.5}} - \frac{I_{e,0.5}}{1-2\rho}\right)\frac{1-\rho}{1-2\rho}\,, \tag{4.3.1}$$

$$a_1 = \left(4I_{e,0.5}\frac{1-\rho}{1-2\rho} - \frac{1}{S_{0.5}}\right)\frac{1-\rho}{1-2\rho}\,, \tag{4.3.2}$$

the terms in parenthesis were constrained to be positive to ensure the positivity of a_0 and a_1. The quantities $a_{17}^{\delta} - a_{17}^{\gamma} a_{\eta\delta}$ and $a_{19}^{\epsilon} - a_{19}^{\gamma} a_{\theta\epsilon}$ in (3.2.107)-(3.2.109) were constrained to be positive. In addition, noting that $a_{17}^{\gamma} a_{19}^{\epsilon} a_{\eta\delta} + a_{19}^{\gamma} a_{17}^{\delta} a_{\theta\epsilon} - a_{17}^{\delta} a_{19}^{\gamma}$ in $D_1^{'}$ equals $a_{17}^{\delta} a_{19}^{\gamma}(\mu_{Akt}/\gamma)$, we assumed $\mu_{Akt}/\gamma \ll 1$.

Table 4.1 (4^{th} and 5^{th} columns) reports the parameter estimates and Figure 4.7 shows the experimental data of L6 cells, replotted from [13] and [124], along with the optimal fitting curves. The phosphorylation data measured in the experiments with db/db medium are fit with a value of J substantially larger compared to control (0.07 vs. 0.001). pAkt(Ser473) at zero insulin is largely increased, but its response to insulin is blunted (see Fig. 4.7 panel A). We observe that a high value of pAkt(Ser473) at zero insulin can only be obtained if mTORC2 is also activated through a signaling pathway independent of PI3K, and if the Thr308 Akt phosphorylation is not required for Ser473 phosphorylation. The response of pAkt (Thr 308) and of pGSK3β(Ser9) is also depressed (panels B and C of Fig. 4.7). The 2-DG uptake data in control reported in Fig. 4.7 D were adequately fit by the model. The predicted 2-DG uptake in the presence of db/db medium was computed by assuming that the rate constants that regulate GLUT4 translocation to plasma membrane are smaller compared to control [7, 8]. Actually, in T2D subjects, GLUT4 mRNA and protein levels are reduced in adipose tissue (GLUT4 concentration reduced to 50% of control in [19]) but not in skeletal muscle [7], suggesting that a defective regulation of GLUT4 translocation may contribute to insulin resistance in L6 cells exposed to the db/db medium. We accounted for the diminished capacity of GLUT4 vesicles to reach plasma membrane in the presence of db/db medium by decreasing the parameters a_{28} and a_{29} in Eq. (3.2.114) (see Table 4.1).

The data measured in the presence of Rapamycin and PP242 are shown Fig. 4.7 panels E-F. The model adequately fits the inhibition of basal (no insulin) pS6K1(Thr389) both in control and db/db medium (panel F). In the basal pAkt(Ser473) data (Fig. 4.7, panel E), the poor prediction for cells exposed to db/db medium is likely caused by experimental variability and the data were not used for model fitting. In cells treated with Rapamycin, the attenuated negative feedback led to an increase of $\mathrm{mTORC2_n}$, thus enhancing pAkt. By contrast, PP242 affects Akt phosphorylation at Ser473, so $\mathrm{Akt^S}$ and $Akt^{T,S}$ are strongly reduced. Overall, it appears that the present model provides an adequate fitting of the L6 data.

A subset of model predictions is displayed in Fig. (4.8). We stress that mTORC1 inhibition leads in turn, because of attenuated negative feedback via S6K1, to a decrease in $\mathrm{IRS1_n^S}$ and an increase in $\mathrm{IRS1_n^Y}$ thus enhancing insulin signaling (panels A-D). In panel E of (4.8) we plotted the values assumed by $\mathrm{PDK1_n}$ and $\mathrm{mTORC2_n}$ when I_e increases from zero to 100 nM for control and db/db medium while panel F gives a 3D representation of the components of pAkt. At 100 nM insulin, total pAkt is 78.7% of total Akt in control.

The L6 cell data were also analyzed in the presence of the positive feedback, with the constant a_P in Eq. (3.2.102) set to a smaller value for the cells in db/db medium compared to control. The results, however, did not appear to improve on those obtained without the positive feedback.

We also performed a sensitivity analysis in order to investigate how parameter changes influence the system behaviour at the steady state and to identify those parameters that have the greatest impact on the system output. The sensitivities of the normalized concentrations of proteins with respect to model parameters were computed (both for control and for cells exposed to conditioned (db/db) medium), as the derivative of log concentration with respect to log parameter at the optimum (see section 2.3). The use of these relative sensitivities provids nondimensional quantities that do not depend on the absolute values of concentrations and parameters. Sensitivities were evaluated numerically upon a $\pm 10\%$ perturbation of the parameters. The results are presented in the form of matrices where the numerical values, which are positive for a positive regulation and negative for an inhibition, are converted to a color. Figure (4.9) shows the sensitivities of protein concentrations to the estimated model parameters at the extracellular insulin concentration of 9.69 nM (estimated $I_{e,0.5}$). We remark that the sensitivities to $a_6^{'}$ and $a_{23}^{'}$ are small according to the small values of the estimates whereas, as expected, the sensitivities to the factor J increase in cells exposed to the db/db medium compared to control. The sensitivity to a_{12} is small suggesting that the effect of the negative feedback loop from S6K1 to mTORC2 can be negligible.

Proteins	Parameters	C2C12	L6	
			Ctr	db/db
IR	$I_{e,0.5}\,(nM)$	44.68	9.69	-
	$S_{0.5}\,(nM)^{-1}$	0.01	0.025	-
IRS1	a_3	8.26	1.88	-
	a_4	24.12	4.70	-
PI3K	$a_6^{'}$	0	$1.3 \cdot 10^{-3}$	$0.66 \cdot 10^{-3}$
	a_6	124	14.50	3.62
PIP$_3$	a_8	0.05	1.85	-
PDK1	a_9	0.49	6.61	-
	a_{10}	0.49	6.61	-
mTORC2	a_{11}	0	1	-
Akt	a_{12}	$5 \cdot 10^{-3}$	$1.2 \cdot 10^{-7}$	-
	a_{13}^{δ}	$9.2 \cdot 10^{-4}$	0.34	-
	a_{15}^{ϵ}	0.22	5.80	-
	a_{17}^{δ}	0.92	3.84	-
	a_{17}^{γ}	0.20	0.29	-
	a_{19}^{ϵ}	7.95	0.67	-
	a_{19}^{γ}	12.88	0.65	-
	$a_{\theta\epsilon}$	0.62	1.0	-
	$a_{\eta\delta}$	0.11	$2.5 \cdot 10^{-3}$	-
FoxO1	a_{21}	0.5	0.5	-
GSK3β	a_{23}	2.92	12.54	-
	$a_{23}^{'}$	0	0	3.35
mTORC1	a_{24}	0.01	0.17	-
S6K1	a_{26}	66.01	39.06	-
	a_{26}^{μ}	0.13	0.90	-
	a_{27}	74.12	460	-
GLUT4	a_{28}	0.14	0.22	0.15
	a_{29}	24.67	1.20	0.67
	a_{30}	28.16	2.01	-

Table 4.1: Parameters estimated from data of C2C12 and L6 cells.

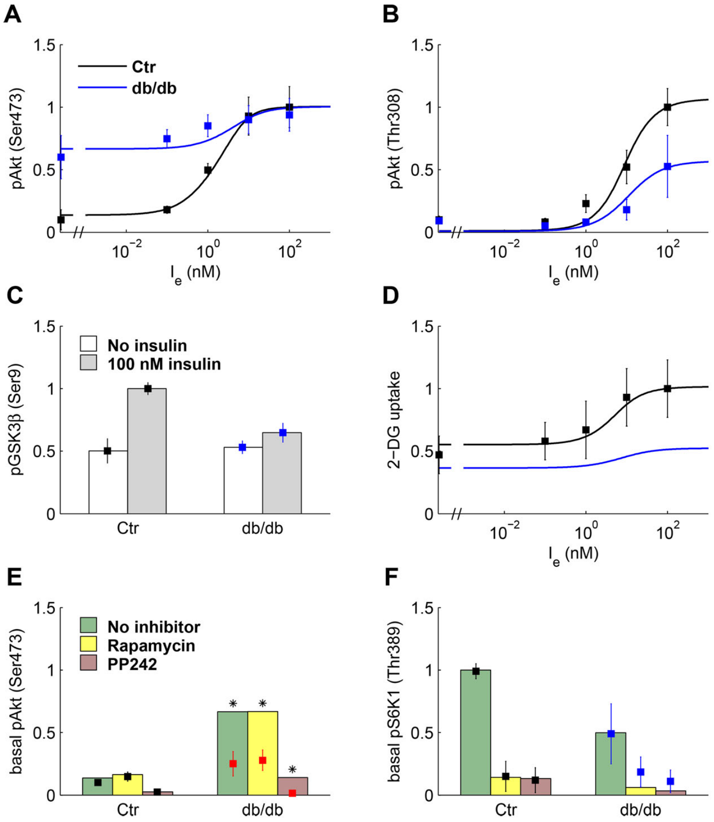

Figure 4.7: Experimental data of L6 myotubes and model fitting. Data (mean ± SD) replotted from Ref. [13] except in panel D from Ref. [124]. Data (squares) and model fitting (solid lines) plotted in black for control and in blue for cells exposed to conditioned (db/db) medium. (A, B) Relative pAkt(Ser473) and pAkt(Thr308). (C) Relative pGSK3β(Ser9) at zero (white box) and 100 nM (gray box) insulin. (D) Relative 2-DG uptake in rat L6 myoblasts. (E) Relative pAkt(Ser473) at zero insulin in control (black) and cells exposed to db/db medium (red), in the absence of inhibition and in cells treated with rapamycin (50 nM) and PP242 (500 nM). The red color indicates that experimental values do not preserve the increase in basal pAkt(Ser473) from control to db/db medium in the absence of inhibition, and asterisks point out that these data were not used in model fitting. The boxes represent model fitting with the color code: green (no inhibitor), yellow (rapamycin), and pink boxes (PP242).(F) Relative pS6K1(Thr389) at zero insulin in the absence of inhibition and in treated cells. The boxes represent model fitting with the same color code of Panel E.

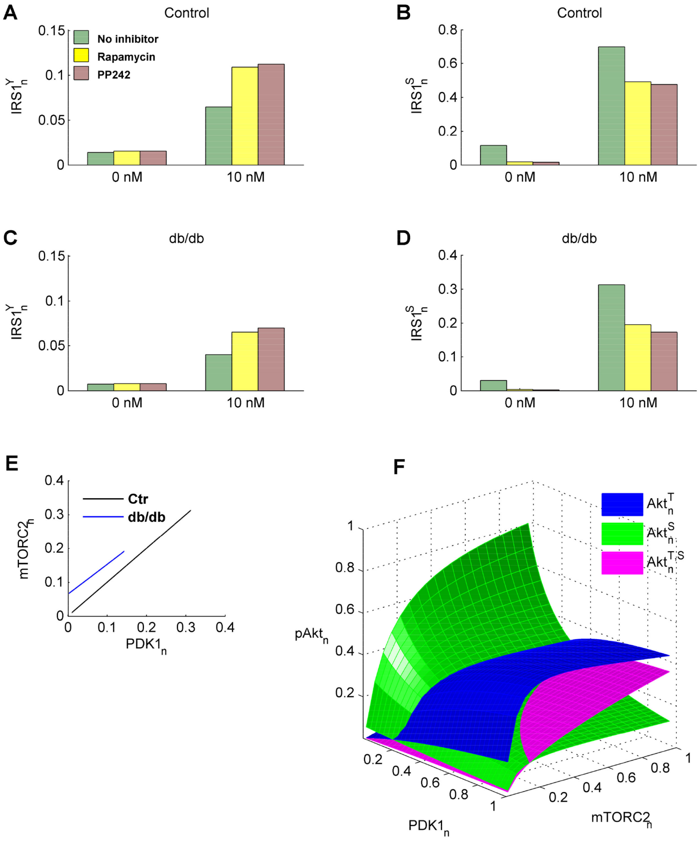

Figure 4.8: Model predictions for L6 myotubes. (A, B) Model prediction of $\mathrm{IRS1}^{\mathrm{Y}}_{\mathrm{n}}$ (panel A) and $\mathrm{IRS1}^{\mathrm{S}}_{\mathrm{n}}$(panel B) for cells in control medium at zero and 10 nM insulin in the absence of inhibitor (green), and in the presence of 50 nM rapamycin (yellow) and 500 nM PP242 (pink). (C, D) Model predictions as in (A) and (B), but for cells exposed to db/db medium. Panels A-D show the different effect of the decreased negative feedback on the tyrosine and serine residues of IRS1. (E) Plot of values assumed by $\mathrm{PDK1}_{\mathrm{n}}$ (abscissa) and $\mathrm{mTORC2}_{\mathrm{n}}$ (ordinate) when I_e increases from zero to 100 nM for control and db/db medium. (F) 3D plot of $\mathrm{Akt}^{\mathrm{T}}_{\mathrm{n}}$, $\mathrm{Akt}^{\mathrm{S}}_{\mathrm{n}}$, and $\mathrm{Akt}^{\mathrm{T,S}}_{\mathrm{n}}$ as a function of $\mathrm{PDK1}_{\mathrm{n}}$ and $\mathrm{mTORC2}_{\mathrm{n}}$ according to Eqs. (3.2.107)-(3.2.109). With the present estimates of Akt model parameters, $\mathrm{Akt}^{\mathrm{S}}_{\mathrm{n}}$ increases with $\mathrm{mTORC2}_{\mathrm{n}}$ and decreases with $\mathrm{PDK1}_{\mathrm{n}}$, while $\mathrm{Akt}^{\mathrm{T,S}}_{\mathrm{n}}$, and less clearly $\mathrm{Akt}^{\mathrm{T}}_{\mathrm{n}}$, increase with both $\mathrm{PDK1}_{\mathrm{n}}$ and $\mathrm{mTORC2}_{\mathrm{n}}$.

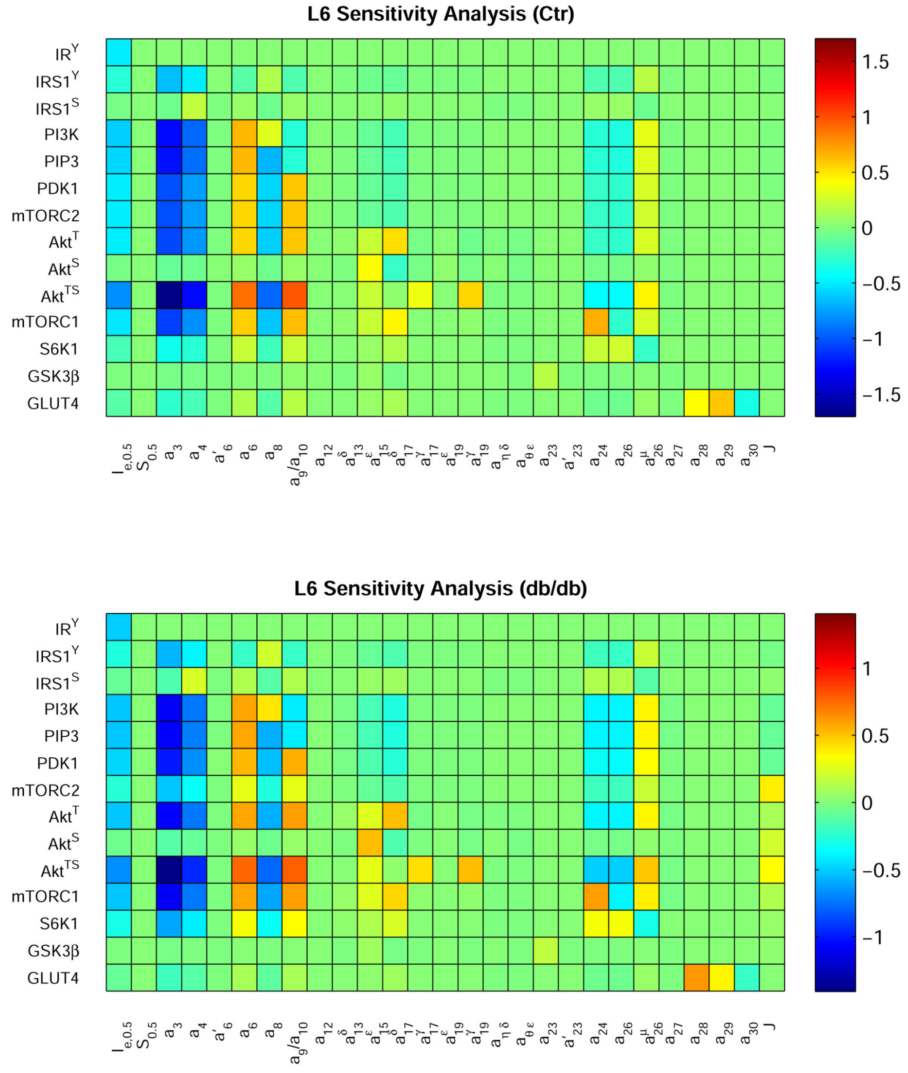

L6 Sensitivity Analysis (Ctr)

L6 Sensitivity Analysis (db/db)

Figure 4.9: Sensitivity analysis for the ISN model of L6 myotubes. The plot shows the sensitivities of protein concentrations to the estimated parameters of the model at the extracellular insulin concentration of 9.69 nM ($I_{e,0.5}$) for control cells (upper panel) and cells in db/db medium (lower panel).

4.4 Estimates of ISN model parameters and optimal fitting curves for C2C12 myotubes

From the C2C12 data, we estimated: the quantities $I_{e,0.5}$ and $S_{0.5}$ characterizing the dose-response curve of $\mathrm{IR}_{\mathrm{n}}^{\mathrm{Y}}$ (see (3.2.98), (3.2.99)); the IRS1 parameters a_3 and a_4; the PI3K parameter a_6; the PIP3 parameter a_8; the PDK1 parameter a_9 assumed equal to the mTORC2 parameter a_{10} as no data on the phosphorylation of PDK1 and mTORC2 were available; the mTORC2 parameter a_{12}; the Akt parameters a^{δ}_{13}, a^{ϵ}_{15}, a^{δ}_{17}, a^{γ}_{17}, a^{δ}_{19}, a^{γ}_{19}, $a_{\theta\epsilon}$ and $a_{\eta\delta}$; the GSK3β parameter a_{23}; the mTORC1 parameter a_{24}; the S6K1 parameters a_{26}, a^{μ}_{26} and a_{27}; and the GLUT4 parameters a_{28}, a_{29} and a_{30}.

To fit the C2C12 data, we assumed that: i) PTEN normalized concentration was equal to 1 in control and to 0.1 in PTEN-silenced cells in according with the experiments in [123]; ii) basal IR autophosphorylation at zero insulin (denoted as ρ in (3.2.98), (3.2.99)) was set to 0.03 in view of the data in [123]; iii) the parameter a_P of positive feedback in (3.2.102) was set to zero because IR tyrosine phosphorylation is similar in control and PTEN-silenced cells (Fig. 4.4 panel A); iv) the factor J was considered negligible and then a_{11} in (3.2.106) was set to zero; v) to reduce the number of parameters to be estimated, the model parameters a_2, a_7 and a^{μ}_{10} in Eqs. (3.2.100), (3.2.104), (3.2.106), that are likely to be small, were set to zero as well as a'_6 in (3.2.103) and a'_{23} in (3.2.111).

Moreover, as for the L6 cells, the normalized experimental data of pAkt(Ser473) and pAkt(Thr308) were fit by the sum $Akt^S_n + Akt^{S,T}_n$ and $Akt^T_n + Akt^{S,T}_n$, respectively, and all parameters were constrained to be nonnegative and to belong to the box [0, 500]. We implemented the constraints that guarantee the positivity of a_0 and a_1 (see (4.3.1)) and of the quantities $a^{\delta}_{17} - a^{\gamma}_{17} a_{\eta\delta}$ and $a^{\epsilon}_{19} - a^{\gamma}_{19} a_{\theta\epsilon}$ in (3.2.107)-(3.2.109). Finally, recalling that $a^{\gamma}_{17} a^{\epsilon}_{19} a_{\eta\delta} + a^{\gamma}_{19} a^{\delta}_{17} a_{\theta\epsilon} - a^{\delta}_{17} a^{\gamma}_{19}$ in D'_1 is equal to $a^{\delta}_{17} a^{\gamma}_{19} (\mu_{Akt}/\gamma)$, we also imposed $\mu_{Akt}/\gamma \ll 1$.

Table 4.1 reports in the third column the parameter estimates for C2C12 cells. It is worth noting that $I_{e,0.5}$ was found equal to 44.68 nM, a value larger than that of L6 cells. Moreover, we note that the parameter estimates reported in Table 4.1 are rather different between C2C12 and L6 cells, which however is not surprising since C2C12 is a line of mouse myoblasts whereas L6 is a line of rat myotubes. Figure 4.10 displays the data of C2C12 cells, replotted from [123], and the optimal fitting curves computed by the present model. The ISN model was able to adequately fit the available C2C12 data.

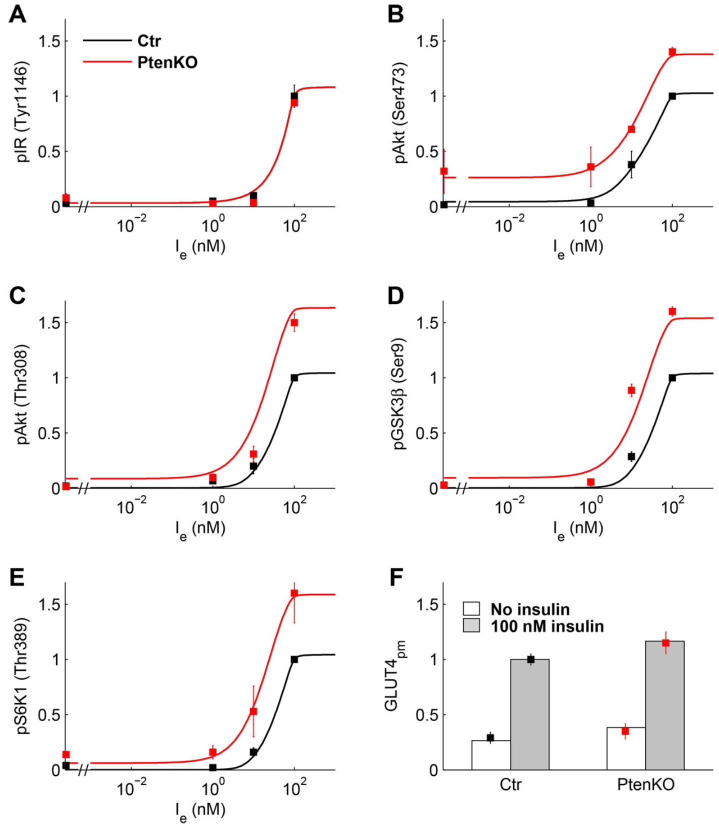

Figure 4.10: Experimental data of C2C12 myoblast cells and model fitting. Data (mean ± SEM) replotted from [123] for control (black squares) and PTEN-suppressed (red squares) cells. Solid lines are the dose-response curves (logaritmic scale) predicted by the model for control (black) and PTEN-suppressed cells (red). (A) Relative pIR(Tyr1146). (B, C) Relative pAkt(Ser473) and pAkt(Thr308). (D) Relative pGSK3 β(Ser9). (E) Relative pS6K1(Thr389). (F) Relative GLUT4 at PM at zero (white box) and 100 nM (gray box) insulin.

As expected, PTEN deletion enhances the insulin response and basal level increased in almost all proteins and, in particular, PTEN protein suppression causes an increase in basal Ser473 Akt phosphorylation, which may phosphorylate and deactivate FoxO1 with the possible enhancement of signaling to the pathways that regulate cell proliferation.

A subset of model predictions is displayed in Fig. 4.11. Panel A shows the prediction, obtained by the estimated model, of pAS160(Thr642) together with the data that were not used in the estimation procedure. While the profile of pAS160(Thr642) data was followed rather accurately, the model failed to predict PIP3 concentration data in the PTEN-silenced cells (panel

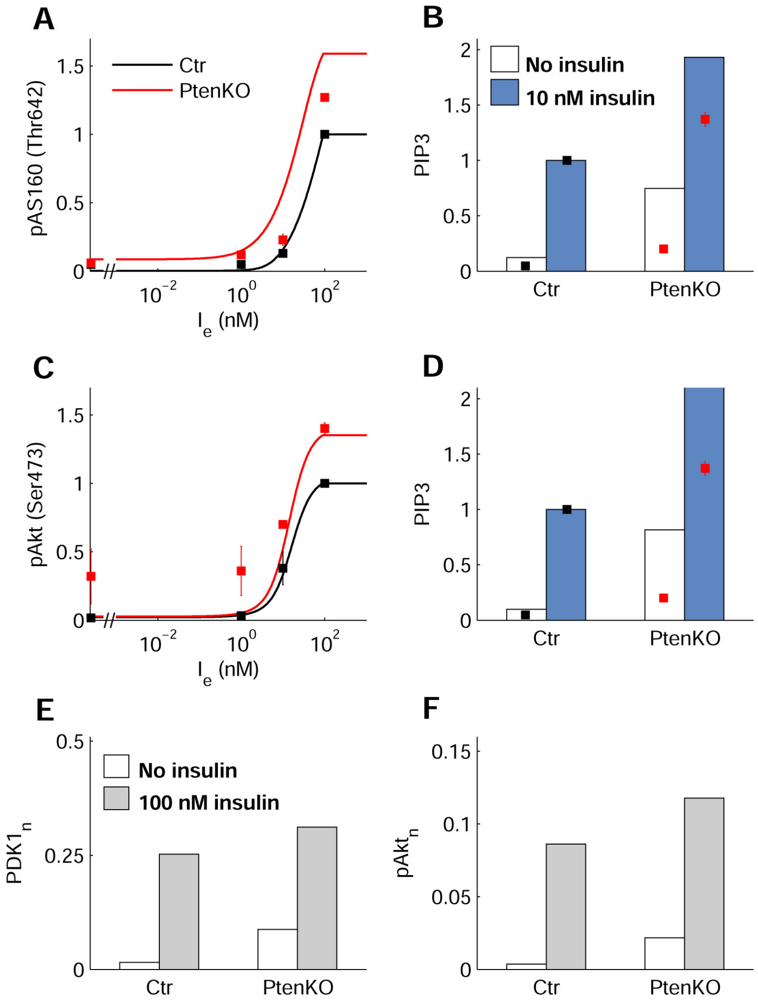

Figure 4.11: Experimental data of C2C12 myoblasts not used in the parameter estimation and model predictions. Data (mean ± SEM) in panels A and B are replotted from [123]. (A) Relative pAS160 (Thr642) concentration in control (black) and PTEN-suppressed (red) cells, together with the dose-response curves predicted by the model. The equation for pAS160 (Thr642) (inactive form) is given by $pAS160_n = 0.5(Akt_n^T + Akt_n^{T,S})/[1 + 0.5(Akt_n^T + Akt_n^{T,S})]$. (B) Relative PIP3 concentration in control (black squares) and PTEN-suppressed (red squares) cells with model prediction at zero insulin (white boxes) and 10 nM insulin (blue boxes). (C, D) Fitting of the relative pAkt(Ser473) and prediction of relative PIP3 in the hypothesis that mTORC2 is activated by PI3K instead of PIP3. (E) Model prediction of $\mathrm{PDK1_n}$ in control and PTEN-suppressed cells at zero (white boxes) and 100 nM insulin (gray boxes). (F) Model prediction of total $\mathrm{pAkt_n}$ in control and PTEN-suppressed cells at zero (white boxes) and 100 nM insulin (gray boxes).

B). We note that if mTORC2 were activated by PI3K instead of PIP3, the model could not adequately fit pAkt(Ser473) data at zero and low insulin in PTEN-silenced cells, nor the prediction of PIP3 concentration data would improve (Fig. 4.11, panels C, D). Moreover, we found that the total $\mathrm{pAkt}(\mathrm{Akt}_{\mathrm{n}}^{\mathrm{T}} + \mathrm{Akt}_{\mathrm{n}}^{\mathrm{S}} + \mathrm{Akt}_{\mathrm{n}}^{\mathrm{T,S}})$ at 100 nM insulin in control is 8.61% of total Akt (Fig. 4.11 panel F) and GLUT4 at the plasma membrane is about 50% of total GLUT4. These values agree with the model results reported in [17], where pAkt is about 9% of total Akt and surface GLUT4 attains 40% of total GLUT4 after 15 min 100 nM insulin.

We performed a sensitivity analysis around the optimal parameter values also for the C2C12 cells. Figure 4.12 shows the sensitivities of protein concentrations upon a $\pm 10\%$ perturbation of the estimated parameters at the extracellular insulin concentration of 44.68 nM. As this concentration equals $I_{e,0.5}$, the sensitivity to $S_{0.5}$ is vanishing. The same occurs for the sensitivities to a_{12}, a_{13}^{δ} and a_{17}^{γ} that have small values. The largest positive sensitivities are found for a_9 and a_{10}, whose values were set equal (see Table 4.1) as no data on the phosphorylation of PDK1 and mTORC2 were available. The sensitivity to a_{12} is again small as in L6 cells, suggesting that the negative feedback loop from S6K1 to mTORC2 has a negligible role in both cell lines. The parameters that directly affect the downstream proteins, as mTORC1 and S6K1, also affect the upstream proteins, as IRS1 and PI3K, because of signaling through the negative feedback loop. The opposite behavior of $\mathrm{IRS1}^{\mathrm{Y}}$ and $\mathrm{IRS1}^{\mathrm{S}}$ is also noted. We also stress the negative sensitivity to a_8 of all proteins downstream PTEN, whereas $IRS1^{Y}$ and PI3K are positively regulated. Let us note that the sensitivity values in control cells and in PTEN-suppressed cells belong to different ranges. Moreover, the general pattern of the sensitivities for the C2C12 cells is similar to that found for L6 cells, confirming that the model is able to represent both types of data.

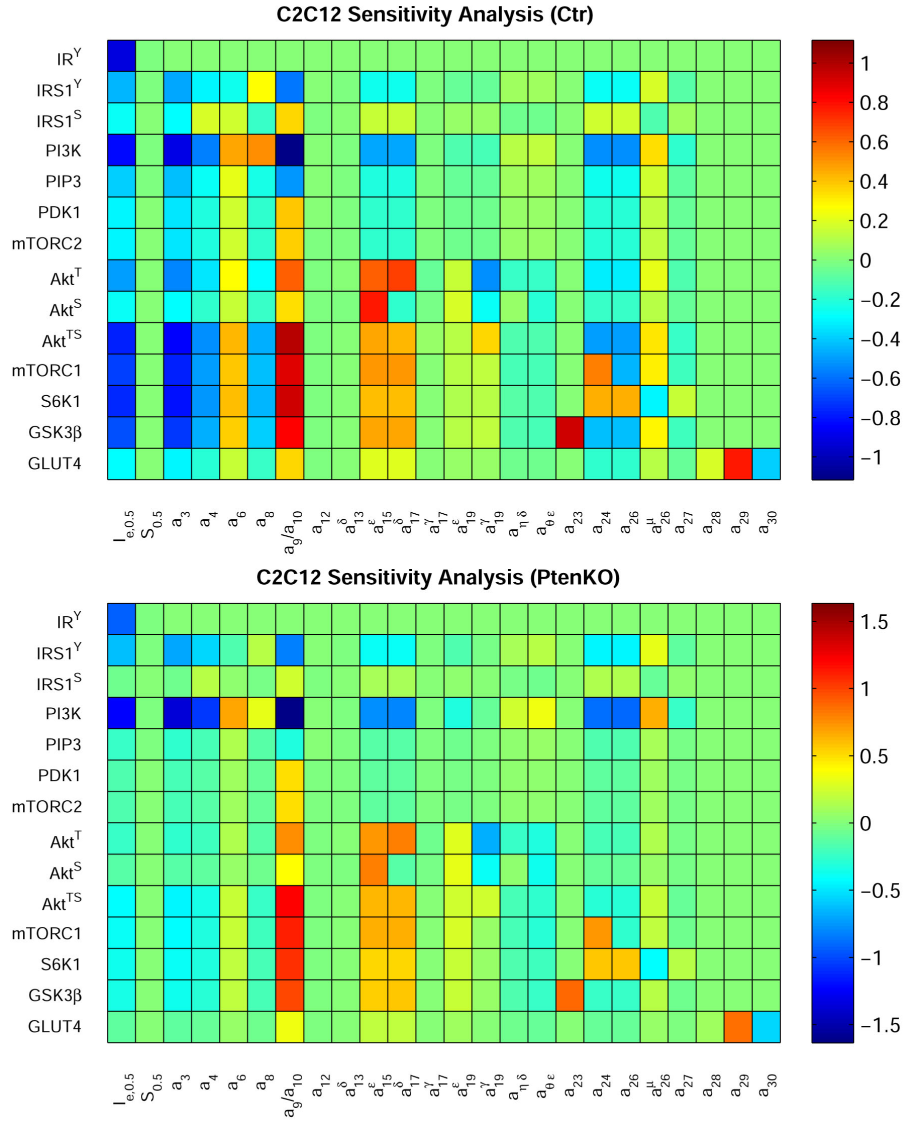

Figure 4.12: Sensitivity analysis for the ISN model of C2C12 myocytes. The plot shows the sensitivities of protein concentrations to the estimated parameters of the model at the extracellular insulin concentration of 44.68 nM in control cells (upper panel) and in PTEN-suppressed cells (lower panel).

4.5 Effects of inhibitors and of gene knockout and identification of potential drug targets

A test of model validity is that of ascertaining whether it is able to represent the effects of inhibitors and of conditions such as gene knockout or RNA interference. For instance, our model may represent the following particular conditions:

- *PI3K inhibitors.* The effect of PI3K inhibitors, such as Wortmannin and PIK-90, may be represented by a reduction of the catalytic constant k_{6c} in (3.2.70). A strong decrease in k_{6c} drives $\mathrm{PI3K}$, $\mathrm{PIP_3}$ and $\mathrm{PDK1}$ close to zero and substantially reduces $\mathrm{mTORC2}$ as shown by Eqs. (3.2.70)-(3.2.74) and (3.2.75). So $\mathrm{Ser473}$ and $\mathrm{Thr308Akt}$ phosphorylation are inhibited [125].

- *Pten knockout.* When the concentration of PTEN vanishes, as in PtenKO cells, $\mathrm{PIP_3}$, and thus $\mathrm{PDK1}$, $\mathrm{mTORC2}$, and Akt signalling are enhanced [123]. In the model, Pten knockout is simulated by reducing the variable $PTEN_n$ in Eq. (3.2.104). An increase in $\mathrm{pAkt(Ser473)}$ (2.1-fold) and $\mathrm{pAkt(Thr308)}$ (3.2-fold) in PtenKO β-cell of mice compared with control is reported in [130].

- *PDK1 knockout and inhibition.* Hashimoto et al. in [131] showed that PDK1 ablation in mice β-cells reduced Thr308 Akt phosphorylation without affecting the phosphorylation at Ser473. PDK1 knockout effect is reproduced by the model by setting b_{PDK1} close to zero. It has been shown [132] that the protein kinase inhibitor 7-Hydroxystaurosporine (UCN-01), a PDK1 inhibitor [133] used in cancer therapies, had a similar effect on Akt activation: UCN-01 inhibits pAkt(Thr308), and then the GLUT4 translocation to the cellular membrane, in a dose-dependent manner at all insulin concentrations even in the face of almost an completely unaffected Ser473 phosphorylation. Figure 4.13 shows how the model proposed is able to reproduce such effects, i.e. the marked decrease of $\mathrm{Akt_n^T}$ and $\mathrm{Akt_n^{T,S}}$, with the resulting insulin resistance elicited by the drug in treated cells compared to control($\mathrm{GLUT4_{pm}}$ increase of 61.8% in control and 36.7% in treated cells).

- *Rictor knockout.* Muscle extracts from mice with muscle-specific rictorKO showed an impaired Ser473 Akt phosphorylation (85% reduc-

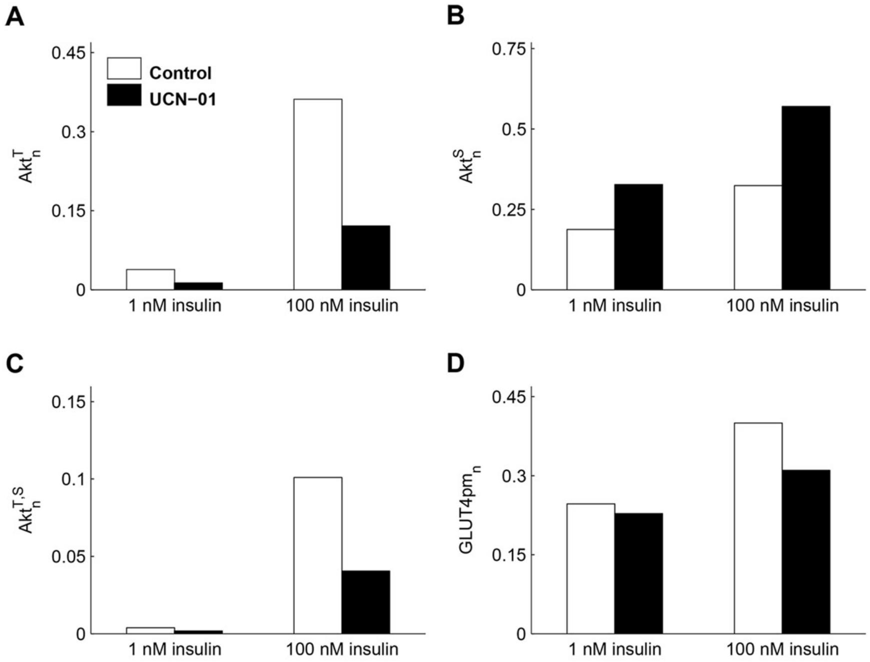

Figure 4.13: Response of the insulin signaling network to the PDK1 inhibitor UCN-01 in L6 cells. Model predictions of $\mathrm{Akt}_\mathrm{n}^\mathrm{T}$, $\mathrm{Akt}_\mathrm{n}^\mathrm{S}$, $\mathrm{Akt}_\mathrm{n}^\mathrm{S,T}$ and $\mathrm{GLUT4}_\mathrm{pm}$ at 1 and 100 nM insulin in control (white boxes) and in cells exposed to UCN-01 (black boxes). To simulate the effect of UCN-01, the parameter a_9 (function of the PDK1 catalytic constant k_{9c}) in (3.2.105) was tenfold decreased, keeping the other parameters to values estimated for L6 cells.

tion) and an increased basal but almost normal Thr308 Akt phosphorylation (similarly for pS6K1(Thr389)) upon insulin stimulation. Thr642 AS160 phosphorylation was reduced but mice did not differ in the insulin tolerance test and only partially in the glucose tolerance test [122]. Accordingly, Eqs. (3.2.78)-(3.2.80) and (3.2.92) show that, if $mTORC2$ is driven close to zero by setting $b_{mTORC2} \cong 0$, pAkt (Ser473) is inhibited, while $\mathrm{Akt}^{\mathrm{T}}$ and $\mathrm{GLUT4}_{\mathrm{pm}}$ may respond almost normally to insulin stimulation.

- *mTOR inhibitors.* mTORC1 signalling is inhibited by rapamycin that inhibits Ser2481 mTORC1 and thus Thr389 S6K1 phosphorylation [134]. Rapamycin action on mTORC1 is represented by reducing the catalytic constant k_{24c} and thus a_{24} in Eq. (3.2.112). Althougth rapamycin cannot bind to preformed mTORC2 [62], it may bind to free mTOR. Therefore, the newly synthesized mTOR does not bind to rictor and mTORC2 assembly is partially or completely inhibited [63]. It has been found, indeed, that long-term rapamycin treatment may cause a strong or a partial inhibition of Ser473 Akt phosphorylation [63]. The response of mTORC2 to long-term rapamycin treatment can be represented by decreasing the model parameters containing the synthesis rate b_{mTORC2}, i.e. the parameters $a^{\epsilon}_{15}, a^{\epsilon}_{19}, a^{\gamma}_{19}$. Figure 4.14 shows the simulation results that are qualitatively in agreement with the experimental data of cells highly sensitive to rapamycin (for instance, the PC3 cells) reported in [63]. A different mTOR inhibitor is PP242 that reduces both mTOR complexes. In the model, PP242 action is represented by a reduction of a_{24} for mTORC1 and a_{10}, a_{11} for mTORC2 [125].

In conclusion, the proposed model appears to be appropriate to quantitatively asses the role of the proteins that are key regulators of the insulin signaling network. It may be useful to better identify the network reactions that are critical for the transitions of cellular states from normal to disease scenario and to give a contribution in the design of anti-diabetic drugs. Indeed, if a drug is targeting a particular enzyme in our network system, the present model allows to envisage its effects on the substrate cascade.

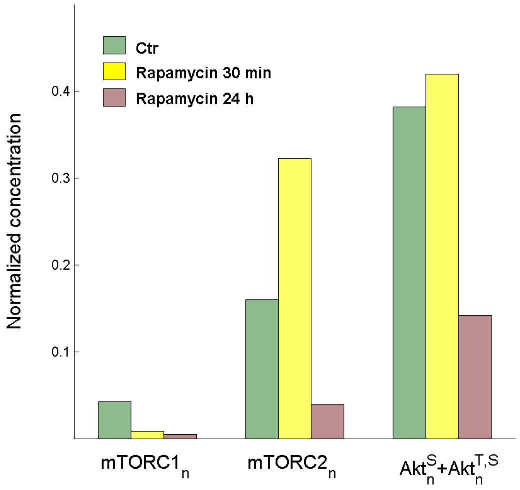

Figure 4.14: Response to short-term and long-term rapamycin treatment of mTORC1, mTORC2, and pAkt (Ser473). Model predictions of mTORC1, mTORC2, and pAkt (Ser473) in control (green boxes) and after short-term (yellow boxes) and long-term (pink boxes) rapamycin treatment at 10 nM insulin. Short- and long-term treatments: a_{24} in Eq. (3.2.112) set to 0.1 of control. Long-term treatment: parameters $a^{\epsilon}_{15}, a^{\epsilon}_{19}, a^{\gamma}_{19}$ of Akt in Eqs. (3.2.107)-(3.2.109) set to 0.1 of control. The other parameters are set to the values estimated for L6 cells. Compared to control, short-term treatment inhibits mTORC1, but enhances mTORC2 due to the downregulation of negative feedback. By contrast, the prolonged treatment strongly inhibits mTORC2 because rapamycin binds to newly synthesized mTOR and the formation of mTOR complex is prevented. mTORC2 inhibition causes a decrement of S473 Akt as well as of double Akt phosphorylation and, as a consequence, also mTORC1 is further downregulated.

Chapter 5

Link between the ISN and the cell proliferation: response to mTOR inhibitors with antitumor activity

The insulin signaling network interacts with other biochemical networks to regulate various physiological and cellular processes. Nowadays, a major goal of biochemical simulations involves integrating outputs of distinct signaling networks to study cell functional outcomes such as proliferation, polarization of cells, or migration. With this aim, in the present chapter we focus on the link that exists between the ISN and the cell proliferation. Indeed, it is widely recognized in literature that Akt and the two mTOR complexes have a major role also in the regulation of the cell growth, and then in cancer development [5, 15, 9]. Moreover, S6K1 is involved in the regulation of protein synthesis and the growth of cell size, and FoxO1 in the induction of apoptosis and autophagy [135].

We investigated how the components of ISN, and in particular Akt and its substrates, may influence the progression of the cells in the cell cycle. In order to correlate these two cellular processes, we considered the response of the ISN and of a AML (acute myeloid leukemia) cell population to mTOR inhibitors with antitumor activity, i.e. the dual ATP-competitive mTOR inhibitor AZD8055 ([65, 136]). The cell population response was represented by the mathematical model, described in the next section, which is similar to the model proposed in [137] and the final goal was to correlate parameters describing tumour cell proliferation with the response to AZD8055 of the ISN.

5.1 The eukaryotic cell cycle

The eukaryotic cell cycle is generally divided into four discrete phases shown in Figure 5.1 [138]: 1) a first phase G_1 (gap 1) in which the cell is metabolically active and continuously grows but does not replicate its DNA; 2) the S phase (synthesis), during which DNA replication takes place; 3) the G_2 phase (gap 2), during which cell growth continues and proteins are synthesized in preparation for mitosis; and 4) the mitosis (M) corresponding to the separation of daughter chromosomes (nuclear division) and usually ending with cell division (cytokinesis) [138]. Moreover, some kinds of cells are characterized by also a quiescent stage of the cycle called G_0, where they remain metabolically active but no longer proliferate unless called on to do so by appropriate extracellular signals. Mitosis is the most dramatic stage of the cell cycle and lasts only about an hour, so approximately 95% of the cell cycle is spent in interphase (the period between mitoses). The cell grows at a steady rate throughout interphase but the duration of every cell cycle phase can vary considerably among different kinds of cells.

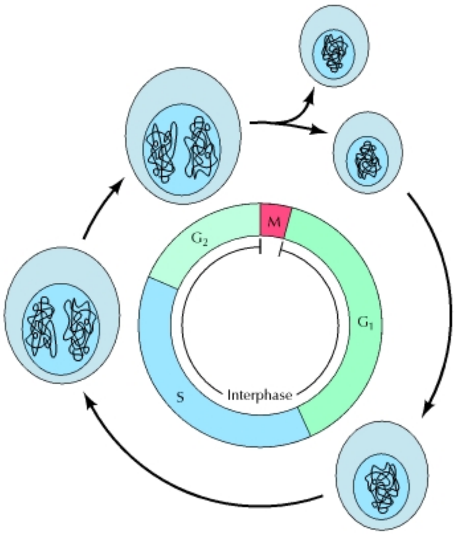

Figure 5.1: Phases of the eukaryotic cell cycle. Figure replotted from [138] that represents the four main phases of the eukaryotic cell cycle: G_1, S, G_2 and M. The relative lengths of the cell cycle phases shown here are typical of rapidly replicating mammalian cells.

Progression through the stages of the cell cycle is controlled by a regulatory apparatus, which not only coordinates the different events so that they occur in the appropriate order but also gets extracellular signals that control cell proliferation. It is critically important that cell entries into the next phase if and only if the events of the preceding phase have been completed. For example, if the mitotis starts when replication of the genome has not been completed, some mutations could appear. Several cell cycle checkpoints exist to ensure that incomplete or damaged chromosomes are not replicated and passed on to daughter cells. One of the most clearly defined of these checkpoints occurs in G_2 and prevents the initiation of M phase before completion of S phase, so cells remain in G_2 until the genome has been completely replicated. This G_2 checkpoint senses unreplicated DNA, which generates a signal that leads to cell cycle arrest. The cell cycle is also arrested at the G_2 checkpoint in response to DNA damage in order to allow the damage repair. DNA damage arrests the cell cycle in another important checkpoint, the checkpoint in G_1, that allow to repair the damage before the cell enters S phase, where the damaged DNA would be replicated. A further important cell cycle checkpoint exists the end of mitosis monitoring the alignment of chromosomes on the mitotic spindle, thus ensuring that a complete set of chromosomes is distributed accurately to the daughter cells.

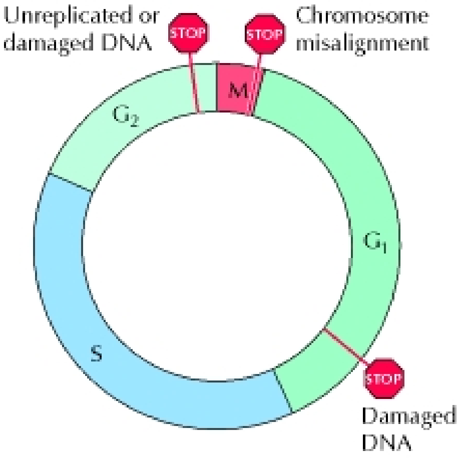

Figure 5.2: Cell cycle checkpoints. Figure replotted from [138] that represents the most clearly defined checkpoints of cell cycle.

To analyse the progression in the cell cycle, it is necessary to identify the cells at the different stages discussed above. Mitotic cells can be distinguished microscopically, while cells in other phases (G_0/G_1, S, and G_2) must be identified by biochemical criteria. For example, cells in S phase can be readily identified by means of the radioactive [^{3}H]thymidine incorporation, which is used exclusively for DNA synthesis [139]. Indeed, it is generally known that, once cells begin DNA replication, they progress without interruption through S phase and incorporate added [^{3}H]thymidine into their newly synthesized DNA. After a short period of exposure, the cells are analyzed by autoradiography and the cell fraction that is found to be radioactively labeled corresponds to the fraction of cells in S phase. Such fraction of labeled cells upon autoradiography is defined as *Labeling Index (LI)* and it is used to estimate the size of the S-phase compartment in various tumors. Obviously, this assay requires the assumption that [^{3}H]thymidine is incorporated by all S-phase tumor cells. Variations of such cell labeling experiments can also be used to determine the length of the other phases of the cell cycle. Let us suppose that the cells are exposed for a short period of time (for instance 15 minutes) to radioactive thymidine, after which the radioactive substance is removed. The radioactively labeled cells that were in S phase during the time of exposure will be observed for several hours as they progress through the remainder of S and G_2. In contrast, radioactively labeled mitotic cells will not be observed until 4 hours after labeling. This 4-hour lag time corresponds to the average length of G_2 (the minimum time required for a cell that incorporated radioactive thymidine at the end of S phase to enter mitosis).

Cells at different phases of the cell cycle can also be distinguished by their DNA content. Animal cells in G_1 contains two copies of each chromosome (diploid), so, if we indicate by n the haploid DNA content of the genome, the DNA content of G_1 cells is 2n. During the S phase, because of the DNA replication, the genome content doubles so that cells in S have DNA contents ranging from 2n to 4n. DNA content remains at 4n for cells in G_2 and M, decreasing to 2n after cytokinesis. Experimentally, cellular DNA content can be determined by incubation of cells with a fluorescent dye that binds to DNA, followed by analysis of the fluorescence intensity of individual cells in a flow cytometer or a fluorescence-activated cell sorter, thereby distinguishing cells in the G_1, S, and G_2/M phases of the cell cycle.

5.2 The mathematical model of the cell proliferation

To analyze the behavior of the AML cell population in the presence of the dual ATP-competitive mTOR inhibitor AZD8055, we used a mathematical model of cell cycle based on the age formalism, similar to that proposed in

[137] and represented by the block diagram of Figure 5.3.

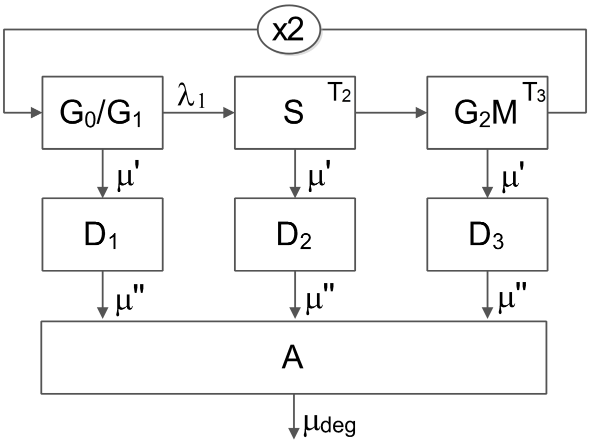

Figure 5.3: Scheme of the mathematical model used for the analysis of AML cell population data in the absence and presence of AZD8055. The blocks represent G_0/G_1, S and G_2M cells, with the X2 block denoting binary cell division. λ_1 is the rate constant of $G_1 \rightarrow S$ transition, T_2 and T_3 the transit times in S and G_2M phases, and $\mu^{'}$ the rate constant of cell loss. $D_1 - D_3$ represent cells lost from viable compartments but still measurable, and A the apoptotic bodies and fragments, with $\mu^{''}$ the rate constant of cell fragmentation and μ_{deg} the loss rate constant from A.

We considered three main phases (G_0/G_1, S and G_2M) and assumed that the cell transition into the G_0/G_1 phase is random with an exponential distribution and rate constant λ_1, while the S and G_2M phases are deterministic with transit times denoted by T_2 and T_3, respectively. Cells may be randomly lost from G_0/G_1, S and G_2M with the same rate constant $\mu^{'}$ (cell loss from compartments of viable cells) and enter the compartments D_i, $i = 1, 2, 3$ that contain dead cells but still transiently measurable. Cells exit randomly from D_i, $i = 1, 2, 3$ with the rate constant of cell fragmentation $\mu^{''}$ and enter the compartment A of the apoptotic bodies and fragments. From A, cells exit with the rate constant μ_{deg}.

We observe that, in the simple scheme of cell progression across cell cycle shown in Fig. 5.3, the rate constant λ_1 represents the activity of the cyclins (as cyclin D) and the cyclin-dependent kinases that regulate the G_1 to S transition. The rate constant $\mu^{'}$ may be related to the activity of the proteins that regulate the autophagia and/or the early phases of apoptosis, whereas $\mu^{''}$ may be related to late apoptosis.

Denoting by $N_1(t)$ the number of G_0/G_1 cells at time t, and by $n_i(a_i, t)$, with $i = 2, 3$, the cell density at time t with respect to age a_i for cells in S and

G$_2$M phases (a_i is measured from cell entry into the corresponding phase), we have the balance equations

$$\frac{dN_1(t)}{dt} = -(\lambda_1 + \mu^{'})N_1(t) + 2n_3(T_3, t) \tag{5.2.1}$$

$$\frac{\partial n_i(a_i, t)}{\partial t} + \frac{\partial n_i(a_i, t)}{\partial a_i} = -\mu^{'} n_i(a_i, t), \quad i = 2, 3, \tag{5.2.2}$$

with boundary conditions

$$n_2(0, t) = \lambda_1 N_1(t)\,, \qquad n_3(0, t) = n_2(T_2, t)\,. \tag{5.2.3}$$

The number of S-phase cells at time t is given by

$$N_2(t) = \int_0^{T_2} n_2(a_2, t) da_2\,, \tag{5.2.4}$$

and similarly, for the number of G2M-phase cells, we have

$$N_3(t) = \int_0^{T_3} n_3(a_3, t) da_3\,. \tag{5.2.5}$$

Moreover, denoting the number of cells lost from the three viable compartments by $D_i(t), i = 1, 2, 3$, we have

$$\frac{dD_i(t)}{dt} = -\mu^{''} D_i(t) + \mu^{'} N_i \tag{5.2.6}$$

Apoptotic bodies and fragments are eventually gathered in a further compartment that obeys the equation

$$\frac{dA(t)}{dt} = -\mu_{deg} A(t) + \mu^{''}\big(D_1(t) + D_2(t) + D_3(t)\big) \tag{5.2.7}$$

where the material that leaves this compartment with rate constant μ_{deg} is no longer measurable.

Assuming that the cell population is in balanced exponential growth (or is declining under the treatment) with rate constant α, it is:

$$N_1(t) = \bar{N}_1 e^{\alpha t}\,, \tag{5.2.8}$$

$$n_i(a_i, t) = \bar{n}_i e^{-\beta a_i} e^{\alpha t} \qquad i = 2,\, 3 \tag{5.2.9}$$

where $\bar{N}_1$, $\bar{n}_i$, with $i = 2, 3$, represent the initial conditions and $\beta = \alpha +$

μ'. Moreover, in exponential growth,the following relation among the model parameters can be obtained:

$$\alpha + \mu' + \lambda_1 = 2\lambda_1 e^{-(\alpha+\mu')(T_2+T_3)} \tag{5.2.10}$$

From (5.2.1)-(5.2.9), the fractions of cells in the cell cycle phases and in the apoptotic compartment at the generic time t can be obtained. Since, as in [137], we assumed that cells lost from the viable population can still be transiently measurable, the fractions of cells in the cell cycle phases measured by propidium iodide (PI) staining and flow cytometry (see next section), must be derived accounting for the dead cells in compartments $D_i(t), i = 1, 2, 3$, together with the viable cells in the respective phase. So, f_{G1} is computed as $(N_1 + D_1)/N_{tot}$ and, similary, $f_S = (N_2 + D_2)/N_{tot}$ and $f_{G2M} = (N_3 + D_3)/N_{tot}$, with N_{tot} the total amount of cells and fragments. It is easy to verify that:

$$f_{G1} = \frac{(\alpha+\mu')(\alpha+\mu_{deg})(\alpha+\mu'+\mu'')}{\Big(\alpha+\mu'+\lambda_1\big(1-e^{-(\alpha+\mu')(T_2+T_3)}\big)\Big)\Big(\mu'\mu''+(\alpha+\mu_{deg})(\alpha+\mu'+\mu'')\Big)}, \tag{5.2.11}$$

$$f_S = \frac{\lambda_1(1-e^{-(\alpha+\mu')T_2})(\alpha+\mu_{deg})(\alpha+\mu'+\mu'')}{\Big(\alpha+\mu'+\lambda_1\big(1-e^{-(\alpha+\mu')(T_2+T_3)}\big)\Big)\Big(\mu'\mu''+(\alpha+\mu_{deg})(\alpha+\mu'+\mu'')\Big)}, \tag{5.2.12}$$

$$f_{G2M} = \frac{\lambda_1 e^{-(\alpha+\mu')T_2}(1-e^{-(\alpha+\mu')T_3})(\alpha+\mu_{deg})(\alpha+\mu'+\mu'')}{\Big(\alpha+\mu'+\lambda_1\big(1-e^{-(\alpha+\mu')(T_2+T_3)}\big)\Big)\Big(\mu'\mu''+(\alpha+\mu_{deg})(\alpha+\mu'+\mu'')\Big)}. \tag{5.2.13}$$

Obviously, the fraction of apoptotic materials is given by

$$f_A = 1 - f_{G1} - f_S - f_{G2M}\,. \tag{5.2.14}$$

In addition, the total fraction of dead cells and fragments can be computed as:

$$f_{Dead} = f_A + \sum_{i=1}^{3} f_{Di} = \frac{\mu'(\alpha+\mu_{deg}+\mu')}{\mu'\mu''+(\alpha+\mu_{deg})(\alpha+\mu'+\mu'')}, \tag{5.2.15}$$

with f_{Di} the cell fraction in the respective compartment $\mathrm{D_i}$.

To assess the effect of the drug on cell cycle progression, as discussed in the next sections, we used data of labeling index (LI) accounting for the radioactive [^{3}H]thymidine incorporation. So, in order to estimate the parameters of the cell proliferation model, we had to derive the LI expression from the model equations. As in [137], for simplicity, the labeling process was accounted for by assuming that cells were exposed to a rectangular [^{3}H]thymidine pulse of length Δ. The pulse length Δ was taken to be shorter that the $\mathrm{G_2M}$ transit time. Moreover, we assumed that even a sojourn of infinitesimal duration in S during the pulse suffices for a cell to be labeled. Thus, letting time t be counted from the start of the [^{3}H]thymidine injection, at $t = 0^+$ all S-phase cells are labeled; at $t = \Delta$, all cells in S, plus the $\mathrm{G_2M}$ cells with age a_3 between 0 and Δ, are labeled. With these assumptions [137], we found that:

$$\begin{aligned} \mathrm{LI}(\Delta) = f_{G1}\frac{\lambda_1(\alpha+\mu^{''})}{(\alpha+\mu^{'})(\alpha+\mu^{'}+\mu^{''})}&\left[e^{\alpha\Delta}\left(1-e^{-(\alpha+\mu^{'})(T_2+\Delta)}\right)\right. \\ &\left.+\mu^{'}e^{-\mu^{''}\Delta}\left(\frac{(e^{(\alpha+\mu^{''})\Delta}-1)}{\alpha+\mu^{''}}-\frac{e^{-(\alpha+\mu^{'})T_2}(e^{(\mu^{'}-\mu^{''})\Delta}-1)}{\mu^{'}-\mu^{''}}\right)\right]. \end{aligned} \quad (5.2.16)$$

5.3 Model parameter estimation from data of AML cells

We estimated the unknown parameters $\alpha, \lambda_1, T_2, T_3, \mu^{'}, \mu^{''}$ and μ_{deg} of the model shown in Fig. 5.3 for an AML cell population model both in the absence and presence of the dual ATP-competitive mTOR inhibitor AZD8055. Note that Eq. (5.2.10) is an independent relationship among parameters that actually reduces the number of unknowns. For instance, we derived λ_1 as function of the remaining parameters. Moreover, while $\alpha, \lambda_1, T_2, T_3, \mu^{'}, \mu^{''}$ are expected to be different in the control (absence of AZD8055) and in the populations treated with different drug doses, it is likely that μ_{deg} does not change and, for simplicity, was taken equal to the value of $\mu^{''}$ in the control.

For the parameter estimation we used the experimental data reported in [136]. The Authors reported the fractions of cells in the cell cycle phases and the fraction of the apoptotic fragments obtained by propidium iodide (PI) staining and flow cytometry (Figure 5.4), the data of [^{3}H]thymidine incorporation (Figure 5.5) and the fractions of annexin V and PI-positive

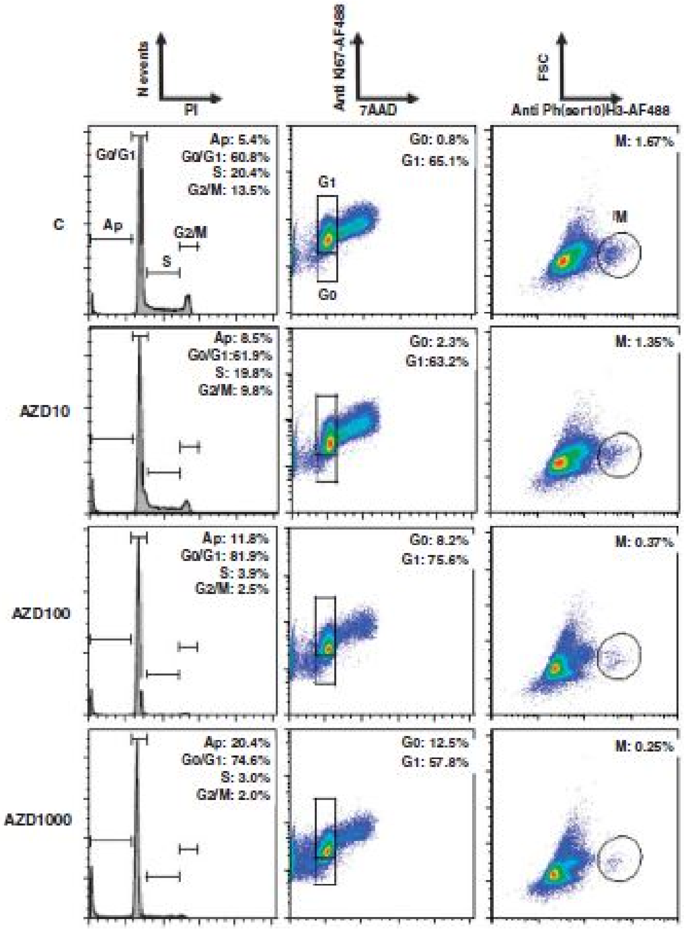

Figure 5.4: Data on cell cycle progression in AML obtained by propidium iodide (PI) staining and flow cytometry. Figure replotted from [136] showing how AZD8055 decreases cell proliferation and cell cycle progression in AML.

cells (Figure 5.6) at increasing AZD8055 concentrations. The in vivo effect of the drug in mice bearing MV4-11 xenografts is also shown (Figure 5.7).

The growth rate constant α of the untreated population was obtained from the growth curve of tumor size in the xenograft (black curve in Fig. 5.7), which is approximately exponential, and we assumed that a similar value holds for the MV4-11 cell line. From the data of cell fractions in cell-cycle phases given by flow cytometry and the data of PI-positive cell fraction represented by the quantity f_{Dead} in Eq. (5.2.15), we estimated $\lambda_1, T_2, T_3, \mu', \mu''$ by least squares method using (5.2.10)-(5.2.15). Equation (5.2.16) provided the value of the labeling index in control, not given in [136]. Such value was computed with the labeling period $\Delta = 6$hrs [136].

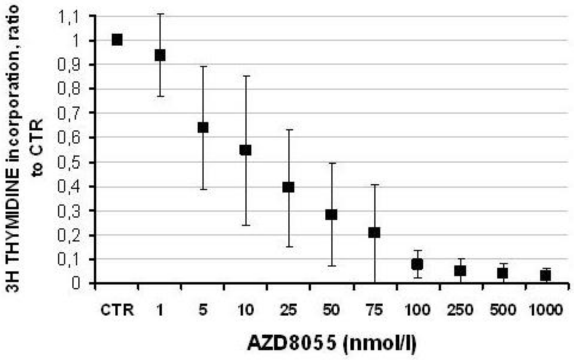

Figure 5.5: Data on thymidine incorporation at increasing AZD8055 concentrations. Figure replotted from [136] showing $[^3H]$thymidine incorporation (labeling index, LI) of AML cells with and without AZD8055. Results are expressed as a ratio between each condition and the control condition.

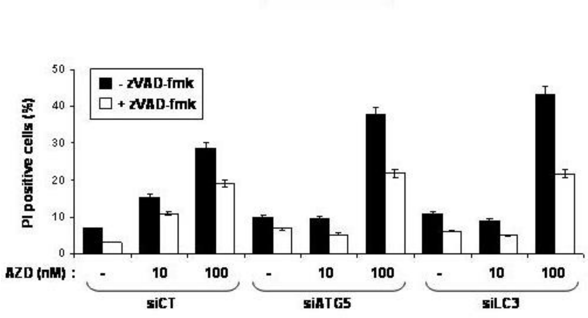

Figure 5.6: Fractions of annexin V and PI-positive cells. Figures replotted from [136] showing fractions of annexin V (upper panel) and PI-positive (lower panel) cells at different experimental conditions.

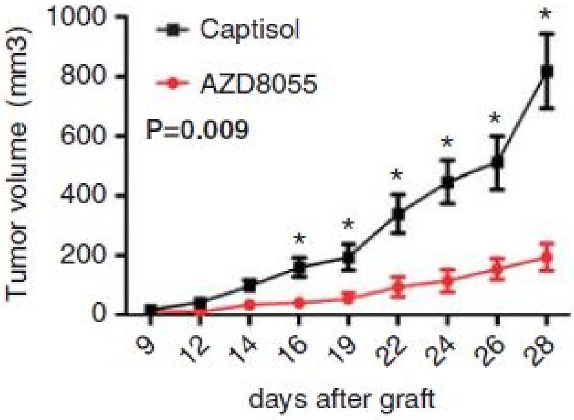

Figure 5.7: In vivo effects of AZD8055 in nude mice transplanted with MV4-11. In [136] MV4-11 cells were xenografted in nude mice treated with captisol (black) or with 20mg/kg/day AZD8055 (red) and tumor size was evaluated some days after graft.

For treated cells, the rate constant α was not available and the drug dose of 20 mg/kg/day AZD8055 administered to mice could not be reliably converted to a drug concentration in the culture medium. The LI values of treated populations, expressed in Fig. 5.2.16 as ratios treated/control, were multiplied for the LI of control (31.2%) in order to obtain the actual values to be compared with the model-predicted LI.

Table 5.1 reports the parameter estimates for the untreated cells and at increasing drug concentrations (10, 100 and 1000 nM).

	$\alpha\,(hr^{-1})$	$\mu'\,(hr^{-1})$	$\mu''\,(hr^{-1})$	$T_2\,(hr)$	$T_3\,(hr)$	$\lambda_1\,(hr^{-1})$
Control	$7.43 \cdot 10^{-3}$	$8.52 \cdot 10^{-3}$	$1.81 \cdot 10^{-1}$	10.61	8.73	$3.4 \cdot 10^{-2}$
AZD 10 nM	$-1.42 \cdot 10^{-2}$	$1.62 \cdot 10^{-2}$	$1.98 \cdot 10^{-1}$	87.82	52.89	$3.82 \cdot 10^{-2}$
AZD 100 nM	$-2.12 \cdot 10^{-2}$	$2.16 \cdot 10^{-2}$	$1.1 \cdot 10^{-1}$	97.91	72.6	$4.56 \cdot 10^{-4}$
AZD 1000 nM	$-3.69 \cdot 10^{-2}$	$3.72 \cdot 10^{-2}$	$8.8 \cdot 10^{-2}$	97.16	77.07	$3.81 \cdot 10^{-4}$

Table 5.1: Estimates of parameters of the cell population model in control and in cells exposed to 10, 100, and 1000 nM AZD8055.

Figure 5.8 displays the data of cell fractions in cell cycle phases and the model fitting. The same figure also displays data and model predictions of

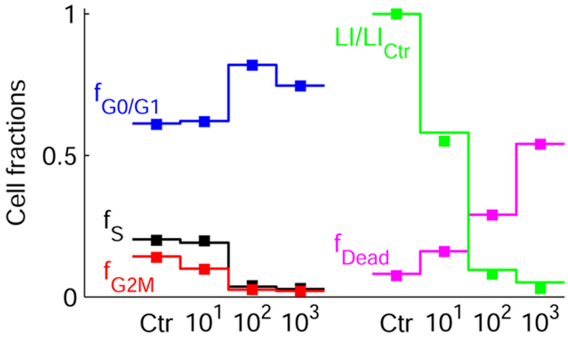

Figure 5.8: Data of AML cells used for the parameter estimation and the model fitting. Data of cell fractions in cell cycle phases in control and cells treated with 10, 100, and 1000 nM AZD8055 (closed squares), and model fitting (solid lines). The panel also displays data and model fitting of LI normalized to control, and of total fraction of dead cells and fragments.

labeling index and of the total fraction of dead cells and fragments. Note the cell accumulation in G_0/G_1 and the depletion of S and G_2M phases in the treated populations. The rate constant λ_1 of the transition from G_0/G_1 to S exhibits a marked concentration-dependent decrement, whereas the transit times in S and G_2M, and the loss rate constant μ' from the viable compartment, increase (see Table 5.1). Accordingly, α (population doubling time $ln2/\alpha = 3.860$ days in control) turns out to be negative in treated populations (halving times $2.036, 1.364$, and 0.783 days at $10, 100$, and $1000nM$ AZD8055). These results confirm that a major factor that inhibits cell proliferation is the block of cells in the G_0/G_1 phase [51].

There is an intricate interplay between autophagia and apoptosis, and these modes of cell death may antagonize or cooperate [140]. We did not try to represent these pathways, hence the simple model used for the analysis of data cannot allow to unambiguously relate the parameters μ' and μ'' to autophagia or apoptosis. The present model, indeed, represents cell death as a two−stage process and α depends directly on μ' but not on μ'' as shown by (5.2.10). However, as depicted by Fig. 5.9, we note that the fraction of dead cells $\sum_{i=1}^{3} f_{Di}$ nicely correlates with the increase of acridine orange staining (an indicator of autophagy) reported in [65] for a different cell line, so the parameter μ' might mainly be related to cell death caused by autophagia.

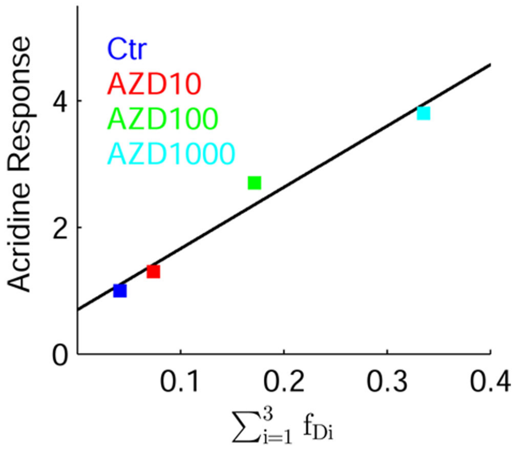

Figure 5.9: Correlation between data of acridine orange staining in A549 cells and fraction of dead cells. We found that the data of acridine orange staining reported in [65] and the fraction of dead cells $\sum_{i=1}^{3} f_{Di}$ correlate linearly at increasing concentrations of AZD8055.

5.4 Akt/mTOR signaling and cell proliferation

The last step to investigate how the insulin signaling network can influence the progression of the cells in the cell-cycle was to correlate the estimated parameters that describe the kinetics of AML cell population with the response to AZD8055 of the ISN. For this aim, we used the experimental data reported in [136] showing the inhibition of p-70S6K Thr389 in the MV4-11 human AML cell line, in untreated cells and at increasing drug concentrations (10, 100 and 1000 nM). These data are replotted from [136] in Fig. 5.10.

In order to fit the pS6K1 (Thr389) inhibition profile in the MV4-11 human AML cell line in [136], the parameters a_{10}, a_{11}, and a_{24} in Eqs. (3.2.106) and (3.2.112) that regulate the inhibition of mTORC1 and mTORC2 signaling were then estimated, keeping the other parameters to the values estimated for L6 cells (see Table 4.1). We accounted for the constitutive activation of PI3K/Akt signaling, frequently found in AML [141], by representing this activation as an equivalent insulin signal (I_e in Eq. (3.2.97) equals 0.2 nM) that drives $PI3K_n$ from $0.28 \cdot 10^{-2}$ at zero insulin to $0.52 \cdot 10^{-2}$. The fitting results are shown in Fig. 5.11. With the estimated values of the parameters of mTOR complexes, we computed other ISN model outputs at the steady state related to the different drug concentrations.

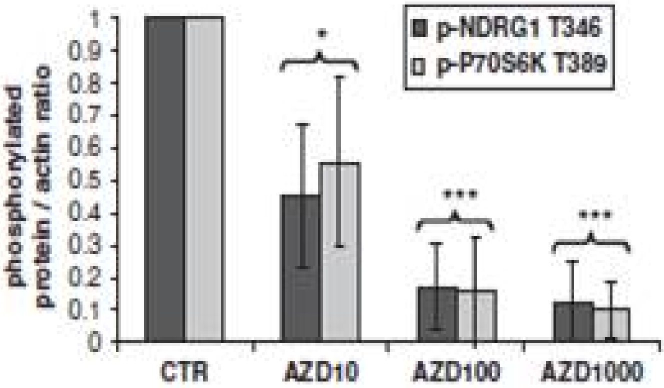

Figure 5.10: The inhibition of p-70S6K Thr389 and p-NDRG1 Thr346 in the MV4-11 human AML cell line with increasing AZD8055 concentrations Data replotted from [136] showing the inhibition of p-70S6K Thr389 and p-NDRG1 Thr346 in the MV4-11 human AML cell line with increasing AZD8055 concentrations. Results are expressedas a ratio to the control incubation without AZD8055.

Figure 5.12 highlights the simple relationships found between the model-predicted changes in the concentrations of ISN proteins, induced by mTOR inhibition, and the changes in the AML cell population model parameters, which correspond to alterations of the proliferative capacity of the population. In particular, a simple non linear function provided a good fit of the relation between pAkt (Ser473), predicted by insulin signaling model, and the population model parameter λ_1 (panel A of Figure 5.12), showing how these two quantities decrease when the drug concentration increases and how the extent of the block of $\text{G1} \rightarrow \text{S}$ transition is related to mTORC2 inhibition. Similar functions also fit the relations between λ_1 and pGSK3β(Ser9), cytosolic FoxO1 and pS6K1(Thr389) (Figure 5.12 panels A and B).

Panel C of Figure 5.12 depicts the relationship between the average cell cycle time, an index of the rate of protein synthesis obtained from the cell population model, and pS6K1(Thr389). The average cell cycle time is an index of the rate of protein synthesis and it is computed as sum of $1/\lambda_1, T_2$ and T_3. In panel D, the model predicted pS6K1(Thr389) is plotted versus the loss parameter $\mu^{'}$, showing how mTORC1 inhibition is also related with the increment of cell loss from the compartment of viable cells. The above findings agree with the notion that mTORC2 inhibition activates cyclins D1-D2 via Akt (Ser473) and FoxO1 inhibition, and that mTORC1 inhibition activates autophagy via ULK1/ATG13 inhibition [5]. Rapamycin derivatives

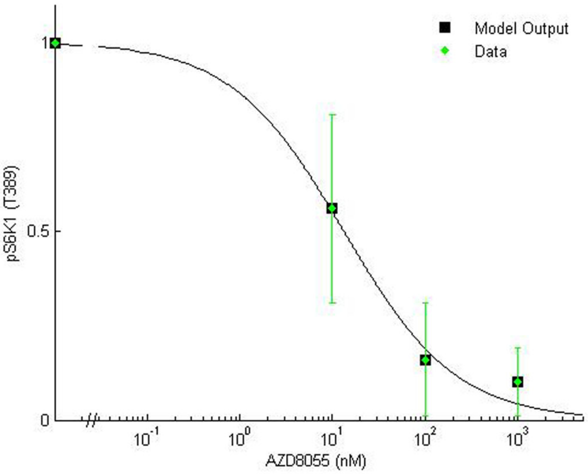

Figure 5.11: pS6K1 (Thr389) vs AZD8055 concentration. Normalized data (mean ± SD) of pS6K1 (Thr389) vs AZD8055 concentration (green diamonds) replotted from [136] and model outputs (black squares), together with the fitting line $y = 6.35/(6.34 + x^{0.71})$.

have indeed been found that inhibit both mTOR complexes and decrease the levels of CCND1 and CCND2 in AML [142].

In summary, we proved that the proposed ISN model permits to investigate the insulin signaling network in the insulin resistance states and in cancer, focusing on the role played by Akt phosphorylated at Ser473 and by the mTOR complexes, as well as on the drug effects. However, although it would be tempting to use the found relations to couple the two mathematical models, it is worth noting that we have used data obtained in a particular experimental setting, so these relations are likely to be not valid in different settings. The relations found are a rough representation of the complex machinery that regulates cell cycle progression, entry and exit from quiescence, and occurrence of cell death. Indeed, we found relationships between the rate constant λ_1 of the G1 to S transition and different proteins (pAkt (Ser473), pGSK3β(Ser9), FoxO1 and pS6K1(Thr389)), but the molecular pathways that link and coordinate the action of these proteins in cell cycle regulation remain undetermined. Similarly, pS6K1(Thr389) is related to parameters of cell cycle progression and cell death, but its specific role in these pathways is not specified. The cell population model of Fig. 5.3 is very far from the complexity and richness of behaviors that can be exhibited by the real system. Sophisticated models have been proposed to represent

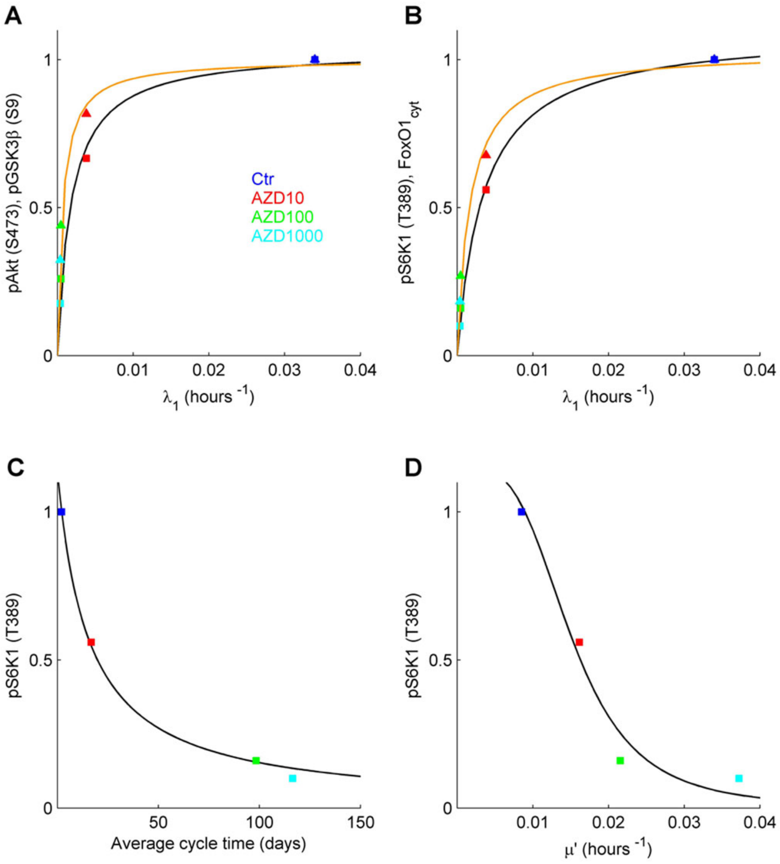

Figure 5.12: ISN response to the mTOR inhibitor AZD8055. (A) Relationship between the decrease of pAkt(Ser473) (squares) and that of λ_1 at increasing drug concentrations. The fitting line (black line) is given by $y = 1.03x/(0.18 \cdot 10^{-2} + x)$, with y=pAkt(Ser473) and x $=\lambda_1$. A similar function (orange line) fits the relation between GSK3β(Ser9) (triangles) and λ_1. (B)Relationship between the decrease of pS6K1 (Thr389) (squares) and that λ_1 at increasing concentrations of the drug. The fitting line (black line) has equation $y = 1.10x/(0.35 \cdot 10^{-2} + x)$, with y= pS6K1 (Thr389) and x=λ_1. A similar function (orange line) fits the relation between FoxO1cyt (triangles) and λ_1. (C) Decrease of pS6K1(Thr389) with drug concentration and relation with the average cell cycle time predicted by the cell population model. The fitting line is $y = 17.71/(15.61 + x)$. (D) Decrease of pS6K1(Thr389) with the drug concentration and relation with the parameter $\mu^{'}$ predicted by cell population model. Fitting line is $y = (3.63 \cdot 10^{-7})/(3.15 \cdot 10^{-7} + x^{3.57})$. In each panel data are normalized to control and represented for the different drug concentrations with the color code: control (blue), AZD10 (red), AZD100 (green), AZD1000 (cyan).

the reactions involving the cyclins and the cyclin-dependent kinases, see for instance a complex model proposed for cell cycle control in mammalian cells [143]. It must also be noticed that we have considered the steady-state response to a drug of the insulin signaling network and the response of the in vitro AML cell population. Studying the in vivo response would be much harder, as the drug pharmacokinetics and the transport into cells must be accounted for, together with the transient response of the protein network and the pharmacodynamics of the drug [65].

Conclusions

In the present PhD thesis, a detailed mathematical model of the insulin signlaing network (ISN) was proposed and used to analyze two different data sets of skeletal muscle cells available in the literature. The first data set included experimental data of L6 myotubes with induced insulin resistance [13] whereas the second one consisted of data of C2C12 myoblasts with PTEN protein suppressed [123].

We used the proposed model to investigate the basal concentrations and the dose-response curves of the main known components of the ISN and to identify the players having a key role in the insulin-stimulated uptake of glucose into the cells. A detailed analysis of the regulatory processes constituting ISN may permit to develop new insights about the origin of the pathologies related to dysfunctions of the ISN and to find drugs able to counterbalance the effect of these diseases.

The most widespread pathology caused by ISN malfunctioning is the insulin resistance, which is the common denominator of several diseases including type 2 diabetes and cancer. Indeed, it is widely recognized that some ISN components have key roles, not only in the glucose metabolism, but also in other important cellular processes such as apoptosis, cell proliferation, transcription and cell migration and they are thus involved also in cancer development. So, investigating the mechanisms responsible for insulin signaling impairment is of primary importance and it is the object of many experimental and theoretical research works. In the last decades, several studies were published on the mechanisms regulating ISN and several research groups proposed mathematical models to represent the complexity of this network.

The ISN scheme here considered is based on a consolidated view that emerges from recent literature [4, 5, 12, 16, 17, 108]. We focused particularly on single and double Akt phosphorylation because recent studies [122] have shown that Akt activity is maintained almost unaltered when it is phosphorylated only on Thr308, while Ser473 phosphorylation seems to play an independent role in both insulin resistance and cancer. That Akt can accomplish its enzymatic function without undergoing Ser473 phosphorylation is demonstrated by the finding that muscle-specific rictor KO mice simply present with a moderately decreased insulin-stimulated glucose uptake and glucose intolerance, but not diabetes. Thr308 Akt phosphorylation is in fact able to activate GLUT4 translocation and it is sufficient to mediate the phosphorylation of GSK3. A scheme where Akt can be independently phosphorylated at Thr308 and Ser473 residues, and where both sites can lead to complete Akt activation, like the one presented in this thesis, does not appear to have previously been considered.

Moreover, in the present model a new characterization of the upstream signaling of mTORC2 is proposed. mTORC2 is assumed to be activated by PIP3, as suggested in [5, 9], and by a putative factor (denoted by J), not dependent on PI3K, which is released by the small intestine and that induces insulin resistance possibly operating through the growth factor receptors [13]. This hypothesis is based on the clinical observation that bariatric surgery, a procedure in which a portion of the stomach and of the small intestine are removed or bypassed, induces a remission of T2D very soon after surgery and far too early to be attributed to weight loss. As bariatric operations reroute food through the upper small intestine, an hypothesis for explaining this mechanism can be that the gastrointestinal removal or bypass reduce the production of putative intestinal factor/s inducing insulin resistance. Such hypothesis was experimentally tested by Salinari et al. [13], showing that L6 cells exposed to a medium enriched with proteins secreted by the small intestine of diabetic rats activated mTORC2, as revealed by an increased value of Ser473 Akt phosphorylation, even in the absence of insulin stimulation.

The model was formulated without including, for simplicity, some established pathways of the network (as for instance, the IR intracellular pool and the receptor recycling) and by describing most of the chemical reactions by the classical Michaelis-Menten scheme. As our aim was the analysis of the dose-response curves, we then derived the concentrations of the chemicals at the equilibrium and, to reduce the number of model parameters to be estimated, we rewrote the model equations in a normalized form.

The model parameters were estimated for both the L6 and C2C12 cells by an ordinary least-squares approach. The proposed ISN model was able to adequately fit all the available experimental data and thus, it can be used as a tool to generate and test hypotheses. The parameter estimates are rather different between C2C12 and L6 cells, but this is not surprising since C2C12 is a line of mouse myoblasts whereas L6 is a line of rat myotubes. In particular, we found that C2C12 cells are more insulin-resistant than L6 cells. Ideed, the value of extracellular insulin at which insulin receptor is half of its maximal was found equal to about 45 nM in C2C12 and about 10 nM in L6 cells. We found also that db/db L6 cells have a value of the factor J substantially larger compared to control (0.07 vs. 0.001) confirming the hypothesis in [13].

In order to identify those parameters that have the greatest impact on the system output, we also performed a sensitivity analysis for both cell lines at the respective optimum. The general pattern of the sensitivities was found to be similar, confirming that the model is able to represent both types of data.

Moreover, the capacity of the proposed model to represent the effects of inhibitors and of conditions such as gene knockout or RNA interference was tested. For instance, we verified that the model is appropriate to study the effect of the UCN-01, a PDK1 inhibitor used in cancer therapies [133]. UCN-01 inhibits Thr308 but not Ser473 Akt phosphorylation and impairs Akt kinase activity with the subsequent inhibition of the GLUT4 translocation to the cellular membrane [132]. The model predictions reported in Figure 4.13 show the marked decrease of pAkt(Thr308), with the resulting insulin resistance elicited by the drug in treated cells compared to control (the concentration of the glucose transporters increases up to 61.8% in control and 36.7% in treated cells). We also simulated the model response to rapamycin treatments and the obtained results (Figure 4.14) are qualitatively in agreement with the experimental data in [63].

Finally, in view of the close and widely recognized relationship between insulin resistance and cancer, we investigated how the components of ISN, and in particular Akt and its substrates, may influence the progression of the cells in the cell cycle. In order to correlate these two cellular processes, we considered the response of the ISN and of a cell population of AML to an mTOR inhibitor with antitumor activity, i.e. the dual ATP-competitive mTOR inhibitor AZD8055. Using literature data of the AML cell population, we found simple relationships between the model-predicted changes in the concentrations of proteins of the ISN, induced by mTOR inhibition, and the changes in the population model parameters which correspond to alterations of the proliferative capacity of the population. In particular, a simple nonlinear monotonic function provides a good fit of the relation between the values of pAkt(Ser473), predicted by the insulin signaling model, and the population model parameter describing the transition from the G_1 to S phases of the cell cycle (see Figure 5.12). These two quantities are even more reduced as the drug concentration increases suggesting that the extent of the block of $\mathrm{G}_1 \rightarrow \mathrm{S}$ transition is related to the mTORC2 inhibition. Moreover, the model-predicted pS6K1(Thr389) was plotted versus the rate constant of cell loss, showing how mTORC1 inhibition is also related with the increment of such loss. Although it would be tempting to use the relations found to couple the two mathematical models, it is worth noting that: 1) such relations are a rough representation of the complex machinery that links and coordinates the action of ISN proteins in cell cycle regulation; 2) we have used data obtained in a particular experimental setting, so these relations are likely to be not valid in different settings; 3) we have considered the steady-state response of the ISN to a drug and the response of the in vitro AML cell population.

In spite of the simplifying assumptions made in view of the ISN complexity, we can conclude that the proposed ISN model, focusing on the role played by Akt and by the mTOR complexes, as well as on the drug effects, permits to investigate the insulin signaling network in the insulin resistance states and in cancer. Although the numerical values of model parameters will certainly change with the cell type, the general structure of the model can be considered valid for any cell type as shown by the qualitative agreement observed between the model predictions and the experimental data from cell types different from skeletal muscle, such as AML cells and PC3 cells. Model behavior has been tested on a variety of conditions: muscle cells with Pten KO or with induced insulin resistance, cells treated with rapamycin, cells with anticancer drugs such as AZD8055 and UCN-01. The proposed model should thus be useful to elucidate the impact of pathologic or therapeutic alterations on the operating states of the network so to support research and development in the field of both diabetes and oncology, and the pharmaceutical industries in the drug design.

Acronyms

ISN	Insulin Signaling Network
PM	Plasma Membrane
T2D	Type 2 Diabetes
T1D	Type 1 Diabetes
OGTT	Oral Glucose Tolerance Test
IVGTT	Intra-Venous Glucose Tolerance Test
MTT	Meal Tolerance Test
EHC	Euglycemic Hyperinsulinemic Clamp
MM	Michaelis-Menten
sQSSA	standard Quasi-Steady-State Approximation
tQSSA	total Quasi-Steady-State Approximation
PDE	partial differential equation
ODE	ordinary differential equation
MLE	Maximum Likelihood Estimator
OLSE	Ordinary Least Squares Estimator
WLSE	Weighted Least Squares Estimator
IR	Insulin Receptor
IGF-1	Insulin-like Growth Factor 1
EGF	Epidermal Growth Factor
SH2	Src-Homology-2
IRS1	Insulin Receptor Substrate-1

PTP1B	Protein Tyrosine Phosphatases 1B
PI3K	Phosphatidylinositide 3-Kinase
PI(3,4,5)P3	Phosphatidylinositol 3,4,5-trishosphates
PTEN	Phosphatase and Tensin Homologue
SHIP2	SH2 domain containing inositol polyphosphate phosphatase
PDK1	Phosphoinositide-dependent Protein Kinase-1
PKC	Protein Kinase C
Akt	RAC-alpha Serine/Threonine-protein Kinase
PKB	Protein Kinase B
PP2A	Protein Phosphatase 2A
PHLPP	PH domain and Leucine rich repeat Protein Phosphatases
FoxO1	Forkhead box protein O1
mTOR	Mammalian Target of Rapamycin
mTORC1	Mammalian Target of Rapamycin Complex 1
mTORC2	Mammalian Target of Rapamycin Complex 2
DEPTOR	DEP domain-containing mTOR-interacting protein
RAPTOR	Regulatory-associated Protein of mTOR
RICTOR	Rapamycin-Insensitive Companion of mTOR
PRAS40	40 kDa Prorich Akt Substrate
GAP	GTPase-Activating Protein
GTP/Rheb	GTPase Ras homologue enriched in brain
TSC1/TSC2	Tuberous Sclerosis Complex 1/2
S6K1	Substrate S6 Kinase 1
4E-BP	4E-Binding Protein
AS160	Akt Substrate of 160 kDa
GSK3β	Glycogen Synthase Kinase 3-β
GYS	Glycogen Synthases

GLUT4	Glucose Transporter-4
2-DG	2-deoxyglucose
CM	Conditioned Medium
AML	Acute Myeloid Leukemia
UCN-01	Protein Kinase Inhibitor 7-Hydroxystaurosporine
LI	Labeling Index

List of Figures

List of Tables

Bibliography

[1] C. Sawyers. Targeted cancer therapy. *Nature*, 432(7015):294–297, 2004.

[2] A.R. Saltiel and C.R. Kahn. Insulin signalling and the regulation of glucose and lipid metabolism. *Nature*, 414(6865):799–806, 2001.

[3] F.S. Thong, C.B. Dugani, and A. Klip. Turning signals on and off: GLUT4 traffic in the insulin-signaling highwayr. *Physiology (Bethesda)*, 20:271–284, 2005.

[4] J. Huang and B.D. Manning. A complex interplay between Akt, TSC2 and the two mTOR complexes. *Biochem Soc Trans*, 37(Pt 1):217–22, 2009.

[5] M. Laplante and D.M. Sabatini. TOR signaling in growth control and disease. *Cell*, 149(2):274–293, 2012.

[6] D.D. Sarbassov, D.A. Guertin, S.M. Ali, and D.M. Sabatini. Phosphorylation and regulation of Akt/PKB by the rictor-mTOR complex. *Science*, 307(5712):1098–1101, 2005.

[7] J. Sötckli, D.J. Fazakerley, and D.E. James. GLUT4 exocytosis. *J Cell Sci*, 124(Pt 24):4147–4159, 2011.

[8] A. Klip, Y. Sun, T.T. Chiu, and K.P. Foley. Signal transduction meets vesicle traffic: the software and hardware of GLUT4 translocation. *Am J Physiol Cell Physiol*, 306(10):C879–C886, 2014.

[9] A. Efeyan and D.M. Sabatini. mTOR and cancer: many loops in one pathway. *Curr Opin Cell Biol*, 22(2):169–76, 2010.

[10] N. Cybulski and M.N. Hall. TOR complex 2: a signaling pathway of its own. *Trends Biochem Sci*, 34(12):620–627, 2009.

[11] J. Huang, C.C. Dibble, M. Matsuzaki, and B.D. Manning. The TSC1-TSC2 complex is required for proper activation of mTOR complex 2. *Mol Cell Biol*, 28(12):4104–4115, 2008.

[12] P. Dalle Pezze, A. G. Sonntag, A. Thien, M. T. Prentzell, M. Gödel, S. Fischer, et al. A dynamic network model of mTOR signaling reveals TSC-independent mTORC2 regulation. *Science Signaling*, 5(217):ra25–ra25, 2012.

[13] S. Salinari, C. Debard, A. Bertuzzi, C. Durand, P. Zimmet, H. Vidal, and G. Mingrone. Jejunal proteins secreted by db/db mice or insulin-resistant humans impair the insulin signaling and determine insulin resistance. *PLoS One*, 8(2):e56258, 2013.

[14] G. Mingrone, S. Panunzi, A. De Gaetano, C. Guidone, A. Iaconelli, et al. Bariatric surgery vs. conventional medical therapy for type 2 diabetes. *New Engl J Med*, 336:1577–1585, 2012.

[15] S.G. Dann, A. Selvaraj, and G. Thomas. mTOR Complex1-S6K1 signaling: at the crossroads of obesity, diabetes and cancer. *Physiology (Bethesda)*, 13(6):252–9, 2007.

[16] S. Wanant and M.J. Quon. Insulin receptor binding kinetics: modeling and simulation studies. *J Theor Biol*, 205(3):355–64, 2000.

[17] A.R. Sedaghat, A. Sherman, and M.J. Quon. A mathematical model of metabolic insulin signaling pathways. *Am J Physiol Endocrinol Metab*, 283(5):1084–101, 2002.

[18] E. Nyman, C. Brännmark, R. Palmér, J. Brugard, F.H. Nyström, P. Stralfors, and G. Cedersund. A hierarchical whole-body modeling approach elucidates the link between in Vitro insulin signaling and in Vivo glucose homeostasis. *J Biol Chem*, 286(29):26028–41, 2011.

[19] C. Brännmark, E. Nyman, S. Fagerholm, L. Bergenholm, E.M. Ekstrand, et al. Insulin signaling in type 2 diabetes: experimental and modeling analyses reveal mechanisms of insulin resistance in human adipocytes. *J Biol Chem*, 288(14):9867–9880, 2013.

[20] L. Giri, V.K. Mutalik, and K.V. Venkatesh. A steady state analysis indicates that negative feedback regulation of PTP1B by Akt elicits

bistability in insulin-stimulated GLUT4 translocation. *Theor Biol Med Model*, 1:2, 2004.

[21] G. Wang. Singularity analysis of the AKT signaling pathway reveals connections between cancer and metabolic diseases. *Phys Biol*, 7(4):046015, 2010.

[22] B. Cheatham and C. R. Kahn. Insulin action and the insulin signaling network. *Endocrine Reviews*, 16(2):117–142, 1995.

[23] G. Wilcox. Insulin and insulin resistance. *Clinical Biochemist Reviews*, 26(2):19, 2005.

[24] A. Golay and J. Ybarra. Link between obesity and type 2 diabetes. *Best Practice & Research Clinical Endocrinology & Metabolism*, 19(4):649–663, 2005.

[25] F. J. Bruggeman, J. J. Hornberg, F. C. Boogerd, and H. V. Westerhoff. Introduction to systems biology. In *Plant Systems Biology*, pages 1–19. 2007.

[26] D. E. Moller and J. S. Flier. Insulin resistance: mechanisms, syndromes, and implications. *N Engl J Med*, 325:938–948, 1991.

[27] R. A. DeFronzo, R. C. Bonadonna, and E. Ferrannini. Pathogenesis of niddm: a balanced overview. *Diabetes Care*, 15:318–368, 1992.

[28] R.N. Bergman, Y.Z. Ider, C.R. Bowden, and C. Cobelli. Quantitative estimation of insulin sensitivity. *Am J Physiol*, 236(1979):E667, 1979.

[29] A. De Gaetano and O. Arino. Mathematical modelling of the intravenous glucose tolerance test. *J Math Biol*, 40:136, 2000.

[30] S. Panunzi, A. De Gaetano, and G. Mingrone. Advantages of the single delay model for the assessment of insulin sensitivity from the intra-venous glucose tolerance test. *Theor Biol Med Model*, 7(9), 2010.

[31] E. Ferrannini, O. Bjorkman, G. A. Reichard, A. Pilo, M. Olsson, et al. The disposal of an oral glucose load in healthy subjects: a quantitative study. *Diabetes*, 34:580, 1985.

[32] E. Ferrannini, D. C. Simonson, L. D. Katz, G. Reichard, S. Bevilacqua, et al. The disposal of an oral glucose load in patients with non-insulin-dependent diabetes. *Metabolism*, 37:79, 1988.

[33] C. Dalla Man, K. E. Yarasheski, A. Caumo, H. Robertson, G. Toffolo, et al. Insulin sensitivity by oral glucose minimal models: validation against clamp. *Am J Physiol Endocrinol Metab*, 3289:E954, 2005.

[34] A. Caumo, R.N. Bergman, and C. Cobelli. Insulin sensitivity from meal tolerance tests in normal subjects: a minimal model index. *J Clin Endocrinol Metab*, 85:4396, 2000.

[35] E. Breda, M.K. Cavaghan, G. Toffolo, K.S. Polonsky, and C. Cobelli. Oral glucose tolerance test minimal model indexes of β-cell function and insulin sensitivity. *Diabetes*, 50:150, 2001.

[36] S. Salinari, A. Bertuzzi, and G. Mingrone. Intestinal transit of a glucose bolus and incretin kinetics: a mathematical model with application to the oral glucose tolerance test. *Am J Physiol Endocrinol Metab*, 300:E955–E956, 2011.

[37] R. A. DeFronzo, J. D. Tobin, and R. Andres. Glucose clamp technique: a method for quantifying insulin secretion and resistance. *American Journal of Physiology-Gastrointestinal and Liver Physiology*, 237(3):G214–G223, 1979.

[38] U. Picchini, A. De Gaetano, S. Panunzi, S. Ditlevsen, and G. Mingrone. A mathematical model of the euglycemic hyperinsulinemic clamp. *Theor Biol Med Model*, 2:44, 2005.

[39] G. I. Bell, T. Kayano, J. B. Buse, C. F. Burant, J. Takeda, H. Lin, D. Fukumoto, and S. Seino. Molecular biology of mammalian glucose transporters. *Diabetes Care*, 13:198–208, 1990.

[40] E. W. Kraegen, J. A. Sowden, M. B. Halstead, P. W. Clark, K. J. Rodnick, D. J. Chisholm, and D. E. James. Glucose transporters and in vivo glucose uptake in skeletal and cardiac muscle: fasting, insulin stimulation and immunoisolation studies of GLUT1 and GLUT4. *Biochem. j*, 295:287–293, 1993.

[41] J. E. Pessin and A. R. Saltiel. Signaling pathways in insulin action: molecular targets of insulin resistance. *Journal of Clinical Investigation*, 106(2):165, 2000.

[42] B. J. Goldstein, F. Ahmad, W. Ding, P. M. Li, and W. R. Zhang. Regulation of the insulin signalling pathway by cellular protein-tyrosine phosphatases. In *Insulin Action*, pages 91–99. 1998.

[43] M. G. Myers Jr, X. J. Sun, B. Cheatham, B. R. Jachna, E. M. Glasheen, J. M. Backer, and M. F. White. IRS-1 is a common element in insulin and insulin-like growth factor-I signaling to the phosphatidylinositol 3'-kinase. *Endocrinology*, 132(4):1421–1430, 1993.

[44] L. C. Cantley. The phosphoinositide 3-kinase pathway. *Science*, 296(5573):1655–1657, 2002.

[45] J. Luo, S. J. Field, J. Y. Lee, J. A. Engelman, and L. C. Cantley. The p85 regulatory subunit of phosphoinositide 3-kinase down-regulates IRS-1 signaling via the formation of a sequestration complex. *The Journal of cell biology*, 170(3):455–464, 2005.

[46] F. Koumanov, J.D. Richardson, B.A. Murrow, and G.D. Holman. AS160 phosphotyrosine-binding domain constructs inhibit insulin-stimulated GLUT4 vesicle fusion with the plasma membrane. *J Biol Chem*, 286(19):16574–16582, 2011.

[47] L.V. Ravichandran, H. Chen, Y. Li, and M.J. Quon. Phosphorylation of PTP1B at Ser(50) by Akt impairs its ability to dephosphorylate the insulin receptor. *Mol Endocrinol*, 15(10):1768–1780, 2001.

[48] D. Leto and A. R. Saltiel. Regulation of glucose transport by insulin: traffic control of glut4. *Nature reviews Molecular cell biology*, 13(6):383–396, 2012.

[49] C. Metcalfe and M. Bienz. Inhibition of GSK3 by Wnt signalling-two contrasting models. *J Cell Sci*, 124(Pt 21):3537–3544, 2011.

[50] D. A. Guertin and D. M. Sabatini. An expanding role for mTOR in cancer. *Trends in molecular medicine*, 11(8):353–361, 2005.

[51] C.A. Sparks and D.A. Guertin. Targeting mTOR: prospects for mTOR complex 2 inhibitors in cancer therapy. *Oncogene*, 29(26):3733–3744, 2010.

[52] R. Zoncu, A. Efeyan, and D.M. Sabatini. mTOR: from growth signal integration to cancer, diabetes and ageing. *Nat Rev Mol Cell Biol*, 12(1):21–35, 2011.

[53] S. Shin, L. Wolgamott, Y. Yu, J. Blenis, and S.O. Yoon. Glycogen synthase kinase (GSK)-3 promotes p70 ribosomal protein S6 kinase (p70S6K) activity and cell proliferation. *Proc Natl Acad Sci USA*, 108(47):E1204–E1213, 2011.

[54] B. Magnuson, B. Ekim, and D.C. Fingar. Regulation and function of ribosomal protein S6 kinase (S6K) within mTOR signalling networks. *Biochem J*, 441(1):1–21, 2012.

[55] S.H. Um, F. Frigerio, M. Watanabe, F. Picard, M. Joaquin, M. Sticker, S. Fumagalli, P.R. Allegrini, S.C. Kozma, J. Auwerx, and G. Thomas. Absence of S6K1 protects against age-and diet-induced obesity while enhancing insulin sensitivity. *Nature*, 431(7005):200–5, 2004.

[56] M. Fraenkel, M. Ketzinel-Gilad, Y. Ariav, O. Pappo, M. Karaca, J. Castel, M.F. Berthault, C. Magnan, E. Cerasi, N. Kaiser, and G. Leibowitz. mTOR inhibition by rapamycin prevents beta-cell adaptation to hyperglycemia and exacerbates the metabolic state in type 2 diabetes. *Diabetes*, 57(4):945–957, 2008.

[57] L. Wang, T. E. Harris, R. A. Roth, and J. C. Lawrence. PRAS40 regulates mTORC1 kinase activity by functioning as a direct inhibitor of substrate binding. *Journal of Biological Chemistry*, 282(27):20036–20044, 2007.

[58] Y. Sancak, C. C. Thoreen, T. R. Peterson, R. A Lindquist, S. A Kang, E. Spooner, S. A. Carr, and D. M. Sabatini. PRAS40 is an insulin-regulated inhibitor of the mTORC1 protein kinase. *Molecular cell*, 25(6):903–915, 2007.

[59] E. Vander Haar, S. Lee, S. Bandhakavi, T. J Griffin, and D. Kim. Insulin signalling to mtor mediated by the Akt/PKB substrate PRAS40. *Nature cell biology*, 9(3):316–323, 2007.

[60] M. Laplante and D. M. Sabatini. An emerging role of mTOR in lipid biosynthesis. *Current Biology*, 19(22):R1046–R1052, 2009.

[61] R. Loewith, E. Jacinto, S. Wullschleger, A. Lorberg, J. L. Crespo, D. Bonenfant, W. Oppliger, P. Jenoe, and M. N. Hall. Two TOR complexes, only one of which is rapamycin sensitive, have distinct roles in cell growth control. *Molecular cell*, 10(3):457–468, 2002.

[62] E. Jacinto, R. Loewith, A. Schmidt, S. Lin, M. A. Rüegg, A. Hall, and M. N. Hall. Mammalian TOR complex 2 controls the actin cytoskeleton and is rapamycin insensitive. *Nature cell biology*, 6(11):1122–1128, 2004.

[63] D. D. Sarbassov, S. M. Ali, S. Sengupta, J. Sheen, P. P. Hsu, A. F. Bagley, A. L. Markhard, and D. M. Sabatini. Prolonged rapamycin treatment inhibits mTORC2 assembly and Akt/PKB. *Molecular cell*, 22(2):159–168, 2006.

[64] D. A. Guertin, D. M. Stevens, M. Saitoh, S. Kinkel, K. Crosby, J. Sheen, D. J. Mullholland, M. A. Magnuson, H. Wu, and D. M. Sabatini. mTOR complex 2 is required for the development of prostate cancer induced by Pten loss in mice. *Cancer cell*, 15(2):148–159, 2009.

[65] C. M. Chresta, B. R. Davies, I. Hickson, T. Harding, S. Cosulich, et al. AZD8055 is a potent, selective, and orally bioavailable atp-competitive mammalian target of rapamycin kinase inhibitor with in vitro and in vivo antitumor activity. *Cancer Res*, 70(1):288–298, 2010.

[66] U.S. Bhalla and R. Iyengar. Emergent properties of networks of biological signaling pathways. *Science*, 283:381–387, 1999.

[67] J.M. Haugh and D.A. Lauffenburger. Physical modulation of intracellular signaling processes by locational regulation. *Biophys J*, 72:2014–2031, 1997.

[68] J. Lippincott-Schwartz, E. Snapp, and A. Kenworthy. Studying protein dynamics in living cells. *Nat Rev Mol Cell Biol*, 2:444–456, 2001.

[69] H. Kitano. Computational systems biology. *Nature*, 420(6912):206–210, 2002.

[70] S. Shankar. Reconstruction of cellular signalling networks and analysis of their properties. *Nat Rev Mol Cell Biol*, 6:99–111, 2005.

[71] W.W. Chen, M. Niepel, and P.K. Sorger. Classic and contemporary approaches to modeling biochemical reactions. *Genes & development*, 24(17):1861–1875, 2010.

[72] J. Hasty, F. Isaacs, M. Dolnik, D. McMillen, J. J. Collins, et al. Designer gene networks: towards fundamental cellular control. *Chaos*, 11:207–220, 2001.

[73] N. J. Eungdamrong and R. Iyengar. Computational approaches for modeling regulatory cellular networks. *Trends Cell Biol.*, 14(12):661–669., 2004.

[74] L. Michaelis and M.L. Menten. Die Kinetik der Invertinwirkung. *Biochem Z*, 49:333–369, 1913.

[75] A. Lehninger, D.L. Nelson, and M.M. Cox. Lehninger's principles of biochemistry. *W. H Freeman*, 2005.

[76] G. E. Briggs and J. B. S. Haldane. A note on the kinetics of enzyme action. *Biochemical journal*, 19(2):338, 1925.

[77] H. Bisswanger. *Enzyme Kinetics. Principles and Methods.* Wiley-VCH, Weinheim.

[78] L.A. Segel. On the validity of the steady state assumption of enzyme kinetics. *Bull Math Biol*, 6:579–593, 1988.

[79] L.A. Segel and M. Slemrod. The quasi-steady state assumption: a case study in perturbation. *SLAM Rev*, 31:446–477, 1989.

[80] A.R. Tzafriri. Michaelis-Menten kinetics at high enzyme concentrations. *Bull Math Biol*, 65:1111–1129, 2003.

[81] J. Borghans, R. de Boer, and L. Segel. Extending the quasi-stady state approximation by changing variables. *Bull Math Biol*, 58:43–63, 1996.

[82] A.R. Tzafriri and E.R. Edelman. The total quasi-steady-state approximation is valid for reversible enzyme kinetics. *J Theor Biol*, 226:303–313, 2004.

[83] M.G. Pedersen, A.M. Bersani, and E. Bersani. Quasi steady-state approximation in complex intraceccular signal transduction networks - a word of caution. *Journal of Mathematical Chemistry*, 43(4):1318–1344, 2007.

[84] M.G. Pedersen, A.M. Bersani, E. Bersani, and G. Cortese. The total quasi-steady-state approximation for complex enzyme reactions. *Mathematics and Computers in Simulation*, 79:1010–1019, 2008.

[85] A. Goldbeter and D.E. Jr Koshland. An amplified sensitivity arising from covalent modification in biological systems. *Proc Natl Acad Sci USA*, 78(11):6840–4, 1981.

[86] M.I. Stefan and N. Le Novére. Cooperative binding. *PLoS Comput Biol*, 9(6):e1003106, 2013.

[87] A. V. Hill. The possible effects of the aggregation of the molecules of haemoglobin on its dissociation curves. *J Physiol*, 40:iv–vii, 1910.

[88] K. Hirschberg, C. M Miller, J. Ellenberg, J. F. Presley, E. D. Siggia, R. D. Phair, and J. Lippincott-Schwartz. Kinetic analysis of secretory protein traffic and characterization of Golgi to plasma membrane transport intermediates in living cells. *The Journal of cell biology*, 143(6):1485–1503, 1998.

[89] A.E. Smith, B.M. Slepchenko, J.C. Schaff, L.M. Loew, and I.G. Macara. Systems analysis of Ran transport. *Science*, 295:488–491, 2002.

[90] N.A.W. van Riel. Dynamic modelling and analysis of biochemical networks: mechanism-based models and model-based experiments. *Briefings in Bioinformatics*, 7(4):364–374, 2006.

[91] C. Bruni and C. Ferrone. *Metodi di stima per il filtraggio e l'identificazione dei sistemi.* Aracne, 2008.

[92] K. Puszyński, P. Lachor, M. Kardyńska, and J. Śmieja. Sensitivity analysis of deterministic signaling pathways models. *Bulletin of the Polish Academy of Sciences: Technical Sciences*, 60(3):471–479, 2012.

[93] H. Yue, M. Brown, J. Knowles, H. Wang, D. S. Broomhead, and D. B. Kell. Insights into the behaviour of systems biology models from dynamic sensitivity and identifiability analysis: a case study of an nf-κb signalling pathway. *Mol BioSyst*, 2(12):640–649, 2006.

[94] K. A. Kim, S. L. Spencer, J. G. Albeck, J. M. Burke, P. K. Sorger, S. Gaudet, et al. Systematic calibration of a cell signaling network model. *BMC bioinformatics*, 11(1):202, 2010.

[95] I. M Sobol. Global sensitivity indices for nonlinear mathematical models and their Monte Carlo estimates. *Mathematics and computers in simulation*, 55(1):271–280, 2001.

[96] A. Saltelli. *Global Sensitivity Analysis: the primer.* John Wiley & Sons, London, 2008.

[97] T. Sumner, E. Shephard, and I. D. L. Bogle1. A methodology for global-sensitivity analysis of time-dependent outputs in systems biology modelling. *J. R. Soc. Interface*, 9:2156–2166, 2012.

[98] M. J. Quon and L. A. Campfield. A mathematical model and computer simulation study of insulin receptor regulation. *J Theor Biol*, 150(1):59–72, 1991.

[99] E. Nyman, G. Cedersund, and P. Stralfors. Insulin signaling - mathematical modeling comes of age. *Trends in Endocrinology and Metabolism*, 23(3):107–115, 2012.

[100] V.V. Kiselyov, S. Versteyhe, L. Gauguin, and P. De Meyts. Harmonic oscillator model of the insulin and IGF1 receptors' allosteric binding and activation. *Mol Syst Biol*, 5:243, 2009.

[101] C. Brännmark, R. Palmér, S.T. Glad, G. Cedersund, and P. Stralfors. Mass and information feedbacks through receptor endocytosis govern insulin signaling as revealed using a parameter-free modeling framework. *J Biol Chem*, 285(26):20171–9, 2010.

[102] P.K.U. Vinod and K. V. Venkatesh. Quantification of the effect of amino acids on an integrated mtor and insulin signaling pathway. *Mol BioSyst*, 5(10):1163–1173, 2009.

[103] G. Cedersund and P. Stralfors. Putting the pieces together in diabetes research: towards a hierarchical model of whole-body glucose homeostasis. *Eur J of Pharmac Sci*, 36(1):91–104, 2009.

[104] M. Koschorreck, H. Conzelmann, S. Ebert, M. Ederer, and E. D. Gilles. Reduced modeling of signal transduction–a modular approach. *BMC bioinformatics*, 8(1):336, 2007.

[105] Y. H. Chew, Y. L. Shia, C. T. Lee, F. A. A. Majid, L. S. Chua, et al. Modeling of glucose regulation and insulin-signaling pathways. *Mol Cell Endocrinol*, 303(1):13–24, 2009.

[106] C. Dalla Man, R. Rizza, C. Cobelli, et al. Meal simulation model of the glucose-insulin system. *IEEE Trans Biomed Eng*, 54:1740–1749, 2007.

[107] K. Oda, Y. Matsuoka, A. Funahashi, and H. Kitano. A comprehensive pathway map of epidermal growth factor receptor signaling. *Mol Syst Biol*, 1(1), 2005.

[108] L.A. Julien, A. Carriere, J. Moreau, and P.P. Roux. mTORC1-activated S6K1 phosphorylates Rictor on threonine 1135 and regulates mTORC2 signaling. *Mol Cell Biol*, 30(4):908–21, 2010.

[109] C. Guidone, M. Manco, E. Valera Mora, A. Iaconelli, D. Gniuli, et al. Mechanisms of recovery from type 2 diabetes after malabsorptive bariatric surgery. *Diabetes*, 55:2025–2031, 2006.

[110] A. Mari, M. Manco, C. Guidone, G. Nanni, M. Castagneto, G. Mingrone, and E. Ferrannini. Restoration of normal glucose tolerance in severely obese patients after bilio-pancreatic diversion: role of insulin sensitivity and beta cell function. *Diabetologia*, 49(9):2136–2143, 2006.

[111] C.Y. Huang and J.E. Jr Ferrell. Ultrasensitivity in the mitogen-activated protein kinase cascade. *Proc Natl Acad Sci USA*, 93(19):10078–83, 1996.

[112] G.C. Castellani, A. Bazzani, and L.N. Cooper. Toward a microscopic model of bidirectional synaptic plasticity. *Proc Natl Acad Sci USA*, 106(33):14091–5, 2009.

[113] T. Sasaoka, K. Fukui, T. Wada, S. Murakami, J. Kawahara, et al. Inhibition of endogenous ship2 ameliorates insulin resistance caused by chronic insulin treatment in 3T3-L1 adipocytes. *Diabetologia*, 48(2):336–344, 2005.

[114] S. Prakash, T. Inobe, A.J. Hatch, and A. Matouschek. Substrate selection by the proteasome during degradation of protein complexes. *Nat Chem Biol*, 5(1):29–36, 2009.

[115] X. Gao, P.R. Lowry, X. Zhou, C. Depry, Z. Wei, G.W. Wong, and J. Zhang. PI3K/Akt signaling requires spatial compartmentalization in plasma membrane microdomains. *Proc Natl Acad Sci USA*, 108(35):14509–14, 2011.

[116] D. Cozzone, S. Fröjdö, E. Disse, C. Debard, M. Laville, L. Pirola, and H. Vidal. Isoform-specific defects of insulin stimulation of Akt/protein kinase B (PKB) in skeletal muscle cells from type 2 diabetic patients. *Diabetologia*, 51(3):512–21, 2008.

[117] S.C. Yip, S. Saha, and Chernoff J. PTP1B: a double agent in metabolism and oncogenesis. *Trends Biochem Sci*, 35(8):442–9, 2010.

[118] L.S. Harrington, G.M. Findlay, A. Gray, T. Tolkacheva, S. Wigfield, H. Rebholz, J. Barnett, N.R. Leslie, S. Cheng, P.R. Shepherd, C.P. Gout, I. amd Downes, and R.F. Lamb. The TSC1-2 tumor suppressor controls insulin-PI3K signaling via regulation of IRS proteins. *J Cell Biol*, 166(2):213–23, 2004.

[119] I. Vivanco and C.L. Sawyers. The phosphatidylinositol 3-Kinase AKT pathway in human cancer. *Nat Rev Cancer*, 2(7):489–501, 2002.

[120] A. Shisheva. Phosphoinositides in insulin action on GLUT4 dynamics: not just PtdIns(3,4,5)P3. *Am J Physiol Endocrinol Metab*, 295(3):E536–44, 2008.

[121] H.K. Karlsson, J.R. Zierath, S. Kane, A. Krook, G.E. Lienhard, and H. Wallberg-Henriksson. Insulin-stimulated phosphorylation of the Akt substrate AS160 is impaired in skeletal muscle of type 2 diabetic subjects. *Diabetes*, 54(6):1692–1697, 2005.

[122] A. Kumar, T. E. Harris, S. R. Keller, K. M. Choi, et al. Muscle-specific deletion of rictor impairs insulin-stimulated glucose transport and enhances basal glycogen synthase activity. *Mol Cell Biol*, 28(1):61–70, 2008.

[123] T. Ijuin and T. Takenawa. Regulation of insulin signaling and glucose transporter 4 (GLUT4) exocytosis by phosphatidylinositol 3,4,5-trisphosphate (PIP3) phosphatase, skeletal muscle, and kidney enriched inositol polyphosphate phosphatase (SKIP). *J Biol Chem*, 87(10):6991–6999, 2012.

[124] T. Miyata, T. Taguchi, M. Uehara, S. Isami, H. Kishikawa, et al. Bradykinin potentiates insulin-stimulated glucose uptake and enhances insulin signal through the bradykinin b2 receptor in dog skeletal muscle and rat l6 myoblasts. *Eur J Endocrinol*, 138(3):344–352, 1998.

[125] M.E. Feldman, B. Apsel, A. Uotila, R. Loewith, and Z.A. Knight. Active-site inhibitors of mtor target rapamycin-resistant outputs of mTORC1 and mTORC2. *PLoS Biol*, 7(2):e38, 2009.

[126] T. Ijuin and T. Takenawa. Skip negatively regulates insulin-induced glut4 translocation and membrane ruffle formation. *Molecular and Cellular Biology*, 23(4):1209–1220, 2003.

[127] T. Sasaoka, H. Hori, T. Wada, M. Ishiki, T. Haruta, H. Ishihara, and M. Kobayashi. SH2-containing inositol phosphatase 2 negatively regulates insulin-induced glycogen synthesis in L6 myotubes. *Diabetologia*, 44(10):1258–1267, 2001.

[128] N. Nakashima, P. M. Sharma, T. Imamura, R. Bookstein, and J. M. Olefsky. The tumor suppressor PTEN negatively regulates insulin signaling in 3t3-l1 adipocytes. *J of Biol Chem*, 275(17):12889–12895, 2000.

[129] S. J. Kim, M. A. DeStefano, W. J. Oh, C. C. Wu, N. M. Vega-Cotto, et al. mTOR complex 2 regulates proper turnover of insulin receptor substrate-1 via the ubiquitin ligase subunit Fbw8. *Mol Cell*, 48(6):875–887, 2012.

[130] Y. Gu, J. Lindner, A. Kumar, W. Yuan, and M.A. Magnuson. Rictor/mTORC2 is essential for maintaining a balance between beta-cell proliferation and cell size. *Diabetes*, 60(3):827–837, 2011.

[131] N. Hashimoto, Y. Kido, T. Uchida, S. Asahara, Y. Shigeyama, et al. Ablation of PDK1 in pancreatic β cells induces diabetes as a result of loss of β cell mass. *Nat Genet*, 38(5):589–593, 2006.

[132] S.B. Kondapaka, M. Zarnowski, D.R. Yver, E.A. Sausville, and S.W. Cushman. 7 hydroxystaurosporine (UCN-01) inhibition of Akt Thr308 but not Ser473 phosphorylation: a basis for decreased insulin-stimulated glucose transport. *Clin Cancer Res*, 10(21):7192–7198, 2004.

[133] S. Sato, N. Fujita, and T. Tsuruo. Interference with PDK1-Akt survival signaling pathway by UCN-01 (7-hydroxystaurosporin). *Oncogene*, 21:1727–38, 2002.

[134] G. A. Soliman, H. A. Acosta-Jaquez, E. A. Dunlop, B. Ekim, N. E. Maj, et al. mTOR Ser-2481 autophosphorylation monitors mTORC-specific catalytic activity and clarifies rapamycin mechanism of action. *J Biol Chem*, 285(11):7866–7879, 2010.

[135] Y. Zhao, J. Yang, W. Liao, X. Liu, H. Zhang, S. Wang, D. Wang, J. Feng, L. Yu, and W. G. Zhu. Cytosolic Foxo1 is essential for the induction of autophagy and tumour suppressor activity. *Nat Cell Biol*, 12(7):665–675, 2010.

[136] L. Willems, N. Chapuis, A. Puissant, T. T. Maciel, A. S. Green, et al. The dual mTORC1 and mTORC2 inhibitor AZD8055 has anti-tumor activity in acute myeloid leukemia. *Leukemia*, 26(6):1195–1202, 2012.

[137] A. Bertuzzi, A. Gandolfi, C. Sinisgalli, and D. Iacoviello. Steel's potential doubling time and its estimation in cell populations affected by nonuniform cell loss. *Math Biosci*, 143(2):61–89, 1997.

[138] G. M. Cooper. The cell: A molecular approach, 2nd edn. Sunderland, MA., 2000.

[139] D. C. Allison, P. F. Ridolpho, S. Anderson, and K. Bose. Variations in the [^{3}H] thymidine labeling of S-phase cells in solid mouse tumors. *Cancer Res*, 45(12 Part 1):6010–6016, 1985.

[140] G. Mariño, M. Niso-Santano, E.H. Baehrecke, and G. Kroemer. Self-consumption: the interplay of autophagy and apoptosis. *Nat Rev Mol Cell Biol*, 15(2):81–94, 2014.

[141] S. Park, N. Chapuis, J. Tamburini, V. Bardet, P. Cornillet-Lefebvre, et al. Role of the PI3K/Akt and mTOR signalling pathways in acute myeloid leukemia. *Haematologica*, 95(5):819–828, 2010.

[142] Z. Zeng, D. D. Sarbassov, I. J. Samudio, K. W. Yee, M. F. Munsell, et al. Rapamycin derivatives reduce mTORC2 signaling and inhibit Akt activation in AML. *Blood*, 109(8):3509–3512, 2007.

[143] B. Novák and J.J. Tyson. A model for restriction point control of the mammalian cell cycle. *J Theor Biol*, 230(4):563–579, 2004.